University of California
Santa Barbara

Electronic Structure of Materials for Novel Computing and Energy Applications

A dissertation submitted in partial satisfaction
of the requirements for the degree

Doctor of Philosophy
in
Physics

by

Michael Warren Swift

Committee in charge:

Professor Chris G. Van de Walle, Co-Chair
Professor Leon Balents, Co-Chair
Professor S. James Allen

March 2018

The Dissertation of Michael Warren Swift is approved.

Professor S. James Allen

Professor Leon Balents, Co-Chair

Professor Chris G. Van de Walle, Co-Chair

March 2018

Electronic Structure of Materials for Novel Computing and Energy Applications

by

Michael Warren Swift

To Emmy Nœther, whose theorems make physics possible, and
to Emmy the cat, whose cuddles make physics bearable

Acknowledgements

First and foremost, I express my thanks to my PhD advisor, Chris Van de Walle. His mentorship—not only in research but also in writing and communications skills—has been invaluable, and this dissertation would not be possible without him. His management skills have kept my PhD on track, and his ability to attract and recruit great people has made the Van de Walle group an ideal place to learn to be a physicist.

Thanks to all the members of the Van de Walle group past and present I have had the pleasure of working with over the years: Hartwin Peelaers, Leigh Weston, Zhen Zhu, Youngho Kang, Darshana Wickramaratne, Xie Zhang, Anderson Janotti, Burak Himmetoglu, Cyrus Dreyer, Joel Varley, Lars Bjaalie, Karthik Krishnaswamy, Wennie Wang, Jimmy Shen, Nicholas Adamski, Andrew Rowberg, Mark Turiansky, and Azi Jackson. The staff scientists and postdocs have been invaluable resources and mentors to me, and it has been a pleasure working with, learning from, and getting to know the other students in the group. Thanks to my collaborators from outside the group: Matthew Fisher, Stephen Wilson, Tom Hogan, Zach Porter, and John Morton; their inspiration and ideas provided me valuable opportunities, and I have learned a great deal through our collaborations. Thanks to Susanne Stemmer and Evgeny Mikheev for stimulating the work on electron-electron scattering, and to Jozef Devreese for invaluable assistance in getting started and for providing the notes which make up the appendix. Thanks to my undergraduate advisors, Doug Natelson and Andriy Nevidomskyy, for helping me take my first steps as a researcher and giving me the tools I needed to start answering unanswered questions. Thanks to my committee, Leon Balents and Jim Allen, for valuable guidance and questions along the course of my PhD.

I would also like to express my thanks to my roommates: Evan Bauer, Lucas Brady, and Dan Ish. "Theorist house" has been an endless source of camaraderie and inside

jokes, physics and politics, whiskey sours and home-brewed beer, and I will truly miss each of them. Thanks to Emmy our cat, who adopted us and keeps us grounded by reminding us that feeding her is really our most important job.

Thanks to my friends at the San Clemente game night: Maher, Hannah, Abe, Carol, Jon, David, Sanjeev, and all the rest; we've had lots of fun together, and spending time with them has helped keep me sane and balanced in the hectic world of graduate school.

Thanks to my church, All Saints-by-the-Sea, and all the clergy, staff, and congregation, for providing a spiritual home these past years. It was a blessing to serve through and be served by them, and I will always carry a connection to All Saints in my heart.

Thanks to my parents, Jim and Deborah, for instilling in me from a young age a love of physics, math, problem-solving, and learning in general. Without them I would not be here or be who I am today. Thanks to my sisters Kathy and Charity for teaching me responsibility and for the joy of watching them grow up into their own exceptional individuals.

Last but certainly not least, my deepest personal thanks go to my wife, Terri Poxon-Pearson. Being married to her is the best part of my life, and I am continually sustained and encouraged by her constant love and support. Even though we have lived apart, she has filled my time in graduate school with adventure, fun, and love. I am truly grateful to have such a strong, intelligent, compassionate, and caring partner.

Curriculum Vitæ
Michael Warren Swift

Education

University of California Santa Barbara 09/2013 - Present
Advisor: Chris G. Van de Walle
Ph.D. in Physics expected 03/2018
Master of Arts in Physics 03/2016

Rice University 08/2009 - 05/2013
Bachelor of Science in Physics, *summa cum laude* and with Distinction in Research and Creative Work. Additionally met the requirements for a major in Mathematics, normally associated with a B.A. degree

Publications

1. M. W. Swift, C. G. Van de Walle, and M. P. A. Fisher: *Posner molecules: From atomic structure to nuclear spins* - Phys. Chem. Chem. Phys. (2018) doi:10.1039/C7CP07720C
2. M. W. Swift, Z. Porter, S. D. Wilson, and C. G. Van de Walle: *Electron doping in $Sr_3Ir_2O_7$: metal-insulator transition and collapse of magnetic order* - arXiv:1711.04173 [cond-mat.str-el] (2017)
3. M. W. Swift and C. G. Van de Walle: *Conditions for T^2 resistivity from electron-electron scattering* - Eur. Phys. J. B **90**, 151 (2017) doi:10.1140/epjb/e2017-80367-1
4. M. Swift and C. G. Van de Walle: *Impact of Point Defects on Proton Conduction in Strontium Cerate* - J. Phys. Chem. C **120**, 9562 (2016) doi:10.1021/acs.jpcc.6b00765
5. M. Swift, A. Janotti, and C. G. Van de Walle: *Small polarons and point defects in barium cerate* - Phys. Rev. B **92**, 214114 (2015) doi:10.1103/PhysRevB.92.214114
6. J. Lin, H. Ji, M. W. Swift, W. J. Hardy, Z. Peng, X. Fan, A. H. Nevidomskyy, J. M. Tour, and D. Natelson: *Hydrogen Diffusion and Stabilization in Single-Crystal VO_2 Micro/Nanobeams by Direct Atomic Hydrogenation* - Nano Lett. **14** (9), pp 544 -5451 (2014) doi:10.1021/nl5030694

7. Y. Filinchuk, N. Tumanov, V. Ban, H. Ji, J. Wei, M. W. Swift, A. Nevidomskyy, and D. Natelson: *In Situ Diffraction Study of Catalytic Hydrogenation of VO_2: Stable Phases and Origins of Metallicity* - J. Am. Chem. Soc. 136 (22), pp 810 -8109 (2014) doi:10.1021/ja503360y

Upcoming Manuscripts

1. J. Mansir, P. Conti, Z. Zeng, J.J. Pla, P. Bertet, M.W. Swift, C. G. Van de Walle, M.L.W. Thewalt, B. Sklenard, Y.M. Niquet, and J.J.L. Morton: *Linear hyperfine tuning of donor spins in silicon using hydrostatic strain* (under review)
2. M. W. Swift, J. L. L. Morton, and C. G. Van de Walle: *Hyperfine Interaction, Binding Energy, and Quadrupole Coupling of Shallow Donors in Silicon* (in preparation)
3. C. Peterson, M. W. Swift, Z. Porter, R. J. Clment, S. J. Moon, H. Cao, J. P. C. Ruff, C. G. Van de Walle, and S. D. Wilson: *$Sr_3Ir_2O_7F_2$: Topotactic transformation of a relativistic Mott insulator into a band insulator through F insertion* (in preparation)

Conference Participation

American Physical Society March Meeting 03/2018
Invited Talk: *Conditions for T^2 resistivity from electron-electron scattering*
Talk: *Electron doping in $Sr_3Ir_2O_7$: metal-insulator transition and collapse of magnetic order*

American Physical Society March Meeting 03/2017
Talk: *Conditions for T^2 resistivity from electron-electron scattering*
Session chair: Quantum Monte Carlo and General Computational Physics

Materials Research Outreach Program Symposium (MROP) 02/2017
Poster: *Transport in complex oxides: understanding mobility from first principles*

American Physical Society March Meeting 03/2016
Talk: *Point defects and band alignment in strontium cerate*

American Physical Society March Meeting 03/2015
Talk: *Small Polarons and Point Defects in Barium Cerate*

Materials Research Outreach Program Symposium (MROP) 02/2015
Poster: *Barium Cerate from First Principles: Band Structure, Point Defects, and Polarons*

Rice Quantum Institute Colloquium 08/2013
Poster: *Hydrogen Diffusion in Vanadium Dioxide*

Research Positions

Graduate Student Researcher 06/2014 - Present
Advisor: Prof. Chris G. Van de Walle, UCSB.
Studied electronic properties of materials using Density Functional Theory (DFT). Projects included proton conduction ($BaCeO_3$ and $SrCeO_3$), electron-electron scattering (especially in $SrTiO_3$), electron doping and fluorine incorporation in the spin-orbit Mott insulator $Sr_3Ir_2O_7$, and hyperfine properties of shallow donors in silicon. Developed expertise in condensed matter physics, first-principles computational methods, and programming (Python, Mathematica, Fortran, and C). Work resulted in 5 first-author publications, with 3 more publications in preparation.

Postbaccalaureate researcher 05/2013 - 08/2013
Advisor: Prof. Andriy Nevidomskyy, Rice University.
Performed DFT calculations on newly discovered phases of hydrogenated VO_2. Resulted in JACS publication (Filinchuk *et al.*)

Undergraduate Researcher 01/2011 - 08/2013
Advisors: Profs. Doug Natelson and Andriy Nevidomskyy, Rice University.
Performed DFT calculations on hydrogenated VO_2. Senior thesis: *Density Functional Theory Calculations for Hydrogenated Vanadium Dioxide*. Resulted in Nano Letters publication (Lin *et al.*). Explored new experimental techniques for measuring VO_2 nanowires.

REU student 05/2012 - 08/2012
Advisors: Profs. Michael Hildreth and Kevin Lannon, University of Notre Dame.
Analyzed a potential tracking algorithm for the SLHC upgrade. Published in *Scientia* 4, 40 (2013) (*Scientia* is the undergraduate research journal at the University of Notre Dame.)

Leadership Experience

Graduate Students for Diversity in Science 02/2015 - Present

- Member—Attended meetings, voted on body-wide decisions, participated in outreach events and hosted distinguished speakers
- Reverse Site Visit Chair, Outreach Committee—Organized and attended outreach visits to local Hispanic-serving institutions to spread awareness of graduate school as a career option, answer questions, and provide role models.

Chemical Sciences Student Seminar 02/2015 - Present

- Executive Committee—Organized seminar featuring talks from a wide variety of fields in the chemical sciences, vetted talks, awarded travel grants to outstanding speakers
- Fundraising Chair—Recruited sponsors to pay for seminars and travel grant awards

Gradlife committee 09/2015 - 08/2016
Organized official social events for graduate students in the physics department

Physics Circus 09/2013 - 03/2015
Presented physics demonstrations and experiments on the road to local schools.

Academic Fellow, Jones College, Rice University 08/2011 - 05/2013
Provided tutoring, advising, and other academic assistance to peers

President, Rice University Society for Physics Students 08/2012 - 05/2013
Organized meetings, lectures, and social events

Honors and Recognition

- Invited Talk, American Physical Society March Meeting 2018
- Honorable Mention, NSF Graduate Research Fellowhsip Program 2015
- Member of Sigma Pi Sigma: The Physics Honors Society
- Academic Fellow for Physics, Jones College, Rice University
- Sophomore Scholar and Junior Scholar, Jones College, Rice University
- Presidents Honor Roll, Rice University (x8): Fall 2009 - Spring 2013

Abstract

Electronic Structure of Materials for Novel Computing and Energy Applications

by

Michael Warren Swift

First-principles calculations based on density functional theory are an invaluable tool in the prediction and understanding of materials properties based on their atomic and electronic structure. Computational results provide relevant insight for applications in the energy sector and in novel computational platforms. We begin by addressing a longstanding problem: the computation of binding energies and hyperfine interactions for shallow dopants in semiconductors. We have developed new techniques for calculating these properties with remarkable accuracy, providing guidance for engineering of spin qubits. We move on to electronic complex oxides, studying electron-electron scattering in $SrTiO_3$. We develop a general methodology to calculate electron-electron scattering rates, and identify the conditions under which the mechanism gives rise to a well-known T^2 power law in resistivity. We then turn to the unconventional electronic phase found in the spin-orbit Mott insulator $Sr_3Ir_2O_7$. The electron-doping-driven metal-insulator transition is studied and structural distortions in the correlated metallic state are shown to arise from a different mechanism from the transition itself. Turning finally from electronic conduction to ionic conduction, we study hydrogen transport and optical properties in $BaCeO_3$. We establish a new understanding of electron localization in this material and explain the results of luminescence experiments. In $SrCeO_3$, cation vacancies are shown to be an important source of proton traps which impede diffusion, and known benefits of doping are explained as resulting from a suppression of these vacancies. In each material, advances in fundamental understanding guide experiment and advance applications.

Contents

Chapter 1

Introduction

The properties of the materials that make up our world are determined by their microscopic structure. In a crystalline solid, this structure takes the form of a periodic arrangement of ions bound together by electrons. The research presented here is based on Density Functional Theory (DFT), a technique which is able to calculate the ionic and electronic structure of materials from first principles (i.e., starting from the fundamental laws of quantum mechanics). We use this methodology, discussed in detail in Chapter 2, to explore fundamental physical properties of materials with exciting applications in the energy sector and/or in novel computational platforms. In each case, we seek to build understanding that is interesting from a theoretical perspective, informs experiment, and is relevant to real-world applications.

We begin by presenting work on shallow donors in silicon, a physical system that is at the heart of modern electronics, and also an exciting platform for possible spin-based quantum computation (Chapter 3). We provide new theoretical insight by overcoming various challenges to the first-principles modeling of shallow impurities; we use hybrid functionals to correctly capture localization and traditional functionals to extrapolate to the dilute limit. This advance allows us to achieve remarkable accuracy in the calculation

of binding energies and hyperfine parameters. We also investigate bismuth donors under strain, supporting recent experimental results showing that the hydrostatic component of strain has an unexpectedly large impact on the hyperfine parameter, and ruling out a proposed quadrupole-mediated mechanism for observed shifts under strain.

Moving beyond silicon, we focus on complex oxides, which are being explored as next-generation electronic materials, necessitating a fundamental understanding of carrier mobility and conductivity. Many complex oxides (including titanates, nickelates and cuprates) show a regime in which resistivity follows a power law in temperature ($\rho \propto T^2$). By analogy to a similar phenomenon observed in some metals at low temperature, this has often been attributed to electron-electron (Baber) scattering. In Chapter 4, we develop a new computational methodology to calculate electron-electron scattering rates from first principles. We show that Baber scattering should only be expected to give a T^2 power law under several crucial assumptions (which may not hold for complex oxides), and we use our methodology to calculate the electron-electron scattering rate directly. We demonstrate that for strontium titanate, $\rho_{\text{el-el}} \not\propto T^2$. This provides guidance for the interpretation of experiments; an observation of $\rho \propto T^2$ is not always sufficient evidence for electron-electron scattering. The understanding of electron-electron scattering and other scattering mechanisms is crucial for applications as well, since low carrier mobility is a significant obstacle for many proposed electronic devices based on complex oxides.

In addition to conventional electronic behavior like electron-electron scattering, complex oxides host a plethora of exotic electronic phases, including topological insulators and high-T_c superconductivity. These unconventional phases could be the key to world-changing applications such as topological quantum computing or superconducting electronics. One particularly exciting variety of unconventional electronic behavior is the spin-orbit Mott phase, in which a gap is opened by a combination of electron correlations and spin-orbit coupling. In Chapter 5, we apply our first-principles methodology

to the spin-orbit Mott insulator $Sr_3Ir_2O_7$. We explore the electron-doping-driven phase transition in which this material goes from an antiferromagnetic insulator to a paramagnetic metal. Both states are identified in our calculations, and the charge gap and staggered magnetization are observed to decrease with increasing doping. We identify a transition at a doping level that is in excellent agreement with experiment. This suggests that the magnetic and electronic transitions are intimately related. Curiously, our first-principles calculations fail to capture the low-temperature structural distortion reported in La-substituted $Sr_3Ir_2O_7$. This supports the notion that this distortion arises as a secondary manifestation of an unconventional electronic order parameter in this material, and rules out a commonly proposed mechanism for the distortions and the transition.

Complex oxides are important not only for electronic applications, but also for energy generation and storage, demanding investigations of ionic conduction in addition to electronic conduction. In particular, barium cerate ($BaCeO_3$) and strontium cerate ($SrCeO_3$) are well-known proton conductors, with proposed applications in solid state fuel cells, water splitting, batteries, and beyond. The cerates are frequently doped (for instance with Y) to increase stability and promote diffusion. However, the effects of doping and native defects are not fully understood. Computational studies have been stymied by the cerium $4f$ states which make up the conduction band and which cannot be correctly described by first-principles methods using traditional functionals. In Chapter 6, we use a hybrid functional to overcome this obstacle, and use this theoretical advance to investigate the effects of hydrogen impurities and native defects on the electrical and optical properties of $BaCeO_3$. Since the primary applications of this material involve proton conduction, we focus on interactions between defects that may reduce proton diffusivity. We discuss the tendency of excess electrons or holes to localize in the form of small polarons: localized charge carriers coupled to a lattice distortion. We explore their interactions with hydrogen impurities and their impact on optical properties of the material, opening

the way for experiments to further probe the polaronic properties of this material. In Chapter 7, we find the positions of the bands on an absolute energy scale, an essential piece of information for water-splitting applications. We also study the atomic and electronic structure of impurities and defects, finding that interactions between hydrogen and cation vacancies negatively impact proton conductivity. This explains the efficacy of acceptor doping in proton conducting applications, since it will tend to reduce the concentration of cation vacancies. Comparisons between $SrCeO_3$ and $BaCeO_3$ allow us to establish general trends that are relevant across a wide variety of proton-conducting complex oxides.

By the end of this dissertation, we hope to have shown that first-principles calculations have expanded our understanding of the fundamental microscopic properties, paving the way for exciting applications in the energy sector and in novel computational platforms.

1.1 Permissions and attributions

Chapter 2

First-Principles Computational Methods

2.1 The many body problem

The behavior of electrons in a solid is given by the many-body Schrödinger equation

$$\hat{H}\Psi(\mathbf{r}_1, \mathbf{r}_2, \ldots, \mathbf{r}_N) = E\Psi(\mathbf{r}_1, \mathbf{r}_2, \ldots, \mathbf{r}_N), \tag{2.1}$$

where $\hat{H}$ is the Hamiltonian that describes the electrons' interaction with each other and the nuclei in the solid. Within the Born-Oppenheimer approximation, the nuclei are treated as fixed point charges, so their degrees of freedom can be ignored while solving the electronic problem. The Hamiltonian becomes

$$\hat{H} = -\frac{\hbar^2}{2m}\sum_{i=1}^{N}\nabla_i^2 - \frac{e^2}{4\pi\epsilon_0}\sum_{i=1}^{N}\sum_{j=1}^{M}\frac{Z_j}{|\mathbf{r}_i - \mathbf{R}_j|} + \frac{e^2}{4\pi\epsilon_0}\sum_{i<k}\frac{1}{|\mathbf{r}_i - \mathbf{r}_k|}, \tag{2.2}$$

where i and k index electrons and j indexes nuclei. For all practical purposes, this Hamiltonian is impossible to solve exactly. Not only does the electron-electron interaction term combined with the required antisymmetry of the wavefunction under exchange of two electrons lead to an extremely complicated electronic wavefunction, but the $3N$ degrees of freedom necessary to describe the full wavefunction would make the result unfeasible to store, process, or interpret. A simplification is needed.

2.2 Density functional theory

In 1964, Pierre Hohenberg and Walter Kohn proved that, for Hamiltonians describing particles moving in an external potential (such as the many-body Hamiltonian in Eq. (2.2)), the potential, and hence the wavefunction and all the properties of the system, are all universal functionals of the electron density n [4]. A particularly relevant functional is the energy $E_0 = E_0[n(\mathbf{r})]$ of the ground state. Given the exact form of this functional, the many-body problem reduces from the $3N$-dimensional problem of finding the many-body wavefunction to a 3-dimensional problem of finding the electron density. Hohenberg and Kohn went on to propose the first approximations to this universal functional based on the Thomas-Fermi method.

In 1965, Walter Kohn and Lu Jeu Sham outlined a method to build an effective potential v_{eff} for non-interacting single-particle orbitals ϕ which, when populated with the correct number of Fermions, reproduce the ground-state electron density:

$$\left(-\frac{\hbar^2}{2m}\nabla^2 + v_{\text{eff}}(\mathbf{r})\right)\phi_i(\mathbf{r}) = \varepsilon_i\phi_i(\mathbf{r}), \tag{2.3}$$

$$n(\mathbf{r}) = \sum_i^N |\phi_i(\mathbf{r})|^2. \tag{2.4}$$

The energy is written as a functional of the density:

$$E[n] = T_s[n] + \int d\mathbf{r}\ v_{\text{ext}}(\mathbf{r})n(\mathbf{r}) + E_H[n] + E_{\text{xc}}[n], \tag{2.5}$$

where

$$T_s[n] = \sum_{i=1}^{N} \int d\mathbf{r}\ \phi_i^*(\mathbf{r}) \left(-\frac{\hbar^2}{2m}\nabla^2\right) \phi_i(\mathbf{r}), \tag{2.6}$$

$$E_H = \frac{e^2}{2} \int d\mathbf{r} \int d\mathbf{r}'\ \frac{n(\mathbf{r})n(\mathbf{r}')}{|\mathbf{r}-\mathbf{r}'|}, \tag{2.7}$$

$v_{\text{ext}}(\mathbf{r})$ is the external potential (provided by the nuclei), and $E_{\text{xc}}[n]$ is the so-called "exchange-correlation" functional, which includes all effects induced by wavefunction antisymmetry (exchange energy) and by many-body correlations. Most of the approximations involved with DFT are contained in E_{xc}, and improving this functional has been the focus of substantial effort.

2.3 Local density and generalized gradient approximations

One of the earliest approximations to E_{xc} is the so-called Local Density Approximation, or LDA. Proposed by Hohenberg and Kohn in their original paper, this approximation assumes that the exchange-correlation energy is local, with the contribution due to the electron density at each point equal to that of a homogeneous electron gas with that density. Since the homogeneous electron gas has been solved analytically, the LDA

exchange-correlation functional can be written down:

$$E_{\text{xc}}^{\text{LDA}}[n] = \int n(\mathbf{r})\epsilon_{xc}(n)\ \mathrm{d}\mathbf{r} = -\frac{3}{4}\left(\frac{3}{\pi}\right)^{1/3}\int n(\mathbf{r})^{4/3}\ \mathrm{d}\mathbf{r}\ . \tag{2.8}$$

This was further improved by the Generalized Gradient Approximation or GGA, which takes into account the gradient of the density in addition to its local value:

$$E_{\text{xc}}^{\text{GGA}}[n_\uparrow, n_\downarrow] = \int \epsilon_{XC}(n_\uparrow, n_\downarrow, \nabla n_\uparrow, \nabla n_\downarrow) n(\mathbf{r})\mathrm{d}^3\mathbf{r}\,. \tag{2.9}$$

A common GGA is that of John Perdew, Kieron Burke, and Matthias Ernzerhof, commonly known as PBE [5].

The LDA and GGA have enjoyed remarkable and wide-ranging success across many fields of physics and chemistry. This success is particularly remarkable given their relative simplicity compared to the immense complexity of the many-body problem. However, these approximations are far from perfect. One of their most egregious shortcomings is the so-called "self-interaction" error. This arises because the term describing the mean-field Coulomb repulsion (the "Hartree term", Eq. (2.7)) includes an unphysical interaction between an electron and its own density. Self-interaction error leads to an over-delocalization of the electronic states, and is related to the "band-gap problem" in which LDA and GGA underestimate the band gap of most semiconductors and insulators.

2.4 DFT+U

Localized states and correlation-driven physics (e.g. Mott insulating behavior) are often described through the Hubbard model:

$$\hat{H} = -t \sum_{\langle i,j \rangle, \sigma} (\hat{c}^{\dagger}_{i,\sigma} \hat{c}_{j,\sigma} + \hat{c}^{\dagger}_{j,\sigma} \hat{c}_{i,\sigma}) + U \sum_{i=1}^{N} \hat{n}_{i\uparrow} \hat{n}_{i\downarrow} \,. \tag{2.10}$$

The parameters of this model are the hopping strength t and the on-site Coulomb repulsion U. Inspired by the success of this model, DFT+U adds a term to penalize double-occupation of an orbital:

$$E^{\mathrm{LDA}+U}[n] = E^{\mathrm{LDA}}[n] + \sum_{I} \left[\frac{U^I}{2} \sum_{m,\sigma \neq m',\sigma'} n^{I\sigma}_{m} n^{I\sigma'}_{m'} - \frac{U^I}{2} n^I (n^I - 1) \right] , \tag{2.11}$$

where $n^{I\sigma}_{m}$ are the occupation numbers of localized orbitals identified by the atomic site index I, state index m and by the spin σ [6]. This term induces physics similar to that observed in the Hubbard model into DFT, and allows for the successful application of DFT+U to materials that are inaccessible to LDA and GGA, such as Mott insulators.

A weakness of the DFT+U method is the need to choose a value for the onsite Coulomb repulsion parameter U. In practice, U is often tuned to reproduce the experimental band gap, though this can be problematic for a number of reasons. Tuning to experiment loses some of the *ab initio* nature of the method, and thus some of the predictive power. In addition, there are multiple reasons why experimental signatures purporting to measure the band gap may not be expected to match a DFT band structure (temperature effects, renormalization due to many-body effects, and unintentional measurement of a sub-band-gap excitation, among others), so matching to an experimental gap may actually give incorrect physics. Another method is to use constrained DFT

or similar approaches to self-consistently calculate the value of U. This is additional computational effort, and may not reproduce experimental results as well as a U tuned to do so, but it retains the *ab initio* predictive power of DFT.

DFT+U is used in this dissertation for simulation of the spin-orbit Mott insulator $Sr_3Ir_2O_7$ (Chapter 5). The U value is taken from constrained RPA calculations in the literature.

2.5 Hybrid functionals

Unlike in the Kohn-Sham approach, wavefunctions in the Hartree-Fock method are Slater determinants, which enforce the Pauli antisymmetrization condition by construction. Hartree-Fock is thus said to have "exact exchange", since the exchange properties of the wavefunction are necessarily correct. While Hartree-Fock has significant limitations when applied to solids (especially metals) [7], inclusion of this "exact" exchange energy is attractive as a possible way to improve the DFT exchange-correlation functional. This is accomplished through a mixing of the Hartree-Fock with conventional DFT exchange-correlation functionals. In the PBE0 hybrid [8], the exchange-correlation energy is

$$E_{\mathrm{xc}} = E_{\mathrm{xc}}^{\mathrm{DFT}} + a_0(E_x - E_{\mathrm{x}}^{\mathrm{DFT}}), \tag{2.12}$$

where E_x is the Fock-like exact exchange for the Kohn-Shame states:

$$E_x = \langle\Psi|\,\hat{V}_{ee}\,|\Psi\rangle - \frac{e^2}{2}\int d^3\mathbf{r}\,d^3\mathbf{r}'\frac{n(\mathbf{r})n(\mathbf{r}')}{|\mathbf{r}-\mathbf{r}'|}. \tag{2.13}$$

A value of $a_0 = 1/4$ is argued to be best for typical molecules based on Görling-Levy perturbation theory. PBE0 was further improved in 2003 by Jochen Heyd, Gustavo Scuseria, and Matthias Ernzerhof in the HSE functional [9]. This is a "range-separated"

hybrid, in which screening is taken into account by separating $1/r$ into short-range (SR) and long-range (LR) parts:

$$\frac{1}{r} = \underbrace{\frac{\mathrm{erfc}(\omega r)}{r}}_{\mathrm{SR}} + \underbrace{\frac{\mathrm{erf}(\omega r)}{r}}_{\mathrm{LR}}, \tag{2.14}$$

where ω is the "screening length", a parameter describing the extent of range separation, typically set to $\omega = 0.207\,\text{Å}^{-1}$ [10]. The HSE hybrid functional has shown remarkable success, not only in chemistry, but also in fixing the band-gap problem in semiconductors (with occasional tweaks of the mixing parameter a_0) and in the correct description of localized states in many materials systems. Our calculations of donors in silicon (Chapter 3), $SrTiO_3$ (Chapter 4), $BaCeO_3$ (Chapter 6), and $SrCeO_3$ (Chapter 7) all make use of the HSE hybrid functional with the standard mixing and screening lengths.

2.6 Practical aspects

Our calculations are performed using the Vienna Ab initio Simulation Package (VASP) [11]. Core electrons are described using the Projector-Augmented Wave (PAW) method [12], an extension of the common pseudopotential method which allows reconstruction of wavefunctions including the core electrons through the use of projectors. Valence electrons are described by Kohn-Sham states, which are expanded in a plane wave basis. This allows for systematic improvement of the basis set through increasing of the plane-wave energy cutoff, which is increased until convergence is reached. The cutoffs used and various other technical details are reported in the individual chapters.

2.7 Defect formation energies

The energy cost of incorporating a defect X in charge state q in the solid is given by the formation energy [13]

$$E^f[X^q] = E_{\text{tot}}[X^q] - E_{\text{tot}}[\text{bulk}] - \sum_i n_i \mu_i + qE_F + \Delta^q \,, \tag{2.15}$$

where $E_{\text{tot}}[X^q]$ is the DFT total energy of a supercell containing the defect X in charge state q, $E_{\text{tot}}[\text{bulk}]$ is the total energy of a supercell of the same size but without the defect, and n_i is the number of atoms of type i added ($n_i > 0$) or removed ($n_i < 0$) to form the defect. μ_i are the corresponding chemical potentials of the species, referenced to the total energies per atom of their respective ground-state phases. The chemical potentials are treated as variables that can depend on growth or processing conditions. However, bounds are placed on these values by imposing the conditions for stability in thermodynamic equilibrium.

The chemical potential of electrons in the solid is the Fermi energy E_F; the qE_F term is the energy required to add or remove electrons to achieve charge state q. By convention, we take $E_F = 0$ at the valence-band maximum. The final term, Δ^q, is a correction term designed to compensate for interaction between a charged defect and its periodic images. This allows us to study defects in the dilute limit. Refs. [14] and [15] describe the method used to calculate Δ^q. Calculation of this term requires the static dielectric constant of the material, including both the electronic and ionic contributions.

2.8 Shallow donors in silicon

Chapter 3 deals with the calculation of shallow donors in silicon using density functional theory. In this section we lay out the theoretical background of the study of shallow donors and discuss some technical details of the calculations.

2.8.1 Kohn-Luttinger effective mass theory

The effective mass approximation was developed by Kohn and Luttinger in the 1950s [16, 17, 18] to describe shallow donors in silicon and other semiconductors. According to this theory, a shallow donor has a binding energy (relative to the CBM) of

$$E_D^b = \frac{m_e^*}{m_0}\frac{1}{\varepsilon_r^2}\frac{m_0 e^4}{2(4\pi\varepsilon_0\hbar)^2}\,, \tag{2.16}$$

where m_e^* is the effective mass of the band state, m_0 is the free electron mass, and ε_r is the dielectric constant of the crystal [19]. The wavefunction itself is given by a product of the host wavefunction at the CBM and a hydrogenic envelope function:

$$\Psi = \frac{1}{\sqrt{\pi a_D^3}} e^{-r/a_D} e^{i\mathbf{k}\cdot\mathbf{r}} u_{\mathbf{k}}(\mathbf{r})\,, \tag{2.17}$$

where $\mathbf{k}$ is the position of the CBM in k-space. The extent of the hydrogenic wavefunction is given by the "effective Bohr radius"

$$a_D = \frac{m_0}{m_e^*}\varepsilon_r a_B\,, \tag{2.18}$$

where $a_B = 0.053$ nm is the Bohr radius [19]. In the case of silicon, the transverse and longitudinal effective masses are quite different: $m_L^* = 0.916\, m_e$ and $m_T^* = 0.191\, m_e$. Including this anisotropy requires only a modest generalization of the theory, and the

ground state may be found variationally [20]. An isotropic effective mass of $m^* = 0.3\,m_e$ may be defined for use in Eq. (2.16), giving similar results [20]. In this way, one is able to derive the Kohn-Luttinger binding energy for donors in silicon: 31.2 meV [20]. This underestimates the ground-state binding energy of (e.g.) a bismuth donor, 70.88 meV [20].

Two complications quickly became apparent: multivalley effects and the central-cell correction [21]. Subsequent developments in the treatment of shallow impurities have focused on corrections for these two effects and attempts to include them in models. This effort has met with success through the use of empirical fitting parameters, but a full *ab initio* description has remained elusive. As recently as 2015, Saraiva *et al.* reported that they were "unaware of any successful description of the complete spectrum of the [shallow donor] $1s$ manifold from first principles." [20]

2.8.2 Multivalley effects

In bulk silicon, the conduction-band minimum is a set of six degenerate valleys [19]. As discussed above, Kohn and Luttinger approximated these valleys as non-interacting, effectively reducing the system to a one-valley problem with anisotropic effective masses and achieving only rough agreement with experiment [18]. The largest correction is valley-orbit coupling, which breaks the degeneracy of the valleys and significantly lowers the energy of the ground state [20, 21, 22]. This is allowed because the effective-mass-theory approximation of the impurity potential as a small perturbation of the host crystal breaks down close to the impurity site. Group-theoretic arguments show that the 6-fold degenerate CBM splits into states corresponding to irreducible representations of the T_d symmetry group: singlet A_1, doublet E, and triplet T_2 [20, 23]. Perturbative methods with no adjustable parameters have had some success in describing intervalley coupling for

phosphorus in silicon [24], but empirical impurity potentials fitted to experimental data remain the standard for treating multivalley effects in effective mass methods [25, 26, 27], tight-binding methods [28], and exact-diagonalization methods [23].

The different valley-orbit-coupled states have significantly different spatial distributions from one another, which in turn influences the hyperfine parameters [29]. Therefore a correct description of valley-orbit coupling is essential, not only for the description of binding energies, but for the calculation of hyperfine parameters.

2.8.3 Central-cell correction

The strong perturbation of the bulk potential near the impurity site is key to the correct description of multivalley effects, as discussed in Sec. 2.8.2. This perturbation has other effects as well. The impurity potential is screened by valence electrons in the host, and the host crystal itself will react to the presence of the impurity in complex material- and impurity-dependent ways. These effects are collectively known as "central-cell corrections", a term which is sometimes defined to include valley-orbit coupling. Empirical impurity potentials are the standard tool to account for central-cell corrections in effective mass theory [30, 31, 32] and tight-binding [33]. The greater spread of multivalley wavefunctions in k-space allows them to be more concentrated towards the impurity center in real space, making the central-cell correction more important for multivalley materials such as silicon [20]. Since the isotropic hyperfine parameter (i.e., the Fermi contact interaction) is based purely on the wavefunction at the impurity, central-cell corrections are especially important for the hyperfine interaction [32, 33].

2.8.4 Prior first-principles work

Density functional theory has been shown to correctly predict hyperfine parameters for localized defect states [34], but shallow donors are more challenging. This difficulty comes primarily from the spatial delocalization of the donor wavefunction (which is much more extended than the size of typical DFT simulation cells) and from the overdelocalization inherent in traditional functionals. Previous work in this area is discussed in Sec. 3.2. Various authors have used *ab initio* impurity studies with a Green's function approach to study shallow donor wavefunctions [35, 36].

Given a linear operator L, a Green's function is a function $G(x, s)$ such that

$$LG(x, s) = \delta(x - s)\,. \tag{2.19}$$

Once calculated, the bulk Green's function can be perturbed by the impurity potential, as calculated in a small supercell, and then extended to calculate the entire wavefunction of the shallow donor. The Green's function method is well-suited for the calculation of the hyperfine interaction of shallow donors because it does not rely on a supercell to describe the wavefunction in the central region. Only the change in potential due to the impurity is needed, since this information is sufficient to perturb the bulk Green's function. Non-negligible changes in the potential occur only quite close to the impurity center, so the need for large supercells is avoided. However, since the Green's function ignores the long-range tail of the Coulomb potential for that part of the induced density that is not contained within the perturbed region, the binding energy is not correctly captured [35]. The perturbation of the bulk Green's function by the impurity potential is also complicated and requires various approximations. In spite of these complications, hyperfine parameters have been successfully calculated by this method. In Ref. [35], Overhof and Gerstmann calculated hyperfine parameters of various common shallow

donors in silicon and found good agreement with experiment. In Ref. [36], Huebl *et al.* employed the Green's function method to include the effects of strain, again achieving good agreement with experiment.

Over the past decade, the defect Green's function method for treating impurities in general has largely fallen out of favor due to increasing computational power and improved algorithms to correct for supercell artifacts, and the fact that finding the bulk Green's function can be difficult. However, it remains attractive for calculating hyperfine parameters, due to its ability to correctly simulate properties of the center of a defect without needing to explicitly calculate a large supercell of the host material.

2.9 Electron-electron scattering

Electron-electron scattering is discussed in Chapter 4. The effects of this scattering mechanism on transport signatures are described by Boltzmann transport theory. The equilibrium occupation of a state in band n with crystal momentum $\mathbf{k}$ and energy $\varepsilon_{n,\mathbf{k}}$ is given by the Fermi-Dirac distribution

$$f(\varepsilon_{n,\mathbf{k}}) = \left(\exp\left(\frac{\varepsilon_{n,\mathbf{k}} - \mu}{k_B T} \right) + 1 \right)^{-1}, \tag{2.20}$$

where μ is the chemical potential, T is the temperature, and k_B is the Boltzmann constant. $\varepsilon_{n,\mathbf{k}}$ and μ are referenced to the conduction-band minimum. The Boltzmann transport equation describes the effects of external forces, diffusion, and internal collisions on the time evolution of the distribution function:

$$\mathbf{v} \cdot \nabla f + \frac{e}{\hbar} \mathbf{E} \cdot \frac{\partial f}{\partial \mathbf{k}} = \left(\frac{\partial f}{\partial t} \right)_{\text{scatt}}. \tag{2.21}$$

We introduce $\Phi_{n,\mathbf{k}}$, the deviation of the distribution function from equilibrium:

$$f_{n,\mathbf{k}} = f(\varepsilon_{n,\mathbf{k}}) + \Phi_{n,\mathbf{k}} \frac{\partial f(\varepsilon)}{\partial \varepsilon} \,. \tag{2.22}$$

Letting X be the left-hand side of Eq. (2.21) and P be an operator representing the effects of scattering, it can be shown [37] that Eq. (2.21) may be written as $X = P\Phi$. With the inner product $\langle A, B \rangle = \sum_n \int d\mathbf{k}\, AB$, this implies

$$\langle \Phi, X \rangle = \langle \Phi, P\Phi \rangle \,. \tag{2.23}$$

The variational principle established by Ziman in Ref. [37] shows that the solution Φ minimizes $\langle \Phi, P\Phi \rangle$. Using the trial function $\Phi = \mathbf{v} \cdot \hat{\mathbf{u}}$, where $\hat{\mathbf{u}}$ is the direction of the electric field, this gives a collision integral for electron-electron scattering [38]:

$$\begin{aligned} \langle \Phi, P\Phi \rangle = \; & \frac{1}{2k_B T} \frac{1}{(2\pi)^9} \frac{2\pi}{\hbar} \sum_{n_1,n_2,n_3,n_4} \int d\mathbf{k}_1 d\mathbf{k}_2 d\mathbf{k}_3 d\mathbf{k}_4 \\ & \times \left[\left(\mathbf{v}_{n_1,\mathbf{k}_1} + \mathbf{v}_{n_2,\mathbf{k}_2} - \mathbf{v}_{n_3,\mathbf{k}_3} - \mathbf{v}_{n_4,\mathbf{k}_4} \right) \cdot \hat{\mathbf{u}} \right]^2 \\ & \times f\left(\varepsilon_{n_1,\mathbf{k}_1}\right) f\left(\varepsilon_{n_2,\mathbf{k}_2}\right) \left[1 - f\left(\varepsilon_{n_3,\mathbf{k}_3}\right)\right] \left[1 - f\left(\varepsilon_{n_4,\mathbf{k}_4}\right)\right] \\ & \times \left(U^{(\mathrm{eff})}_{\mathbf{k}_1,\mathbf{k}_3} \right)^2 \delta\left(\varepsilon_{n_1,\mathbf{k}_1} + \varepsilon_{n_2,\mathbf{k}_2} - \varepsilon_{n_3,\mathbf{k}_3} - \varepsilon_{n_4,\mathbf{k}_4} \right) \\ & \times \delta\left(\mathbf{k}_1 + \mathbf{k}_2 - \mathbf{k}_3 - \mathbf{k}_4 \right) \,. \end{aligned} \tag{2.24}$$

This represents scattering between two electrons in bands n and n' with initial momenta $\mathbf{k}_1$ and $\mathbf{k}_2$ and final momenta $\mathbf{k}_3$ and $\mathbf{k}_4$. $U^{(\mathrm{eff})}_{\mathbf{k}_1,\mathbf{k}_3}$ is the effective interaction for the momentum transfer $\mathbf{k}_3 - \mathbf{k}_1$, and $\mathbf{v}_{n,\mathbf{k}} = 1/\hbar \; \partial\varepsilon/\partial\mathbf{k}$ is the band velocity. Note that momentum conservation sends the velocity term (and thus the entire expression) to zero in the absence of a mechanism for "momentum relaxation". This can be provided by Umklapp processes ($\mathbf{k}_1 + \mathbf{k}_2 - \mathbf{k}_3 - \mathbf{k}_4 = \mathbf{G}$, a lattice vector) or by scattering between states with

different masses [39].

Eq. (2.24) can be normalized to give the resistivity:

$$\rho_{\text{el-el}} = \mathcal{N}\langle\Phi, P\Phi\rangle \text{ , with } \mathcal{N} = [\langle\Phi, X(E=1)\rangle]^{-2} \text{ ,} \tag{2.25}$$

where $X(E=1)$ indicates the left-hand side of the Boltzmann transport equation with a unit electric field. The normalization factor $\mathcal{N}$ is given by

$$\mathcal{N} = \frac{(2\pi)^6}{4e^2}\left[\sum_n \int d\mathbf{k}\mathbf{v}_{n,\mathbf{k}}\Phi_{n,\mathbf{k}}\frac{\partial f(\varepsilon_{n,vk})}{\partial \varepsilon_{n,\mathbf{k}}}\right]^{-2} . \tag{2.26}$$

2.9.1 $U^{(\text{eff})}$

The form of $U^{(\text{eff})}$ for the electron-electron interaction including Coulomb, optical phonon-mediated, and acoustic phonon-mediated terms is [38]

$$U^{(\text{eff})} = U_C + U_{\text{op}} + U_{\text{ac}} \tag{2.27}$$

$$U_C = \frac{4\pi e^2}{\varepsilon_\infty\left(\kappa_s^2 + q^2\right)} \tag{2.28}$$

$$U_{op} = -\sum_\lambda \frac{2\left|V_{\mathbf{q},\lambda}\right|^2}{\hbar\omega_{\mathbf{q},\lambda}\left(\epsilon_e(\mathbf{q})\right)^2} \tag{2.29}$$

$$U_{ac} = -\frac{2\left|V_{\mathbf{q}}^{(ac)}\right|^2}{\hbar\omega_{\mathbf{q}}^{(ac)}} . \tag{2.30}$$

Coulomb term

The Coulomb term (in Gaussian units) is

$$U_C = \frac{4\pi e^2}{\varepsilon_\infty\left(\kappa_s^2 + q^2\right)} . \tag{2.31}$$

A common form of the screening length κ_s is given by the Thomas-Fermi approximation

$$\kappa_s^2 = \frac{6\pi e^2 n_0}{\varepsilon_\infty E_F} \,. \tag{2.32}$$

This form has limited applicability. In particular, it is ill-defined when E_F is negative, so we use a generalized Thomas-Fermi screening [40], which is also described as Lindhard screening:

$$\kappa_s^2 = \frac{4\pi e^2}{\varepsilon_\infty} \frac{\partial n}{\partial \mu} \,. \tag{2.33}$$

We use ε_∞ since the scattering is on a shorter timescale than atomic motion. We calculate the derivative numerically.

Some numerical results for these constants follow. In cgs units, $e = 4.803 \times 10^{-10}$ statC. (Note that statC is the cgs unit of charge, and is equivalent to cm $\sqrt{\text{dyn}} = \sqrt{\text{cm erg}}$.) Thus, $e^2 = 2.307 \times 10^{-19}$ cm erg $= 1.440 \times 10^{-7}$ cm eV $= 14.40$ eV Å. $4\pi e^2 = 180.95$ eV Å. When $\frac{\partial n}{\partial \mu}$ is expressed in eV^{-1} Å^{-3},

$$\kappa_s^2 = 180.95 \, \frac{\partial n}{\partial \mu} \text{ Å}^{-2} \,. \tag{2.34}$$

If q^2 is expressed in Å^{-2}, the Coulomb term is

$$U_C = \frac{4\pi e^2}{q^2 \varepsilon_\infty \epsilon_e(\mathbf{q})} = \frac{180.95}{q^2 \varepsilon_\infty \epsilon_e(\mathbf{q})} \text{ eV Å}^3 \,. \tag{2.35}$$

Optical term

We treat coupling between the electrons and the optical phonons through the Fröhlich model. Derivation of the Fröhlich coupling for multiple optical modes was provided by

Burak Himmetoglu and is reproduced here.

$$U_{op} = -\sum_{\lambda} \frac{2\left|V_{\mathbf{q},\lambda}\right|^2}{\hbar\omega_{\mathbf{q},\lambda}\left(\epsilon_e(\mathbf{q})\right)^2} \tag{2.36}$$

$$\epsilon_e(\mathbf{q}) = 1 + \frac{\kappa_s^2}{q^2} \tag{2.37}$$

$$V_{\mathbf{q},\lambda} = \frac{1}{q}\left(\frac{e^2\hbar\omega_{L,\lambda}}{2\varepsilon_0}\right)^{\frac{1}{2}} \frac{1}{\sqrt{\varepsilon_\infty}} \left[\frac{\prod_j \left(1-\frac{\omega_{T,j}^2}{\omega_{L,\lambda}^2}\right)}{\prod_{j\neq\lambda}\left(1-\frac{\omega_{L,j}^2}{\omega_{L,\lambda}^2}\right)}\right]^{\frac{1}{2}} \tag{2.38}$$

$$U_{op} = -\sum_{\lambda} \frac{2}{\hbar\omega_{\mathbf{q},\lambda}\left(\epsilon_e(\mathbf{q})\right)^2}\frac{1}{q^2}\frac{e^2\hbar\omega_{L,\lambda}}{2\varepsilon_0}\frac{1}{\varepsilon_\infty}\frac{\prod_j\left|1-\frac{\omega_{T,j}^2}{\omega_{L,\lambda}^2}\right|}{\prod_{j\neq\lambda}\left|1-\frac{\omega_{L,j}^2}{\omega_{L,\lambda}^2}\right|} \tag{2.39}$$

$$= -\frac{2e^2\hbar}{\hbar\left(\epsilon_e(\mathbf{q})\right)^2 q^2 2\varepsilon_0\varepsilon_\infty}\sum_{\lambda}\frac{\omega_{L,\lambda}}{\omega_{\mathbf{q},\lambda}}\frac{\prod_j\left|1-\frac{\omega_{T,j}^2}{\omega_{L,\lambda}^2}\right|}{\prod_{j\neq\lambda}\left|1-\frac{\omega_{L,j}^2}{\omega_{L,\lambda}^2}\right|} \tag{2.40}$$

$$= -\frac{e^2}{\varepsilon_0\varepsilon_\infty}\frac{q^2}{\left(q^2+\kappa_s^2\right)^2}\sum_{\lambda}\frac{\omega_{L,\lambda}}{\omega_{\mathbf{q},\lambda}}\frac{\prod_j\left|1-\frac{\omega_{T,j}^2}{\omega_{L,\lambda}^2}\right|}{\prod_{j\neq\lambda}\left|1-\frac{\omega_{L,j}^2}{\omega_{L,\lambda}^2}\right|} \tag{2.41}$$

$$= -\frac{180.95\ \text{Å eV}}{\varepsilon_\infty}\frac{q^2}{\left(q^2+\kappa_s^2\right)^2}\sum_{\lambda}\frac{\omega_{L,\lambda}}{\omega_{\mathbf{q},\lambda}}\frac{\prod_j\left|1-\frac{\omega_{T,j}^2}{\omega_{L,\lambda}^2}\right|}{\prod_{j\neq\lambda}\left|1-\frac{\omega_{L,j}^2}{\omega_{L,\lambda}^2}\right|} \tag{2.42}$$

Acoustic term

The acoustic-phonon-mediated term is given by [38]

$$U_{ac} = -\frac{2\left|V_{\mathbf{q}}^{(ac)}\right|^2}{\hbar\omega_{\mathbf{q}}^{(ac)}} \quad \text{where} \tag{2.43}$$

$$V_{\mathbf{q}}^{(ac)} = (4\pi\alpha_{ac})^{1/2}\frac{\hbar^2}{m_D}q^{1/2} \quad \text{and} \tag{2.44}$$

$$\alpha_{ac} = \frac{E_d^2 m_D^2}{8\pi n\hbar^3 v}\,, \tag{2.45}$$

$\omega_{\mathbf{q}} = vq$ is the acoustic phonon frequency, $n = 5.11\,\mathrm{g\,cm^{-3}}$ is the density of STO, E_d is the deformation potential, m_D is the density-of-states band mass, and $v = 8.1 \times 10^3\,\mathrm{m\,s^{-1}}$ is the speed of sound in STO. Note that m_D cancels out. Thus

$$U_{ac} = -\frac{2(4\pi\alpha_{ac})\frac{\hbar^4}{m_D^2}q}{\hbar\omega_q} = -\frac{8\pi\alpha_{ac}\hbar^3 q}{m_D^2\omega_q} = -\frac{8\pi E_d^2 m_D^2\hbar^3 q}{m_D^2\omega_q 8\pi n\hbar^3 v} = -\frac{E_d^2 q}{\omega_q n v}\,. \tag{2.46}$$

Assuming a linear phonon dispersion $\omega_q = vq$,

$$U_{ac} = -\frac{E_d^2}{nv^2} = -(0.477881\ \text{Å}^3\ \text{eV}^{-1})E_d^2\,. \tag{2.47}$$

2.9.2 Anisotropic parabola

It is desirable to contract the delta functions in 2.24 analytically, because numerical smearing of the delta functions introduces troublesome artifacts. We therefore follow Klimin *et al.* [38] and model the dispersion of $SrTiO_3$ as a set of 3 anisotropic parabolic bands

$$\varepsilon_1 = t_\delta\frac{a_0^2k_x^2}{4} + t_\pi\frac{a_0^2k_y^2}{4} + t_\pi\frac{a_0^2k_z^2}{4}\,, \tag{2.48}$$

$$\varepsilon_2 = t_\pi\frac{a_0^2k_x^2}{4} + t_\delta\frac{a_0^2k_y^2}{4} + t_\pi\frac{a_0^2k_z^2}{4}\,, \text{ and} \tag{2.49}$$

$$\varepsilon_3 = t_\pi\frac{a_0^2k_x^2}{4} + t_\pi\frac{a_0^2k_y^2}{4} + t_\delta\frac{a_0^2k_z^2}{4}\,, \tag{2.50}$$

where t_π is the curvature in the more dispersive direction, and t_δ is the curvature in the less dispersive direction. This is equivalent to

$$m_\pi = \frac{2\hbar^2}{a_0^2 t_\pi}\,, \qquad\qquad m_\delta = \frac{2\hbar^2}{a_0^2 t_\delta}\,. \tag{2.51}$$

The dispersion of the first band is

$$\varepsilon_1 = \frac{\hbar^2 k_x^2}{2m_\delta} + \frac{\hbar^2 k_y^2}{2m_\pi} + \frac{\hbar^2 k_z^2}{2m_\pi} \tag{2.52}$$

$$= \frac{\hbar^2 k_x^2 a_0^2 t_\delta}{4\hbar^2} + \frac{\hbar^2 k_y^2 a_0^2 t_\pi}{4\hbar^2} + \frac{\hbar^2 k_z^2 a_0^2 t_\pi}{4\hbar^2} \tag{2.53}$$

$$= t_\delta \frac{a_0^2 k_x^2}{4} + t_\pi \frac{a_0^2 k_y^2}{4} + t_\pi \frac{a_0^2 k_z^2}{4} \,. \tag{2.54}$$

Changing units to dimensionless k,

$$\varepsilon_1 = t_\delta \pi^2 k_x^2 + t_\pi \pi^2 k_y^2 + t_\pi \pi^2 k_z^2 \,. \tag{2.55}$$

The dispersions of the other bands are analogous.

2.9.3 Simplifying the collision integral

We now turn to a simplification of the collision integral [Eq. (2.24)]. A key aim is to analytically satisfy all the δ functions, leaving an integral which may be calculated numerically. Appendix A contains notes provided by J. T. Devreese and S. N. Klimin, which were very valuable in this endeavor. However, our goal is to test the claimed T^2 scaling, so we must avoid making various Fermi liquid approximations which lead to that T^2 behavior. These approximations will be discussed further in Sec. 4.3. For now, we begin with Eq. (16) from Devreese's notes, which contains the following expression for the collision integral:

$$\begin{aligned}\langle \Phi, P\Phi \rangle =& \frac{1}{2k_BT}\frac{1}{(2\pi)^9}\frac{2\pi}{\hbar}\hbar^2\frac{m_D^6}{\hbar^{14}}\sum_{n,n'}\left(\frac{1}{m_{zz}^{(n)}}-\frac{1}{m_{zz}^{(n')}}\right)^2 m_{zz}^{(n)}\int d\Omega_1\, d\Omega_2\, d\Omega_3\, d\Omega_4 \\ & \int \sqrt{2\varepsilon_1}d\varepsilon_1\,\sqrt{2\varepsilon_2}d\varepsilon_2\,\sqrt{2\varepsilon_3}d\varepsilon_3\,\sqrt{2\varepsilon_4}d\varepsilon_4\;\times\left(U^{(\mathrm{eff})}_{\mathbf{k}_1,\mathbf{k}_2}\right)^2 f\left(\varepsilon_{n,\mathbf{k}_1}\right) f\left(\varepsilon_{n',\mathbf{k}_2}\right) \\ & \left[1-f\left(\varepsilon_{n,\mathbf{k}_3}\right)\right]\left[1-f\left(\varepsilon_{n',\mathbf{k}_4}\right)\right]\left(p_1\cos\theta_1-p_3\cos\theta_3\right)^2 \\ & \delta\left(\varepsilon_{n,\mathbf{k}_1}+\varepsilon_{n',\mathbf{k}_2}-\varepsilon_{n,\mathbf{k}_3}-\varepsilon_{n',\mathbf{k}_4}\right)\delta\left(\mathbf{k}_1+\mathbf{k}_2-\mathbf{k}_3-\mathbf{k}_4\right)\,.\end{aligned} \tag{2.56}$$

Furthermore, on page 6, the notes indicate that

$$\delta(\mathbf{k}_1-\mathbf{k}_3+\mathbf{k}_2-\mathbf{k}_4)=\frac{\hbar^3}{m_D^{3/2}}\delta(\mathbf{p}_2-\mathbf{p}_4+\mathbf{Q}_{n,n'})\,, \tag{2.57}$$

and on page 7,

$$\int d\Omega_2\, d\Omega_4\,\delta(\mathbf{Q}_{n,n'}+\mathbf{p}_2-\mathbf{p}_4)=\frac{2\pi}{p_2p_4}\frac{1}{|\mathbf{Q}_{n,n'}|}\Theta\left(P_{\min}<|\mathbf{Q}_{n,n'}|<P_{\max}\right)\,, \tag{2.58}$$

where $P_{\min}=|p_2-p_4|$ and $P_{\max}=p_2+p_4$. We substitute these expressions into Eq. (2.24) to get an expression for the collision integral without the approximations made in Appendix A which, as we will argue, do not hold in $SrTiO_3$:

$$\begin{aligned}\langle \Phi, P\Phi \rangle =& \frac{1}{2k_BT}\frac{1}{(2\pi)^9}\frac{2\pi}{\hbar}\hbar^2\frac{m_D^6}{\hbar^{14}}\frac{\hbar^3}{m_D^{3/2}}2\pi\sum_{n,n'}\left(\frac{1}{m_{zz}^{(n)}}-\frac{1}{m_{zz}^{(n')}}\right)^2 m_{zz}^{(n)}\int d\Omega_1\, d\Omega_3 \\ & \int \sqrt{2\varepsilon_1}d\varepsilon_1\,\sqrt{2\varepsilon_2}d\varepsilon_2\,\sqrt{2\varepsilon_3}d\varepsilon_3\,\sqrt{2\varepsilon_4}d\varepsilon_4\;\times\left(U^{(\mathrm{eff})}_{\mathbf{k}_1,\mathbf{k}_2}\right)^2 f\left(\varepsilon_1\right) f\left(\varepsilon_2\right) \\ & \left[1-f\left(\varepsilon_3\right)\right]\left[1-f\left(\varepsilon_4\right)\right]\left(p_1\cos\theta_1-p_3\cos\theta_3\right)^2 \\ & \delta\left(\varepsilon_1+\varepsilon_2-\varepsilon_3-\varepsilon_4\right)\frac{1}{p_2p_4}\frac{1}{|\mathbf{Q}_{n,n'}|}\Theta\left(P_{\min}<|\mathbf{Q}_{n,n'}|<P_{\max}\right)\,.\end{aligned} \tag{2.59}$$

Since $p_j = \sqrt{2\varepsilon_j}$, the denominator cancels with ε factors from the integration measure. Carrying out this cancellation and contracting the delta functions,

$$\begin{aligned}
\langle \Phi, P\Phi \rangle =& \frac{1}{2k_BT}\frac{1}{(2\pi)^9}\frac{2\pi}{\hbar}\hbar^2\frac{m_D^6}{\hbar^{14}}\frac{\hbar^3}{m_D^{3/2}}2\pi\sum_{n,n'}\left(\frac{1}{m_{zz}^{(n)}}-\frac{1}{m_{zz}^{(n')}}\right)^2 m_{zz}^{(n)}\int d\Omega_1\, d\Omega_3 \qquad (2.60)\\
&\int \sqrt{2\varepsilon_1}d\varepsilon_1\, d\varepsilon_2\, \sqrt{2\varepsilon_3}d\varepsilon_3\ \times \left(U_{\mathbf{k}_1,\mathbf{k}_2}^{(\text{eff})}\right)^2 f(\varepsilon_1)\, f(\varepsilon_2)\\
&[1-f(\varepsilon_3)]\,[1-f(\varepsilon_1+\varepsilon_2-\varepsilon_3)]\left(\sqrt{2\varepsilon_1}\cos\theta_1-\sqrt{2\varepsilon_3}\cos\theta_3\right)^2\\
&\frac{1}{|\mathbf{Q}_{n,n'}|}\Theta\left(P_{\min}<|\mathbf{Q}_{n,n'}|<P_{\max}\right)\\
=&\frac{m_D^{9/2}}{k_BT(2\pi)^7\hbar^{10}}\sum_{n,n'}\left(\frac{1}{m_{zz}^{(n)}}-\frac{1}{m_{zz}^{(n')}}\right)^2 m_{zz}^{(n)}\int d\Omega_1\, d\Omega_3\, d\varepsilon_1\, d\varepsilon_2\, d\varepsilon_3 \qquad (2.61)\\
&\sqrt{\varepsilon_1\varepsilon_3}\left(U_{\mathbf{k}_1,\mathbf{k}_2}^{(\text{eff})}\right)^2 f(\varepsilon_1)\, f(\varepsilon_2)\,[1-f(\varepsilon_3)]\,[1-f(\varepsilon_1+\varepsilon_2-\varepsilon_3)]\\
&\left(\sqrt{2\varepsilon_1}\cos\theta_1-\sqrt{2\varepsilon_3}\cos\theta_3\right)^2\frac{1}{|\mathbf{Q}_{n,n'}|}\Theta\left(P_{\min}<|\mathbf{Q}_{n,n'}|<P_{\max}\right)\\
=&\frac{m_D^{9/2}}{k_BT(2\pi)^7\hbar^{10}}\sum_{n,n'}\left(\frac{1}{m_{zz}^{(n)}}-\frac{1}{m_{zz}^{(n')}}\right)^2 m_{zz}^{(n)}\frac{\hbar^6}{m_D^3}\int d\mathbf{k}_1\, d\mathbf{k}_3\, d\varepsilon_2 \qquad (2.62)\\
&\left(U_{\mathbf{k}_1,\mathbf{k}_2}^{(\text{eff})}\right)^2 f(\varepsilon_1)\, f(\varepsilon_2)\,[1-f(\varepsilon_3)]\,[1-f(\varepsilon_1+\varepsilon_2-\varepsilon_3)]\\
&\left(\sqrt{2\varepsilon_1}\cos\theta_1-\sqrt{2\varepsilon_3}\cos\theta_3\right)^2\frac{1}{|\mathbf{Q}_{n,n'}|}\Theta\left(P_{\min}<|\mathbf{Q}_{n,n'}|<P_{\max}\right)\\
=&\frac{m_D^{3/2}}{k_BT(2\pi)^7\hbar^4}\sum_{n,n'}\left(\frac{1}{m_{zz}^{(n)}}-\frac{1}{m_{zz}^{(n')}}\right)^2 m_{zz}^{(n)}\int d\mathbf{k}_1\, d\mathbf{k}_3\, d\varepsilon_2 \qquad (2.63)\\
&\left(U_{\mathbf{k}_1,\mathbf{k}_2}^{(\text{eff})}\right)^2 f(\varepsilon_1)\, f(\varepsilon_2)\,[1-f(\varepsilon_3)]\,[1-f(\varepsilon_1+\varepsilon_2-\varepsilon_3)]\\
&\left(\sqrt{2\varepsilon_1}\cos\theta_1-\sqrt{2\varepsilon_3}\cos\theta_3\right)^2\frac{1}{|\mathbf{Q}_{n,n'}|}\Theta\left(P_{\min}<|\mathbf{Q}_{n,n'}|<P_{\max}\right)\\
=&\frac{m_D^{3/2}}{2\pi k_BT\hbar^4a^6}\sum_{n,n'}\left(\frac{1}{m_{zz}^{(n)}}-\frac{1}{m_{zz}^{(n')}}\right)^2 m_{zz}^{(n)}\int_{-1/2}^{1/2}d\mathbf{k}_1\, d\mathbf{k}_3\int_0^{\varepsilon_{max}}d\varepsilon_2 \qquad (2.64)\\
&\left(U_{\mathbf{k}_1,\mathbf{k}_2}^{(\text{eff})}\right)^2 f(\varepsilon_1)\, f(\varepsilon_2)\,[1-f(\varepsilon_3)]\,[1-f(\varepsilon_1+\varepsilon_2-\varepsilon_3)]\\
&\left(\sqrt{2\varepsilon_1}\cos\theta_1-\sqrt{2\varepsilon_3}\cos\theta_3\right)^2\frac{1}{|\mathbf{Q}_{n,n'}|}\Theta\left(P_{\min}<|\mathbf{Q}_{n,n'}|<P_{\max}\right).
\end{aligned}$$

We note that

$$\cos\theta_1 = \frac{p_{1,z}}{p_1} \qquad \sqrt{2\varepsilon_1}\cos\theta_1 = p_{1,z}\,. \tag{2.65}$$

Therefore,

$$\begin{aligned}\langle \Phi, P\Phi\rangle =& \frac{m_D^{3/2}}{2\pi k_B T\hbar^4 a^6}\sum_{n,n'}\left(\frac{1}{m_{zz}^{(n)}}-\frac{1}{m_{zz}^{(n')}}\right)^2 m_{zz}^{(n)}\int_{-1/2}^{1/2} d\mathbf{k}_1\, d\mathbf{k}_3\int_0^{\varepsilon_{max}} d\varepsilon_2 \\ & \left(U^{(\text{eff})}_{\mathbf{k}_1,\mathbf{k}_2}\right)^2 f(\varepsilon_1)\, f(\varepsilon_2)\,[1-f(\varepsilon_3)]\,[1-f(\varepsilon_1+\varepsilon_2-\varepsilon_3)] \\ & (p_{1,z}-p_{3,z})^2\,\frac{1}{|\mathbf{Q}_{n,n'}|}\Theta\left(P_{\min}<|\mathbf{Q}_{n,n'}|<P_{\max}\right)\,.\end{aligned} \tag{2.66}$$

Verification

Now that we have arrived at a simplified expression without the Fermi liquid approximations, we verify that this expression replicates the results from Ref. [38] when their assumptions are in place.

$$\begin{aligned}\frac{\hbar}{\tau} =& (k_B T)^2\frac{\pi}{192}\frac{n_0}{(4\pi)^2}\frac{m_D^{3/2}m_b}{\hbar^3\mu^3}p_\mu^4\sum_{n,n'}\left(\frac{1}{m_{zz}^{(n)}}-\frac{1}{m_{zz}^{(n')}}\right)^2 m_{zz}^{(n)} \\ & \times\int_0^\pi \sin\theta_1\, d\theta_1\int_0^\pi \sin\theta_3\, d\theta_3\int_0^{2\pi} d\varphi_1\int_0^{2\pi} d\varphi_3\left(U^{(\text{eff})}_{\mathbf{k}_1,\mathbf{k}_2}\right)^2 \\ & \times\frac{(\cos\theta_1-\cos\theta_3)^2}{|\mathbf{Q}_{n,n'}|}\Theta(2p_\mu-|\mathbf{Q}_{n,n'}|)\,.\end{aligned} \tag{2.67}$$

This matches Klimin's result [38]. Converting to resistivity requires

$$\frac{\hbar}{\tau} = \frac{\hbar\omega_p^2}{4\pi}\rho\,, \qquad \omega_p^2 = \frac{4\pi e^2 n_0}{m_b}\,. \tag{2.68}$$

Therefore Klimin's result may also be written

$$\begin{aligned}\rho =&(k_BT)^2\frac{\pi}{192}\frac{1}{(4\pi)^2e^2}\frac{m_D^{3/2}m_b^2}{\hbar^4\mu^3}p_\mu^4\sum_{n,n'}\left(\frac{1}{m_{zz}^{(n)}}-\frac{1}{m_{zz}^{(n')}}\right)^2 m_{zz}^{(n)} \\ &\times\int_0^\pi \sin\theta_1\,d\theta_1\int_0^\pi \sin\theta_3\,d\theta_3\int_0^{2\pi}d\varphi_1\int_0^{2\pi}d\varphi_3\left(U^{(\mathrm{eff})}_{\mathbf{k}_1,\mathbf{k}_2}\right)^2 \\ &\times\frac{(\cos\theta_1-\cos\theta_3)^2}{|\mathbf{Q}_{n,n'}|}\Theta(2p_\mu-|\mathbf{Q}_{n,n'}|)\,.\end{aligned} \tag{2.69}$$

Approximation: $p_j \to p_\mu$

We make the approximation that p_j is given by its value at the Fermi level. As discussed on page 7 of the notes in Appendix A, this approximation allows Eq. (2.69) to be derived from 2.56, reproduced below:

$$\begin{aligned}\langle\Phi,P\Phi\rangle =&\frac{1}{2k_BT}\frac{1}{(2\pi)^9}\frac{2\pi}{\hbar}\hbar^2\frac{m_D^6}{\hbar^{14}}\sum_{n,n'}\left(\frac{1}{m_{zz}^{(n)}}-\frac{1}{m_{zz}^{(n')}}\right)^2 m_{zz}^{(n)}\int d\Omega_1\,d\Omega_2\,d\Omega_3\,d\Omega_4 \\ &\int\sqrt{2\varepsilon_1}d\varepsilon_1\sqrt{2\varepsilon_2}d\varepsilon_2\sqrt{2\varepsilon_3}d\varepsilon_3\sqrt{2\varepsilon_4}d\varepsilon_4\;\times\left(U^{(\mathrm{eff})}_{\mathbf{k}_1,\mathbf{k}_2}\right)^2 f\left(\varepsilon_{n,\mathbf{k}_1}\right)f\left(\varepsilon_{n',\mathbf{k}_2}\right) \\ &\left[1-f\left(\varepsilon_{n,\mathbf{k}_3}\right)\right]\left[1-f\left(\varepsilon_{n',\mathbf{k}_4}\right)\right]\left(p_1\cos\theta_1-p_3\cos\theta_3\right)^2 \\ &\delta\left(\varepsilon_{n,\mathbf{k}_1}+\varepsilon_{n',\mathbf{k}_2}-\varepsilon_{n,\mathbf{k}_3}-\varepsilon_{n',\mathbf{k}_4}\right)\delta\left(\mathbf{k}_1+\mathbf{k}_2-\mathbf{k}_3-\mathbf{k}_4\right)\,.\end{aligned} \tag{2.70}$$

There are three steps involved. One is

$$\delta(\mathbf{k}_1-\mathbf{k}_3+\mathbf{k}_2-\mathbf{k}_4)=\frac{\hbar^3}{m_D^{3/2}}\delta(\mathbf{p}_2-\mathbf{p}_4+\mathbf{Q}_{n,n'}) \tag{2.71}$$

$$\int d\Omega_2\,d\Omega_4\,\delta(\mathbf{Q}_{n,n'}+\mathbf{p}_2-\mathbf{p}_4)=\frac{2\pi}{p_2p_4}\frac{1}{|\mathbf{Q}_{n,n'}|}\Theta\left(P_{\min}<|\mathbf{Q}_{n,n'}|<P_{\max}\right)\,. \tag{2.72}$$

Eqs. 2.71 and 2.72 hold without any approximations. For the second step, we note that

$$\varepsilon_4=\varepsilon_1+\Delta \qquad \text{and} \qquad \varepsilon_3=\varepsilon_2+\Delta'\,. \tag{2.73}$$

The delta function $\delta(\varepsilon_1+\varepsilon_2-\varepsilon_3-\varepsilon_4)$ guarantees $\Delta'=-\Delta$.

$$\int d\varepsilon_1\, d\varepsilon_2\, d\varepsilon_3\, d\varepsilon_4\, f(\varepsilon_1)\, f(\varepsilon_2)\,[1-f(\varepsilon_3)]\,[1-f(\varepsilon_4)]\,\delta(\varepsilon_1+\varepsilon_2-\varepsilon_3-\varepsilon_4) \tag{2.74}$$

$$=\int d\varepsilon_1\, d\varepsilon_2\, d\varepsilon_3\, f(\varepsilon_1)\, f(\varepsilon_2)\,[1-f(\varepsilon_3)]\,[1-f(\varepsilon_1+\varepsilon_2-\varepsilon_3)] \tag{2.75}$$

$$=\int_{-\varepsilon_1}^{\varepsilon_2} d\Delta \int_0^\infty d\varepsilon_1\, f(\varepsilon_1)\,[1-f(\varepsilon_1+\Delta)] \int_0^\infty d\varepsilon_2\, f(\varepsilon_2)\,[1-f(\varepsilon_2-\Delta)] \tag{2.76}$$

$$=(k_BT)^3\int_{-\infty}^{\infty} z^2\frac{e^{-z}}{(1-e^{-z})^2}dz=\frac{2\pi^2}{3}(k_BT)^3\,. \tag{2.77}$$

This has been verified numerically in the case $\mu \gg k_BT$. However, this is the key source of the T^2 scaling, and the integral does not give T^2 in intermediate regimes (see Sec. 4.3.3), so we must retain the integral to be done numerically at each desired temperature.

$$\begin{aligned}\frac{\hbar}{\tau} =&\frac{1}{k_BT}\frac{1}{128\pi}\frac{n_0}{(4\pi)^2}\frac{m_D^{3/2}m_b}{\hbar^3\mu^3}p_\mu^4\sum_{n,n'}\left(\frac{1}{m_{zz}^{(n)}}-\frac{1}{m_{zz}^{(n')}}\right)^2 m_{zz}^{(n)}\int d\varepsilon_1\, d\varepsilon_2\, d\varepsilon_3\, d\varepsilon_4 \\ &\times f(\varepsilon_1)\, f(\varepsilon_2)\,[1-f(\varepsilon_3)]\,[1-f(\varepsilon_1+\varepsilon_2-\varepsilon_3)]\int_0^\pi \sin\theta_1\, d\theta_1\int_0^\pi \sin\theta_3\, d\theta_3 \\ &\times\int_0^{2\pi} d\varphi_1\int_0^{2\pi} d\varphi_3\left(U^{(\mathrm{eff})}_{\mathbf{k}_1,\mathbf{k}_2}\right)^2\ \frac{(\cos\theta_1-\cos\theta_3)^2}{|\mathbf{Q}_{n,n'}|}\Theta(2p_\mu-|\mathbf{Q}_{n,n'}|)\,.\end{aligned} \tag{2.78}$$

Distributing p_μ^4 back into the integral,

$$\begin{aligned}\frac{\hbar}{\tau} =&\frac{1}{k_BT}\frac{1}{128\pi}\frac{n_0}{(4\pi)^2}\frac{m_D^{3/2}m_b}{\hbar^3\mu^3}\sum_{n,n'}\left(\frac{1}{m_{zz}^{(n)}}-\frac{1}{m_{zz}^{(n')}}\right)^2 m_{zz}^{(n)}\int \sqrt{2\mu}\, d\varepsilon_1\,\sqrt{2\mu}\, d\varepsilon_2\,\sqrt{2\mu}\, d\varepsilon_3 \\ &\times\int \sqrt{2\mu}\, d\varepsilon_4\, f(\varepsilon_1)\, f(\varepsilon_2)\,[1-f(\varepsilon_3)]\,[1-f(\varepsilon_1+\varepsilon_2-\varepsilon_3)]\int_0^\pi \sin\theta_1\, d\theta_1\int_0^\pi \sin\theta_3\, d\theta_3 \\ &\times\int_0^{2\pi} d\varphi_1\int_0^{2\pi} d\varphi_3\left(U^{(\mathrm{eff})}_{\mathbf{k}_1,\mathbf{k}_2}\right)^2\ \frac{(\sqrt{2\mu}\,\cos\theta_1-\sqrt{2\mu}\,\cos\theta_3)^2}{\sqrt{2\mu}\,\sqrt{2\mu}\,|\mathbf{Q}_{n,n'}|}\Theta(2p_\mu-|\mathbf{Q}_{n,n'}|)\,.\end{aligned} \tag{2.79}$$

Calculating resistivity from scattering rate

The plasma frequency is

$$\omega_p^2 = \frac{4\pi e^2 n_0}{m_b} \,. \tag{2.80}$$

This allows

$$\rho = \frac{4\pi}{\omega_p^2 \hbar} \frac{\hbar}{\tau} = \frac{m_b}{e^2 n_0 \hbar} \frac{\hbar}{\tau} \,. \tag{2.81}$$

Final simplification

We have

$$\begin{aligned} \frac{\hbar}{\tau} =& \frac{1}{k_B T} \frac{1}{128\pi} \frac{n_0}{(4\pi)^2} \frac{m_D^{3/2} m_b}{\hbar^3 \mu^3} \sum_{n,n'} \left(\frac{1}{m_{zz}^{(n)}} - \frac{1}{m_{zz}^{(n')}} \right)^2 m_{zz}^{(n)} \int p_1 \, d\varepsilon_1 \, p_2 \, d\varepsilon_2 \, p_3 \, d\varepsilon_3 \, p_4 \\ & \times f\left(\varepsilon_1\right) f\left(\varepsilon_2\right) \left[1 - f\left(\varepsilon_3\right)\right] \left[1 - f\left(\varepsilon_1 + \varepsilon_2 - \varepsilon_3\right)\right] \int_0^\pi \sin\theta_1 \, d\theta_1 \int_0^\pi \sin\theta_3 \, d\theta_3 \\ & \times \int_0^{2\pi} d\varphi_1 \int_0^{2\pi} d\varphi_3 \left(U_{\mathbf{k}_1, \mathbf{k}_2}^{(\mathrm{eff})} \right)^2 \frac{\left(p_1 \, \cos\theta_1 - p_3 \, \cos\theta_3\right)^2}{p_2 p_4 \, |\mathbf{Q}_{n,n'}|} \Theta(2p_\mu - |\mathbf{Q}_{n,n'}|) \,. \end{aligned} \tag{2.82}$$

Converting to resistivity,

$$\begin{aligned} \rho =& \frac{1}{k_B T} \frac{1}{128\pi} \frac{1}{e^2 (4\pi)^2} \frac{m_D^{3/2} m_b^2}{\hbar^4 \mu^3} \sum_{n,n'} \left(\frac{1}{m_{zz}^{(n)}} - \frac{1}{m_{zz}^{(n')}} \right)^2 m_{zz}^{(n)} \int p_1 \, d\varepsilon_1 \, p_2 \, d\varepsilon_2 \, p_3 \, d\varepsilon_3 \, p_4 \\ & \times f\left(\varepsilon_1\right) f\left(\varepsilon_2\right) \left[1 - f\left(\varepsilon_3\right)\right] \left[1 - f\left(\varepsilon_1 + \varepsilon_2 - \varepsilon_3\right)\right] \int_0^\pi \sin\theta_1 \, d\theta_1 \int_0^\pi \sin\theta_3 \, d\theta_3 \\ & \times \int_0^{2\pi} d\varphi_1 \int_0^{2\pi} d\varphi_3 \left(U_{\mathbf{k}_1, \mathbf{k}_2}^{(\mathrm{eff})} \right)^2 \frac{\left(p_1 \, \cos\theta_1 - p_3 \, \cos\theta_3\right)^2}{p_2 p_4 \, |\mathbf{Q}_{n,n'}|} \Theta(2p_\mu - |\mathbf{Q}_{n,n'}|) \,. \end{aligned} \tag{2.83}$$

However, this expression still contains the denominator evaluated in the fixed-μ approximation

$$[\langle\Phi, X(E=1)\rangle]^2 = e^2 \frac{8}{\pi^4} \frac{\mu^3}{\hbar^6} \frac{m_D^3}{m_b^2} \,. \tag{2.84}$$

Removing this from the expression for the resistivity, we have a final expression for the main integral

$$\begin{aligned}\langle\Phi, P\Phi\rangle =& \frac{1}{2k_BT} \frac{1}{(2\pi)^7} \frac{m_D^{9/2}}{\hbar^{10}} \sum_{n,n'} \left(\frac{1}{m_{zz}^{(n)}} - \frac{1}{m_{zz}^{(n')}} \right)^2 m_{zz}^{(n)} \int p_1 \, d\varepsilon_1 \, p_2 \, d\varepsilon_2 \, p_3 \, d\varepsilon_3 \, p_4 \\ & \times f(\varepsilon_1) \, f(\varepsilon_2) \left[1 - f(\varepsilon_3)\right] \left[1 - f(\varepsilon_1 + \varepsilon_2 - \varepsilon_3)\right] \int_0^\pi \sin\theta_1 \, d\theta_1 \int_0^\pi \sin\theta_3 \, d\theta_3 \\ & \times \int_0^{2\pi} d\varphi_1 \int_0^{2\pi} d\varphi_3 \left(U_{\mathbf{k}_1,\mathbf{k}_2}^{(\text{eff})} \right)^2 \frac{(p_1 \cos\theta_1 - p_3 \cos\theta_3)^2}{p_2 p_4 \, |\mathbf{Q}_{n,n'}|} \Theta(2p_\mu - |\mathbf{Q}_{n,n'}|) \,.\end{aligned} \tag{2.85}$$

This can also be derived from Eq. (2.56) by applying Eqs. (2.71) and (2.72). All that remains is to explicitly calculate the denominator

$$[\langle\Phi, X(E=1)\rangle]^2 = \frac{4e^2}{(2\pi)^6} \left[\sum_n \int d\mathbf{k} v_{n,\mathbf{k}} \Phi_{n,\mathbf{k}} \frac{\partial f(\varepsilon_{n,vk})}{\partial \varepsilon_{n,\mathbf{k}}} \right]^2 , \tag{2.86}$$

or in reduced units,

$$[\langle\Phi, X(E=1)\rangle]^2 = \frac{4e^2}{a^6} \left[\sum_n \int d\mathbf{k} v_{n,\mathbf{k}} \Phi_{n,\mathbf{k}} \frac{\partial f(\varepsilon_{n,vk})}{\partial \varepsilon_{n,\mathbf{k}}} \right]^2 . \tag{2.87}$$

Eqs. 2.24, 2.85, and 2.87 represent the final equations which we implement in code in order to calculate the electron-electron scattering rate.

2.9.4 Code

The code used to calculate electron-electron scattering rates is written in C and uses Divonne, a Monte Carlo integration algorithm which uses stratified sampling for variance reduction, as implemented in the CUBA package [41]. The full code may be found at

`https://bitbucket.org/numenorean7/electron-electron/`.

Chapter 3

Shallow Donors in Silicon

3.1 Introduction

Doped semiconductors are well known as the heart of modern electronics, but they are also an exciting platform for novel quantum computation in the form of spin-based qubits. Doping of semiconductors is typically accomplished through the introduction of so-called "shallow" impurities that contribute carriers to the delocalized band states: electrons to the conduction-band minimum (CBM) in the case of shallow donors (n-type doping) or holes to the valence-band maximum (VBM) in the case of shallow acceptors (p-type doping).

A shallow donor is an impurity with charge +1 relative to the host crystal (in the case of a single donor) which donates an electron to the conduction band. A shallow acceptor behaves similarly with opposite sign of the charges. According to "effective-mass theory" (discussed in Sec. 2.8.1), a donor modifies the band occupied by the donated electron much like a point charge modifies the vacuum states. This creates "hydrogenic" states in which the electron is loosely bound to the donor, analogous to the bonding of an electron to a proton in a free hydrogen atom. Originally studied by Kohn and Luttinger

in the 1950s [16, 17, 42, 18], this model has been extended and improved, but still faces limitations due to its intrinsic approximations. Within hydrogenic effective mass theory, screening of the impurity potential is approximated by using the macroscopic dielectric constant, but actual screening by the valence electrons proceeds in complex material- and impurity-dependent ways. These are known as "central-cell" effects (see Sec. 2.8.3). Further complications arise from the fact that the conduction-band minimum of silicon is a set of six degenerate valleys [19]. These six valleys are not independent, but mix and split through a process known as "valley-orbit coupling". Group theoretic arguments show that the CBM splits into states corresponding to irreducible representations of the T_d symmetry group: singlet A_1 (the ground state), doublet E, and triplet T_2 (see Sec. 2.8.2).

Developments in the treatment of shallow impurities have largely focused on corrections for these effects and attempts to include them in models. [25, 23, 26, 27, 20] Within effective mass theory, this effort has met with success largely through the use of empirical fitting parameters. It is desirable to avoid fitting to experimental input and to calculate properties of shallow impurities from first principles. This effort has met with some success using a variety of techniques (as discussed in Sec. 3.2), but accuracy has been limited by electron overdelocalization of traditional functionals and by the large size of the donor wavefunction compared to typical simulation-cell sizes. We overcome these obstacles by using a hybrid functional to provide a correct description of localization, and demonstrate a simple extrapolation to the dilute limit using traditional functionals. This technique provides results that are in excellent agreement with experiment.

Our ability to model shallow donors using first-principles methods provides valuable background for the engineering of silicon-based spin qubits [43, 44]. This theoretical understanding also allows us to explain an unusual phenomenon observed in experiments by Pla *et al.* [45] These experiments use electron spin resonance (ESR) to measure tran-

sitions between total-spin states of the coupled electron-nucleus spin degree of freedom of shallow bismuth donors in silicon. They observe a split Hahn echo peak corresponding to the $|4,-4\rangle \leftrightarrow |5,-5\rangle$ transition. Orientation-dependent measurements suggest that this results from strain caused by the thermal contraction of an aluminum resonator patterned on the surface of the sample.

This result raises the question: how does strain cause such a dramatic splitting in the ESR line? Traditionally, strain effects have been explained through the "valley repopulation model" [46], which describes changes in the valley-orbit ground state caused by shifts of the conduction-band valleys. This model provides no explanation for the observed ESR splittings. Pla *et al.* proposed a possible mechanism involving a term in the ESR Hamiltonian which couples the quadrupole moment of the donor nucleus with the electric field gradient (EFG) induced by the electron wavefunction. Their model included a parameter γ, which enters as a scaling term in the quadrupole Hamiltonian. The main contribution to this term should be the Sternheimer antishielding factor, a measure of how the core electrons amplify an externally-applied EFG (in this case coming from the shallow donor wavefunction). Isolated Bi^+ ions have $\gamma = -925.6$. They find that $\gamma = -900$ fits their data. It remains to be seen whether this value of γ is realistic for a bismuth donor in silicon. Other observations, such as g-factor anisotropy, are also not well explained by the quadrupole mechanism. [45] *Ab initio* calculations using the projector-augmented-wave method have successfully determined EFGs at nuclei without using empirical corrections such as the Sternheimer antishielding factor [47]. An accurate calculation of the donor wavefunction will thus allow the determination of the EFG at the nucleus and the strength of the quadrupole coupling. Subsequent experiments by the Morton group identified an unexpectedly large dependency of the isotropic hyperfine parameter A on the hydrostatic component of strain [48]. We therefore also study strain effects on shallow donors using our first-principles technique.

3.2 First-principles studies of shallow impurities

Density functional theory (DFT) has been shown to correctly predict hyperfine parameters for localized defect states [34], but shallow states are more challenging due to the large extent of the wavefunction. Capturing this large extent within a supercell approach, which is the most commonly used technique to calculate impurities in solids [13], is extremely challenging. Calculations based on an impurity Green's function approach are in principle more suited (see Sec. 2.8.4), and have been successfully used to study the isotropic hyperfine parameter of shallow donors [35] and to explore their evolution for phosphorus donors at very high strain [36]. However, the Green's function technique is far less intuitive than the supercell approach, and is difficult to generalize.

To overcome the limitations of the supercell approach, Wang [49] used a potential patching method to calculate supercells up to 64,000 atoms, achieving modest success in the calculation of binding energies of some acceptors. Yamamoto *et al.* [22] modeled an As donor in Si by performing DFT calculations using the generalized gradient approximation (GGA) for supercells up to 10,648 atoms. They calculated binding energies based on wavefunctions extracted from the supercells combined with a model for the screened impurity potential, and found a good description of the Bohr radius and the binding energy. More recently, Smith *et al.* [50] used a similar approach for P in Si. These studies show that, while it is extremely difficult to capture the exponential tail of shallow impurity wavefunctions with first-principles methods, DFT is able to describe the wavefunction in the vicinity of the impurity. This is encouraging because the isotropic hyperfine coupling and quadrupole coupling both depend on the properties of the wavefunction at the donor nucleus. This also suggests that it may be possible to introduce a systematic correction for errors induced by the overlap of the exponential tail of the wavefunction into neighboring supercells.

In this work, we present DFT calculations of the arsenic and bismuth shallow donor in Si. Calculated values of the hyperfine parameter and donor binding energies are in good agreement with experiment in the isolated limit. We also demonstrate that the variation of the isotropic hyperfine parameter as a function of strain can be captured in feasible supercell calculations, correctly including central-cell and valley-orbit effects.

The present work is on silicon, but the same techniques should work for donors in other multivalley semiconductors such as germanium. Donors in single-valley semiconductors such as gallium arsenide are simpler due to the lack of multivalley effects, and are much better described by effective mass theory [20]. We also expect that our techniques can be generalized to shallow acceptors, including the treatment of the degeneracy at the valence-band maximum.

3.3 Computational methods

A general overview of our computational approach to modeling shallow donors may be found in Sec. 2.8. Here we discuss specifics of the methodology that are pertinent to the questions at hand.

3.3.1 Binding energies

The binding energy of a shallow donor can be obtained from the Kohn-Sham eigenvalues:

$$E_b = \epsilon_\Gamma^{\text{donor}} - \epsilon_\Gamma^{\text{CB}} + \Delta \tag{3.1}$$

where $\epsilon_\Gamma^{\text{donor}}$ is the Kohn-Sham eigenvalue of the occupied donor state (evaluated at Γ, as discussed in Sec. 3.3.6) and $\epsilon_\Gamma^{\text{CB}}$ is the Kohn-Sham eigenvalue of the conduction band in a bulk calculation of a supercell of the same size (also evaluated at Γ for consistency).

Because the Kohn-Sham eigenvalues are referenced to the average electrostatic potential, we must adjust for any shifts in the potential due to the presence of the impurity in order to meaningfully compare eigenvalues between bulk and impurity cells. Assuming the valence-band maximum is unperturbed by the presence of the donor impurity, this alignment may be accomplished by introducing the correction term $\Delta = \epsilon^{\mathrm{VBM,bulk}} - \epsilon^{\mathrm{VBM,defect}}$. This term aligns the Kohn-Sham levels between the bulk and donor cells, allowing for meaningful comparison.

3.3.2 Strain effects

The isotropic hyperfine parameter is given by Eq. (3) of Ref. [34]:

$$A = \frac{2\mu_0}{3} g_e \mu_B g_I \mu_N \left|\Psi(\mathbf{r})\right|^2 , \tag{3.2}$$

where g_e is the electron g-factor, g_I is the g-factor of the nucleus in question, μ_B is the Bohr magneton, mu_N is the nuclear magneton, and $\Psi(\mathbf{r})$ is the wavefunction at the nucleus. Symmetry restricts the form of the strain dependence of the isotropic hyperfine parameter [48]. Expanded to second order in strain, this dependence is given by

$$\begin{aligned} A/A_0 =& 1 + \frac{K}{3}(\epsilon_{xx} + \epsilon_{yy} + \epsilon_{zz}) \\ &+ \frac{L}{2}\left[(\epsilon_{yy} - \epsilon_{zz})^2 + (\epsilon_{yy} - \epsilon_{zz})^2 + (\epsilon_{yy} - \epsilon_{zz})^2\right] , \end{aligned} \tag{3.3}$$

where A_0 is the value in the absence of strain. Shear terms were also included in Ref. [48], but were shown to be negligible; they will not be discussed here. The valley repopulation model [46] predicts a quadratic dependence of $L = -2\Xi_u^2/(9\Delta^2)$, where $\Xi_u = 8.6$ eV is the uniaxial deformation potential of the CBM and Δ is the splitting between the A_1 and the E valley-orbit states. This gives a numerical value of $L = -9720$, in good agreement

with experiment [46, 36, 48].

Since hydrostatic strain acts on all the valleys equally, it will not lead to a repopulation effect. However, the magnitude of the wavefunction at the donor nucleus—which determines A—will be affected by hydrostatic strain, leading to a nonzero value of K. At the level of effective mass theory, a dependence on hydrostatic strain occurs through variations in the dielectric constant ε and effective mass m^*. The donor Bohr radius a_D is proportional to ε/m^* [19]. Literature shows that these properties vary linearly with small hydrostatic pressure. According to Ref. [51], $\Delta\varepsilon/\varepsilon = -2.8 \times 10^{-3}$ for $P = 1$ GPa, and according to Ref. [52], $\Delta m^*/m^* = -1.4 \times 10^{-3}$ for $P = 1800$ kg/cm^2. Using the bulk modulus of silicon (97.88 GPa) [53], these results give the dependence of ε and m^* on small hydrostatic strain $\epsilon_{xx} = \epsilon_{yy} = \epsilon_{zz} = \epsilon$:

$$\frac{\Delta\varepsilon}{\varepsilon} = 0.819\epsilon \text{ and } \frac{\Delta m^*}{m^*} = 2.322\epsilon\,. \tag{3.4}$$

The donor Bohr radius is therefore given by

$$a_D(\epsilon) = a_{D0}\frac{1 + 0.819\epsilon}{1 + 2.322\epsilon}\,. \tag{3.5}$$

The EMT wavefunction is proportional to $a_D^{-3/2}$ and the hyperfine parameter is proportional to the square of the wavefunction at the nucleus [Eq. (3.2)] [19]. Therefore the hyperfine parameter is

$$A(\epsilon) = A_0\frac{(1 + 2.322\epsilon)^3}{(1 + 0.819\epsilon)^3} = A_0\left(1 + 4.524\epsilon + \mathcal{O}(\epsilon^2)\right)\,. \tag{3.6}$$

In the notation of Eq. (3.3), this corresponds to $K = 4.524$. The experimentally observed value is $K = 19.1$ [48]. Within effective mass theory, the impact of hydrostatic strain is clearly not negligible, but it is also clearly not the dominant factor. Other

factors, such as central-cell effects which lead to mixing with the donor $2s$ states, also play a role [48]. We will use first-principles computations to capture these effects.

3.3.3 Density Functional Theory

We use DFT with the standard approach discussed in Chapter 2. Calculations employed the HSE functional with the standard parameters as well as the PBE functional.

Hyperfine parameters were calculated following the methodology described in Refs. [54] and [55], and electric field gradients and quadrupole couplings were calculated using the method of Ref. [47]. Calculations were performed in supercells that are $n \times n \times n$ multiples of the conventional 8-atom cubic cell. The largest PBE supercell corresponds to n=7, containing N=2744 atoms. The largest HSE supercell corresponds to n=4, containing N=512 atoms. Further details may be found in Sec. 2.8.

3.3.4 Finite size effects

The Bohr radius of a shallow donor in silicon within effective mass theory is approximately 23.8 Å. This is only slightly smaller than the side lengths of the largest ($n = 7$, $N = 2744$) supercells we use: 32.8 Å. The Coulomb envelope only drops to 1% of its central value 54.7 Å from the center. Therefore, a significant part of this exponential tail necessarily overlaps into neighboring supercells. We will therefore need to extrapolate to the $N \to \infty$ limit, where N is the number of atoms in the supercell, in order to calculate physical results. We expect that, for large enough supercells, the error will scale inversely with the volume of the supercell, or equivalently with $1/N$.

3.3.5 Occupation of states

Occupancies of the Kohn-Sham states in DFT are typically set through a "smearing" procedure. This is done to avoid various convergence issues that can arise when bands are partially occupied, and a scheme for extrapolating to zero smearing is typically included. This procedure is benign for most situations, but it leads to severe problems in this particular case. The energy spacing between valley-orbit split states of the donor wavefunction is approximately 10 meV, comparable in size to the smallest smearing parameters typically used; smearing will mix states other than the ground state into the final charge density. This is a problem because the A_1 state has a peak at the nucleus, while the other states have nodes. We are comparing to experiments performed at low temperature, so the measured properties are determined entirely by the ground state. Mixing with excited states of the donor will defeat any chance of calculating the hyperfine parameter correctly. To overcome this issue, we do not use smearing in our final calculations. This requires care to ensure proper convergence, but has proven feasible through the use of intermediate calculations which include small amounts (e.g. 0.01 eV) of smearing.

3.3.6 Brillouin zone sampling

The A_1 valley-orbit ground state is made up of a combination of all six conduction-band valley states. Therefore a correct calculation of the donor wavefunction must include contributions from each valley. For the equilibrium structure, and under hydrostatic strain, the six valleys are equivalent and equally occupied. Under uniaxial deformation, splitting of the valleys occurs, and ensuring correct sampling of all of the valleys (which is necessary to obtain the correct valley-orbit splitting) could be tricky.

Most of the supercells used in the present study are large enough to ensure that, in

reciprocal space, the conduction-band valleys are folded back to a point very close to the zone center. Therefore sampling the Brillouin zone at a single **k** point automatically allows for all of the proper interactions and mixing between the valleys in the self-consistent calculation. Our calculations use the Γ point to maintain an unbiased sampling of the valleys and to reduce the computational demand. A detailed analysis of Brillouin-zone sampling was included in Ref. [50], and also reached the conclusion that sampling at the Γ point provided reliable results.

We verified that our calculations capture the correct valley-orbit state through symmetry analysis of the wavefunction [see Sec. 3.4.5].

3.4 Results

3.4.1 Binding energies

Calculated binding energies for bismuth and arsenic shallow donors in silicon are shown in Fig. 3.1. For sufficiently large supercells, the error in the calculated binding energy comes from the exponential tail of the donor wavefunction, which extends into neighboring supercells. This error is expected to scale inversely with the volume of the supercell (see Sec. 3.3.4), and therefore we plot our results as a function of $1/N$ where N is the number of atoms in the supercell. Our results for bismuth donor supercells with $n \geq 4$ ($N \geq 512$) show a clear linear trend with $1/N$, allowing extrapolation to the $N \to \infty$ limit. Extrapolating PBE results gives a value of -21.4 meV for bismuth donors, significantly underestimating the experimental result of -70.9 meV [20]. For the arsenic donors, the PBE extrapolated value is -12.5 meV, compared to an experimental value of -53.8 meV [20].

This underestimation of the binding energy can be attributed to the over-delocalization

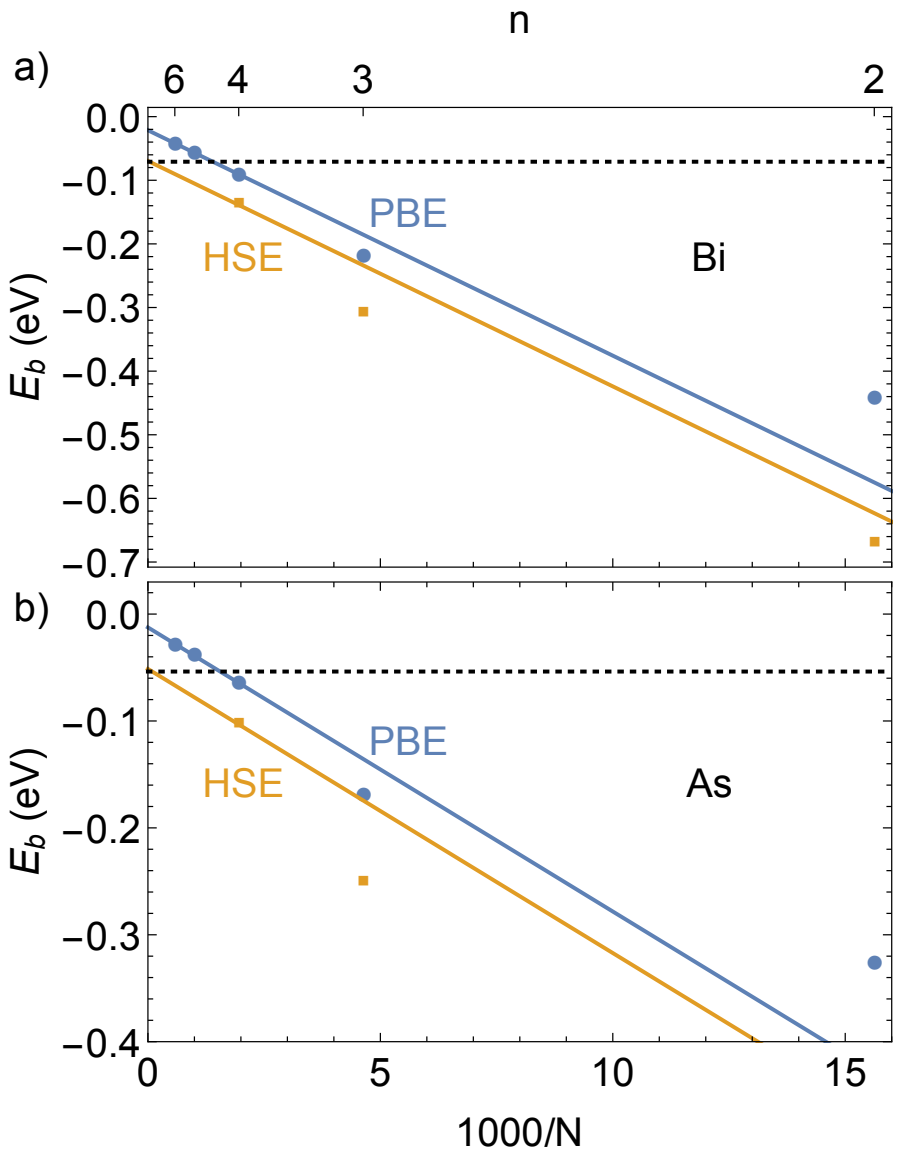

Figure 3.1: a) Binding energy [Eq. (3.1)] for a bismuth donor as a function of supercell size. PBE results are in blue circles and HSE results are in orange squares. The blue line is a linear fit to the PBE data for $n \geq 4, N \geq 512$: $E_b = -0.0214 - 35.4/N$. The orange line is an extrapolation from the HSE $n = 4, N = 512$ point using the PBE slope: $E_b = -0.0697 - 35.4/N$. This HSE extrapolated value of -69.7 meV is in excellent agreement with the experimental binding energy of -70.9 meV, shown as a black dashed line. b) Similar results for an arsenic donor. Blue PBE line fit to data with for $n \geq 4, N \geq 512$ is $E_b = -0.0125 - 26.6/N$, orange HSE line is $E_b = -0.0513 - 26.6/N$ This HSE extrapolated value of -51.3 meV is in very good agreement with the experimental binding energy of -53.8 meV.

of the wavefunctions inherent in PBE which results in a lower spin density close to the impurity site and thus a lower Coulomb attraction between the electron and the donor nucleus. This effect has been found in previous work on shallow impurities using DFT [22, 49, 50]. A better description of localization can be achieved with more sophisticated functionals, such as the HSE hybrid functional. The vastly greater computational cost of HSE does not allow the calculation of supercells large enough to reliably calculate all properties of the donor wavefunction; however, we are able to perform calculations up to n=4 (N=512) (see Fig. 3.2).

As we can see from the PBE results, results obtained with the N=512 (n=4) supercells are still far from the converged value; however, the PBE results also show that N=512 is within the regime in which the value of the hyperfine parameter A scales as $1/N$. We can therefore rely on the known PBE scaling (which we assume also applies to HSE; this will be verified in Sec. 3.4.2) to extrapolate the HSE results to $N \to \infty$. This procedure gives -69.7 meV for Bi donors and -51.3 meV for As donors, in excellent agreement with the experimental values (-70.9 meV for Bi and -53.8 meV for As) [20]. These results show that HSE is able to correct the PBE underestimation of shallow donor binding energies in silicon, achieving remarkable agreement with experiment.

3.4.2 Hyperfine parameter

Results for the hyperfine parameter of bismuth and arsenic shallow donors are shown in Fig. 3.2. The error is expected to scale inversely with the volume of the supercell much as in the case of binding energies (see Sec. 3.4.1), so we again plot our results as a function of $1/N$. The linear trend in hyperfine parameter for PBE calculations starts at even lower cell size of $n \geq 3$ ($N \geq 216$) than the binding energies, allowing extrapolation to the $N \to \infty$ limit. Extrapolating PBE results gives a value of 891 MHz for bismuth

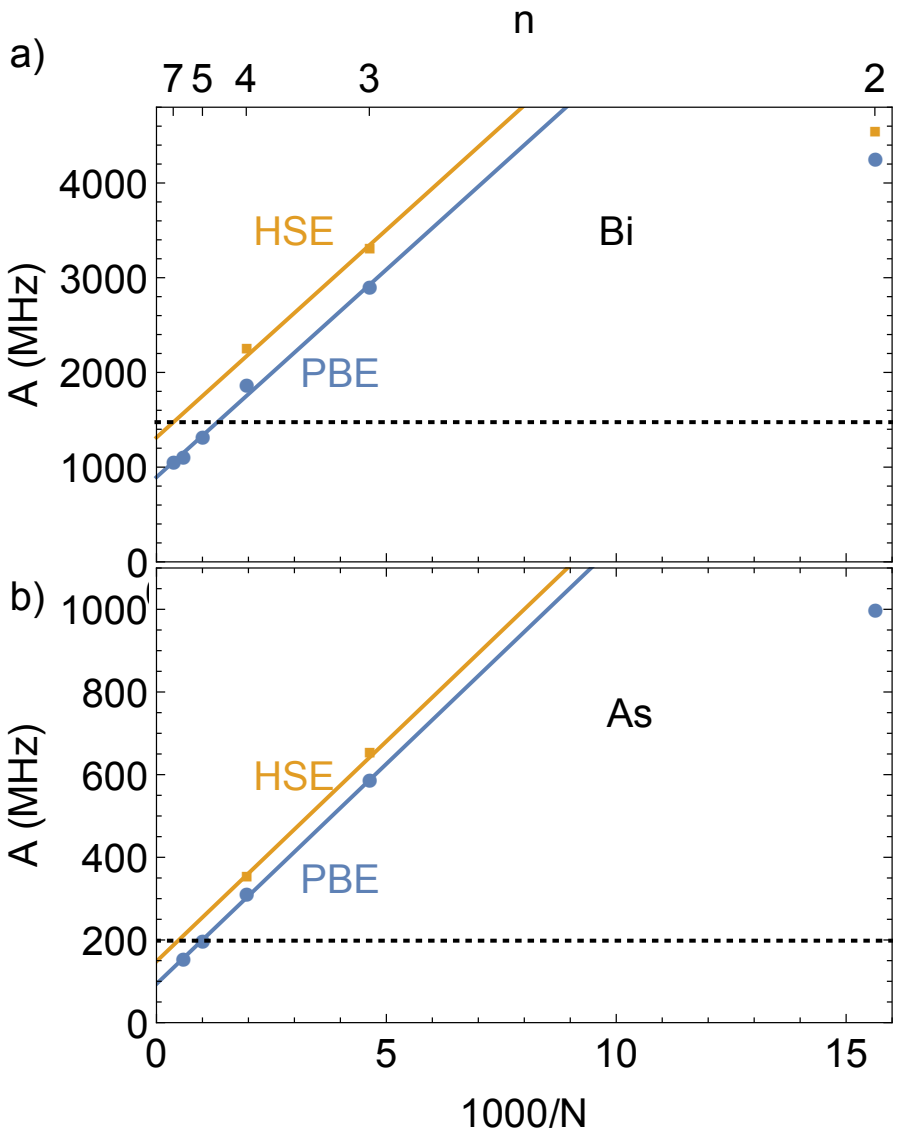

Figure 3.2: a) Calculated isotropic hyperfine parameter for a bismuth donor in silicon as a function of $1/N$, where N is the number of atoms in the supercell. PBE results are in blue, and the line shows a linear fit for $n \geq 3, N \geq 216$: $A = 891 + 4.40 \times 10^5/N$. HSE results are in orange, and the line shows a linear fit for $n \geq 3, N \geq 216$ with the slope fixed to match the PBE fit: $A = 1310 + 4.40 \times 10^5/N$. The dashed black line is the experimental value, $A = 1475$ MHz. b) Calculated isotropic hyperfine parameter for an arsenic donor in silicon as a function of $1/N$, with the same color coding as the top plot. PBE fit: $A = 93.6 + 1.06 \times 10^5/N$. HSE fit with slope fixed by the PBE fit: $A = 148.2 + 1.06 \times 10^5/N$. The experimental value is $A = 198.3$ MHz.

donors, significantly underestimating the experimental result of 1475 MHz [45]. For the arsenic donors, the extrapolated value is 93.6 MHz, compared to an experimental value of 198.3 MHz [20].

This underestimation of the hyperfine parameter is due to PBE overdelocalization, and may be fixed using HSE in a similar way to that employed for the binding energies. HSE results show linear scaling in the same regime as PBE and with the same slope, supporting our assertion that PBE scaling extends to HSE results for binding energies. This procedure gives 1310 MHz for Bi donors and 148.2 MHz for As donors (compared with experimental values of 1475 MHz for Bi [45] and 198.3 MHz for As.[20]), providing a vast improvement over PBE.

3.4.3 Electric field gradients and quadrupole couplings

We have calculated the EFG at the nucleus of the Bi shallow donor in unstrained silicon and find it to be zero to within the accuracy of our calculations; we estimate the error bar to be approximately 1 $\mathrm{V/\AA^2}$, corresponding to a quadrupole interaction strength of approximately 1 MHz. For the unstrained case, the zero value is as expected, since symmetry arguments show that the EFG should vanish [45]. However, the calculated EFGs remain zero (within the error bar) when strain is applied. This runs counter to the hypothesis of Pla *et al.* [45], which assumed a quadrupole interaction on the order of 100 MHz, and thus calls into question the proposed quadrupole mechanism for the splitting observed in the ESR spectrum. These results highlight the need for a different mechanism to explain the observed splitting. In the next section we will explore the shift of the isotropic hyperfine parameter with the hydrostatic component of strain.

3.4.4 Strain

The calculated dependence of the isotropic hyperfine parameter on strain is shown in Fig. 3.3 for a bismuth donor in silicon (using PBE in the $n = 6$, $N = 1728$ supercell). Figure 3.3 (a) shows the data for hydrostatic strain, which are well described by a linear fit up to the highest strains tested (2×10^{-3}), with a coefficient that corresponds to $K = 17.5$ [Eq. (3.3)]. This value is in good agreement with the experimental value $K = 19.1$ [48]. Figure 3.3 (b) shows uniaxial strain. We varied ϵ_{zz} up to 2×10^{-3}, keeping $\epsilon_{xx} = \epsilon_{yy} = 0$. The calculated points are fitted to Eq. (3.3) using the K value obtained from the hydrostatic strain calculations. The quadratic term is found to be $L = -11700$. Using tight binding, Mansir *et al.* [48] obtained $L = -9064$; they also reported a value $L = -9720$ predicted by the valley repopulation model. Deviations from the quadratic behavior are observed for higher strains, consistent with the higher-order repopulation effects.

The linear fit to hydrostatic component of strain [Fig. 3.3 (a)] for $n = 6$, $N = 1728$ may be repeated at different supercell sizes and subjected to similar scaling analysis as binding energies (Sec. 3.4.1) and hyperfine parameters (Sec. 3.4.2). The results of this procedure are shown in Fig. 3.4. K also shows linear scaling with $1/N$, but it begins at a higher N value than observed for the hyperfine parameter itself. Extrapolation to the dilute limit gives a coefficient of $K = 20.2$, in good agreement with the experimental value $K = 19.1$ [48]. We have not attempted an HSE correction, since PBE and HSE results for K are very similar at small N.

The bismuth-silicon bond lengths in the unstrained case are 2.651 Å, compared to 2.367 Å in bulk silicon. When hydrostatic strain is applied, all Bi-Si and Si-Si bond lengths simply scaled by hydrostatic strain to within better than 0.001 Å. Our results clearly show that the isotropic hyperfine parameter depends linearly on the hydrostatic

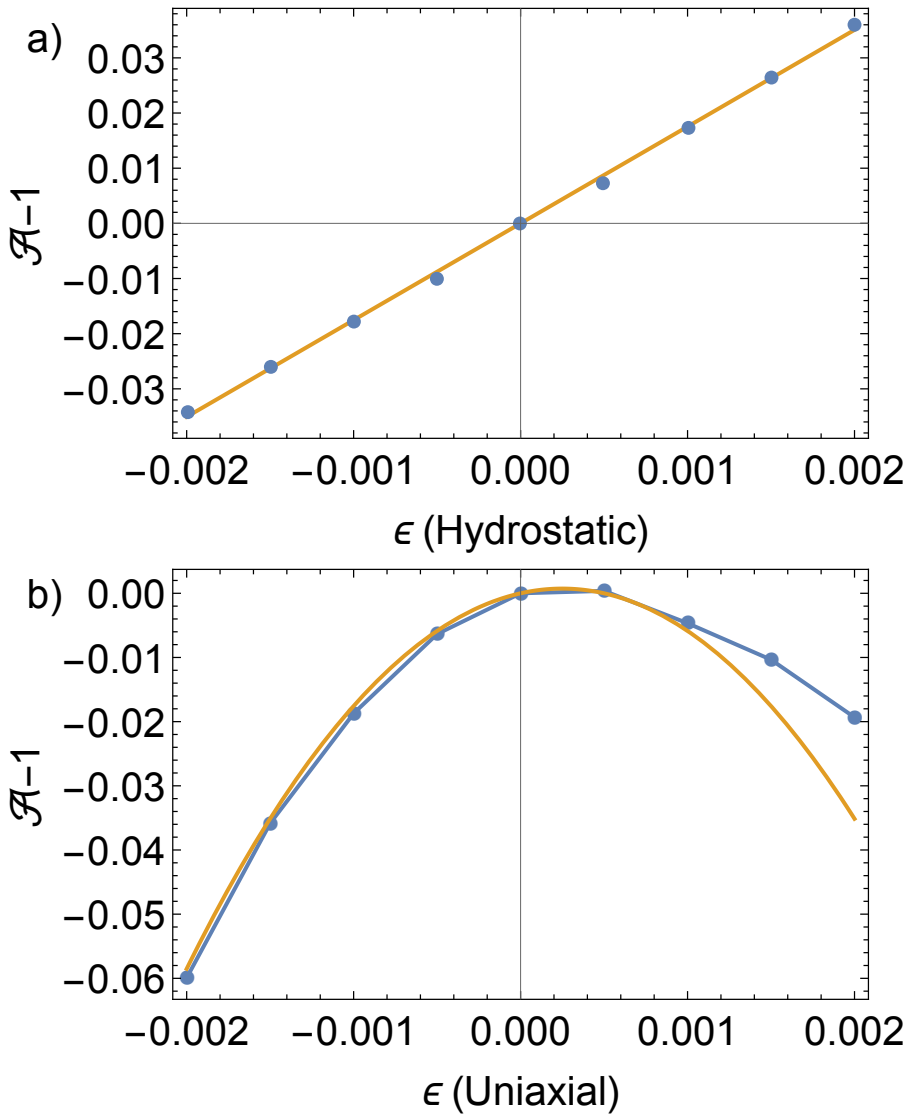

Figure 3.3: a) $A/A_0 - 1$ versus hydrostatic strain for a bismuth donor in silicon in the $n = 6$, $N = 1728$-atom supercell using PBE. A linear fit produces $K = 17.5$ [Eq. (3.3)]. b) $A/A_0 - 1$ versus uniaxial strain for a bismuth donor in silicon. Taking $K = 17.5$ fixed based on the hydrostatic case, a fit to the data up to $\epsilon = 10^{-3}$ using Eq. (3.3) is shown, which gives $L = -11700$.

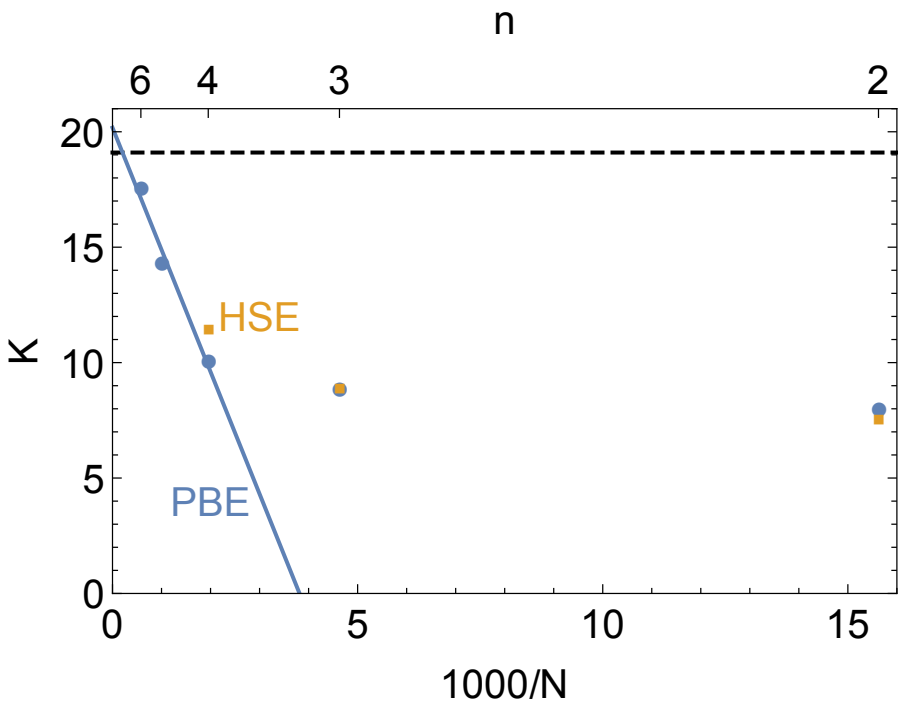

Figure 3.4: Calculated K coefficient [Eq. (3.3)] as a function of supercell size. PBE in blue circles, HSE in orange squares. A fit to PBE data for $N \geq 512$ is shown: $K = 20.2 - 5290/N$. The dashed line shows the experimental value.

component of strain with a coefficient that significantly differs from that predicted by effective mass theory, highlighting the importance of valley-orbit coupling and central-cell corrections.

3.4.5 Irreducible representations

The symmetry and group-theoretic properties of the ground-state wavefunction are key to all of our results. As discussed in the Introduction, the 6-fold degenerate CBM splits into states corresponding to irreducible representations (irreps) of the T_d symmetry group: singlet A_1, doublet E, and triplet T_2 [20, 23]. The A_1 wavefunction (the fully symmetric state) has a peak at the center while the others have nodes. This allows the A_1 state to maximize the Coulomb binding energy, making it the ground state, with an energy that is significantly lowered compared to effective mass theory. This also means that the hyperfine parameter is directly related to the amount of A_1 character in the ground state; as more of the other irreps are mixed in, the hyperfine parameter decreases. In the case of uniaxial strain (Fig. 3.3, second panel), the symmetry is lowered, at the expense of the weight of the fully symmetric A_1 state, and A decreases for both compressive and expansive uniaxial strain.

To demonstrate that our calculations correctly capture these symmetry effects, we project out the portions of the donor wavefunctions which transform according to the various irreps of T_d. We use the projection operator

$$\hat{P}^j = \frac{l_j}{h} \sum_R \chi(R)^j \hat{R}\,, \tag{3.7}$$

where j indexes the various irreps, l_j is the dimension of the irrep, h is the order of the T_d group, R is summed over all the symmetry operations in the group, and $\chi(R)^j$ is the character of the operation in the jth representation [56]. Note that the rotation matrices

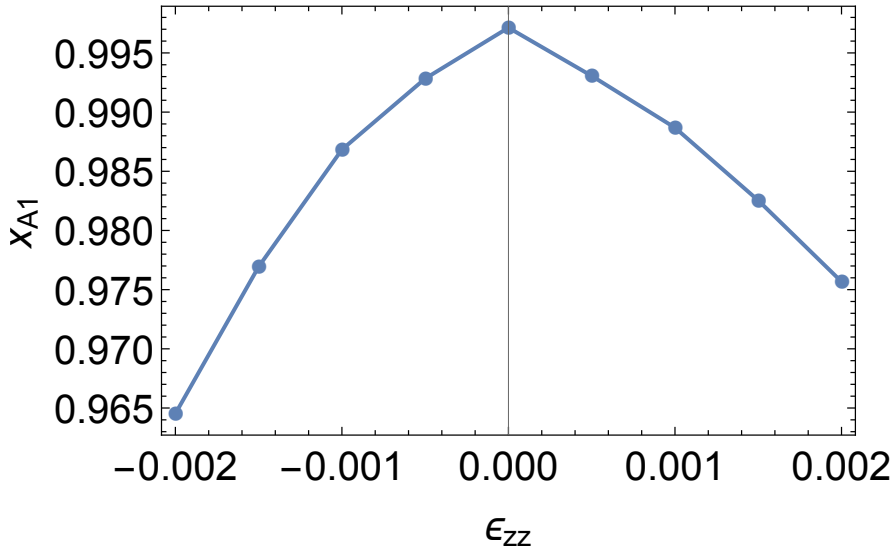

Figure 3.5: Fraction of the spin density which transforms according to the A_1 irreducible representation [Eq. (3.8)], plotted as a function of applied uniaxial strain. At zero strain, ρ transforms under the A_1 representation. As uniaxial strain is applied, the fraction of ρ which transforms under A_1 decreases.

cannot simply be added together; each must be applied separately to the charge density, and the results must be added. Code implementing this projection may be found at `https://bitbucket.org/numenorean7/symmetry_projection`.

With cell volume Ω, we define the fraction of the spin density ρ which transforms under the jth irrep

$$x_j = \frac{1}{\Omega} \int d^3\mathbf{r} \frac{\left|\hat{P}^j \rho\right|}{|\rho|} . \tag{3.8}$$

The x_{A1} values as a function of strain ϵ_{zz} with $\epsilon_{xx} = \epsilon_{yy} = 0$ are shown in Fig. 3.5. At zero strain, ρ transforms almost entirely under the A_1 representation, and as uniaxial strain is applied, the fraction of ρ which transforms under A_1 decreases, following a trend similar to the hyperfine parameter (Fig. 3.3, second panel). Visualizations of the projected spin density are shown in Fig. 3.6.

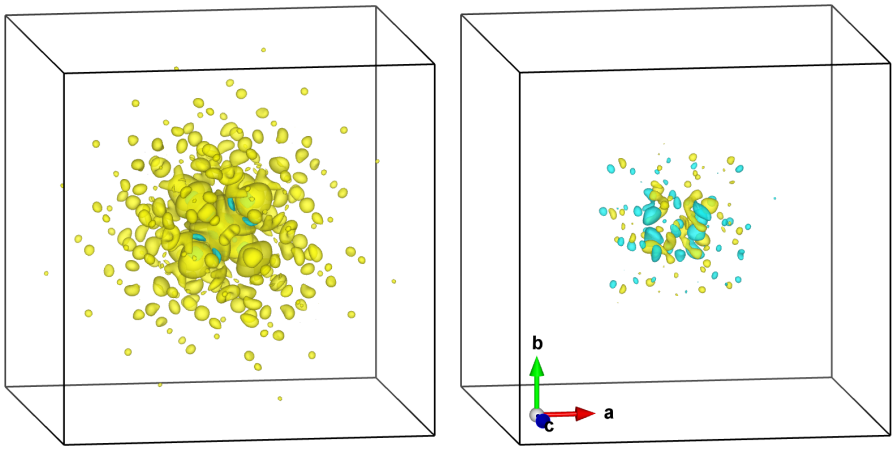

Figure 3.6: Results of projecting ρ onto the A_1 representation for a calculation with $\epsilon_{xx} = 10^{-3}$ uniaxial strain, in a $N = 1728$ ($n = 6$) supercell. Left: The portion of ρ which transforms as A_1. Isosurface value $2.7 \times 10^{-4} e/\text{Å}^3$. Right: The remainder after projection. Isosurface value $5.4 \times 10^{-5} e/\text{Å}^3$.

3.5 Conclusions

The study of shallow impurity wavefunctions has a long history, beginning with Kohn-Luttinger effective mass theory in the 1950s. We have overcome some of the challenges to modeling these wavefunctions from first principles, allowing us to employ DFT calculations which fully include central-cell and valley-orbit effects. This allows us to study the evolution of the hyperfine parameter and quadrupole coupling of shallow donors as a function of strain without the use of empirical fitting parameters.

Our calculations show that the electric field gradients at the site of the nucleus are negligible even when strain is applied. This suggests that the splittings observed by Pla *et al.* [45] do not in fact arise from quadrupole interactions.

Instead, our calculations lend strong support to an alternative mechanism recently explored in Ref. [48], which suggests a large linear dependence of the isotropic hyperfine parameter A on the hydrostatic component of strain. Our calculations find just such a dependence, with a coefficient $K = 20.2$ that is in good agreement with the experimental

value $K = 19.1$. The linear dependence on hydrostatic strain is significantly larger than the dependence predicted by effective mass theory.

Finally, we have calculated accurate hyperfine parameters and binding energies of bismuth and arsenic shallow donors by using PBE, identifying a $1/N$ scaling with supercell size and extrapolating to the $N \to \infty$ limit, and correcting the results for PBE self-interaction error using the HSE hybrid functional. This procedure represents a significant step forward in the *ab intio* simulation of shallow donors in silicon, and we expect it to be generalizable to other shallow impurities in silicon and other materials.

Chapter 4

Conditions for T^2 Resistivity from Electron-Electron Scattering

4.1 Introduction

A resistivity component of the form $\rho = AT^2$ has been observed in a variety of materials. The most well known are metals at low temperature, including transition metals [57, 58, 59] (with $A \sim 10^{-4}$ to $10^{-5}\,\mu\Omega\,\mathrm{cm/K^2}$) and alkali metals [60, 61, 62] (with $A \sim 10^{-6}$ to $10^{-7}\,\mu\Omega\,\mathrm{cm/K^2}$). The mechanism behind this contribution to resistivity has been identified as electron-electron scattering (or Baber scattering [63]). This scattering mechanism is well described by Fermi liquid theory, which predicts $\rho_{\text{el-el}} = AT^2$ of a similar magnitude to that seen in experiments [64, 65, 66]. Unifying features of electron-electron scattering in these materials include a relatively small scattering rate and a low temperature threshold ($\sim$ 20 K for transition metals, a few K for alkali metals) above which other scattering mechanisms (such as electron-phonon) dominate.

More recently, investigations into transport properties of complex oxides have also found a resistivity component $\rho = AT^2$, or a component of electron mobility $\mu = \alpha T^{-2}$.

Examples include $SrTiO_3$ (STO) [67, 68, 69, 70], rare-earth nickelates [71, 72], and cuprates [73, 74]. Discussions of the T^2 behavior (and deviations from it) are often based on the assumption that the T^2 comes from Fermi-liquid electron-electron scattering, much as it does in metals. Though the power law is the same, this mechanism is several orders of magnitude stronger ($A \sim 10^{-1}$ to $10^{-2}\,\mu\Omega\,\mathrm{cm/K^2}$) and has been observed in some cases up to room temperature. Other transport signatures have also clashed with predictions from Fermi liquid theory [70, 75].

In this work, we show that the T^2 exponent of Baber scattering arises only under a certain set of assumptions. These assumptions are fulfilled in metals at low temperature (as we show explicitly for the case of sodium metal), but are not necessarily fulfilled in semiconductors at higher temperature. In the specific case of bulk STO, we find that many of the assumptions do *not* hold, and explicit calculations of this scattering mechanism result in a resistivity that significantly deviates from the T^2 behavior. More generally, this implies that observation of $\rho \propto T^2$ in a given system is not evidence for electron-electron scattering unless the assumptions behind the Baber T^2 hold in that system.

4.2 Theory

4.2.1 Boltzmann transport for electron-electron scattering

We approach the study of this electron-electron scattering using Boltzmann transport theory, following methods derived in Refs. [37, 38]. The methodology is laid out in detail in Sec. 2.9. The resistivity is given by Eq.(2.25), which is reproduced below:

$$\rho_{\text{el-el}} = \mathcal{N}\langle\Phi, P\Phi\rangle \text{ , with } \mathcal{N} = [\langle\Phi, X(E=1)\rangle]^{-2} \text{ ,} \tag{4.1}$$

and where $\langle \Phi, P\Phi \rangle$ is given by Eq.(2.24), also reproduced below:

$$\begin{aligned}\langle \Phi, P\Phi \rangle = & \frac{1}{2k_B T} \frac{1}{(2\pi)^9} \frac{2\pi}{\hbar} \sum_{n,n'} \int d\mathbf{k}_1 d\mathbf{k}_2 d\mathbf{k}_3 d\mathbf{k}_4 \\ & \times \left[\left(\mathbf{v}_{n,\mathbf{k}_1} + \mathbf{v}_{n',\mathbf{k}_2} - \mathbf{v}_{n,\mathbf{k}_3} - \mathbf{v}_{n',\mathbf{k}_4} \right) \cdot \hat{\mathbf{u}} \right]^2 \\ & \times f\left(\varepsilon_{n,\mathbf{k}_1}\right) f\left(\varepsilon_{n',\mathbf{k}_2}\right) \left[1 - f\left(\varepsilon_{n,\mathbf{k}_3}\right)\right] \left[1 - f\left(\varepsilon_{n',\mathbf{k}_4}\right)\right] \\ & \times \left(U^{(\mathrm{eff})}_{\mathbf{k}_1,\mathbf{k}_3} \right)^2 \delta\left(\varepsilon_{n,\mathbf{k}_1} + \varepsilon_{n',\mathbf{k}_2} - \varepsilon_{n,\mathbf{k}_3} - \varepsilon_{n',\mathbf{k}_4}\right) \\ & \times \delta\left(\mathbf{k}_1 + \mathbf{k}_2 - \mathbf{k}_3 - \mathbf{k}_4\right) . \end{aligned} \tag{4.2}$$

These equations are the basis for our discussion of electron-electron scattering.

4.2.2 Derivation of T^2

We now lay out the standard derivation of a T^2 power law from Eq. (4.2), in order to understand the assumptions involved. We begin by separating the $\mathbf{k}$-space integral into an integral over the Fermi surface and an integral in the perpendicular direction. Assuming the chemical potential is constant with temperature (Assumption 1), integration over the Fermi surface will give a result that is independent of temperature. In the direction perpendicular to the Fermi surface, the Fermi function terms and energy and momentum conservation restrict the scattering states to a narrow thermal envelope around the Fermi surface. Assuming the non-Fermi-function terms vary slowly enough over the width of this envelope (Assumption 2), they may be approximated as constants given by their value at the Fermi surface. Ignoring the temperature-independent terms and changing integration variables to energy, we can define the integral I, which contains the temperature dependence of the resistivity:

$$\rho_{\text{el-el}} \propto I = \frac{3}{2\pi^2 k_B^3 T} \int_0^\infty d\varepsilon_1\, d\varepsilon_2\, d\varepsilon_3\, f(\varepsilon_1)\, f(\varepsilon_2) \times [1 - f(\varepsilon_3)]\, [1 - f(\varepsilon_1 + \varepsilon_2 - \varepsilon_3)] \tag{4.3}$$

We extract the dimensionful quantities by changing integration variables again to $x_i = (\varepsilon_i - \mu)/k_B T$ and assuming the lower bound on x_i integration can be taken to $-\infty$ (Assumption 3):

$$I = \frac{3T^2}{2\pi^2} \int_{-\infty}^\infty dx_1\, dx_2\, dx_3\, (e^{x_1} + 1)^{-1} (e^{x_2} + 1)^{-1} \times \left[1 - (e^{x_3} + 1)^{-1}\right] \left[1 - (e^{x_1 + x_2 - x_3} + 1)^{-1}\right] \tag{4.4}$$

The integral is a dimensionless constant, so $\rho_{\text{el-el}} \propto T^2$.

4.3 Assumptions

As highlighted during the course of the derivation, this result depends on three key assumptions. We will explore each of the assumptions and determine whether they are satisfied in our case studies, Na metal and STO. We will investigate the impact of each assumption on the final result by calculating ρ as a function of T employing the assumption and comparing to a numerical calculation with the assumption removed. Numerical integration is carried out with Divonne, a Monte Carlo integration algorithm which uses stratified sampling for variance reduction, as implemented in the CUBA package [41].

4.3.1 Assumption 1

As temperature changes, the chemical potential μ of the electrons is constant and equal to its zero-temperature value. While this is a very good approximation in metals

at low temperature, it may not hold in semiconductors at intermediate temperature. In many cases (including degenerately doped semiconductors), the quantity which actually remains constant with temperature is the electron density n. The chemical potential μ is determined by the equation

$$n = \sum_i \int d\varepsilon \; D_i(\varepsilon) f(\varepsilon) \,, \tag{4.5}$$

where D_i is the density of states of band i, and μ and T are implicit in f [Eq. (2.20)]. With Assumption 1 in place, μ is set to its zero-temperature value, which we calculate analytically. When this assumption is relaxed, the integral in Eq. (4.5) is calculated numerically, and μ is recalculated at any given temperature to keep n fixed. When $\mu \gg k_B T$, smearing of f due to increased T does not have a strong effect on Eq. (4.5), so μ has negligible temperature dependence. However, when $\mu \sim k_B T$, the chemical potential does have a significant temperature dependence, as shown in Fig. 4.1.

4.3.2 Assumption 2

The integrand in Eq. (4.2) is slowly varying compared to the Fermi functions over the width of the thermal envelope. When Assumption 2 is in place, the non-Fermi-function terms in the integrand are taken to be constant for a given direction in k-space, equal to their value at the Fermi surface. This reduces the radial part of the integral to Eq. (4.3). When Assumption 2 is relaxed, the radial dependence of the integrand is included explicitly. This assumption is valid at temperatures that are small compared to the scale over which the non-Fermi-function terms vary. This scale is difficult to predict *a priori*, so we will assess the validity of this assumption on a case-by-case basis.

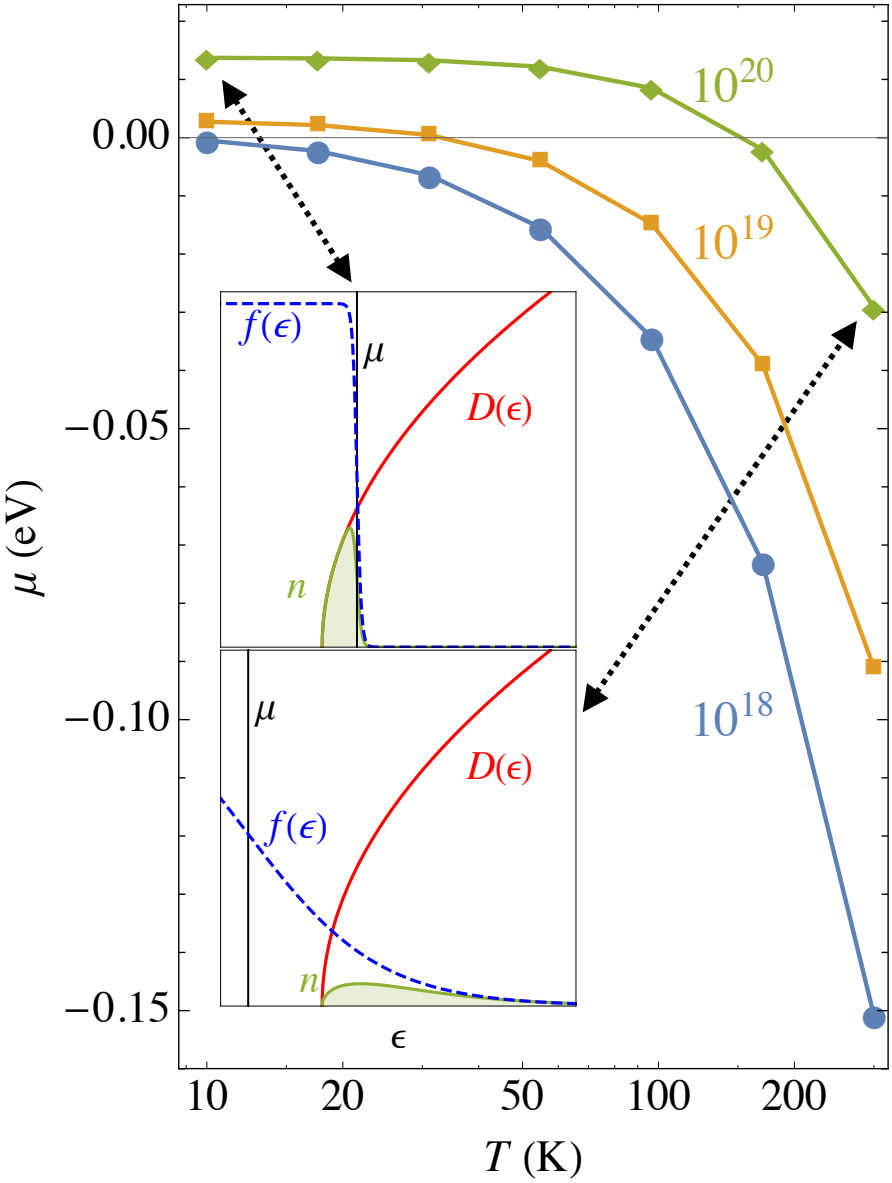

Figure 4.1: Chemical potential as a function of temperature in strontium titanate for three different fixed electron concentrations, expressed in cm^{-3}. Inset: illustration of Eq. (4.5) applied to find μ for $n = 10^{20}$ cm^{-3} at $T = 10$ K and $T = 300$ K. These results were calculated using our anisotropic parabolic fit to the conduction band of $SrTiO_3$ [Eq. (4.7)].

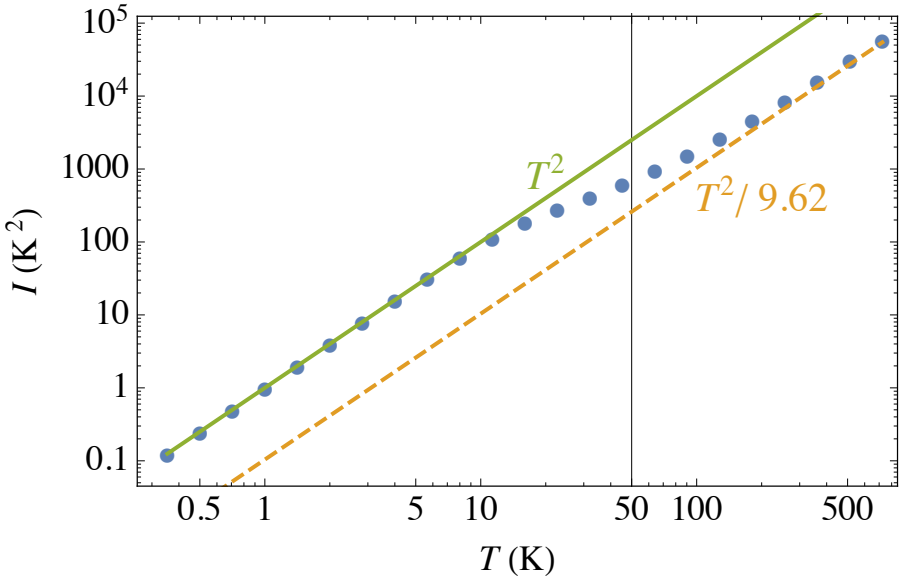

Figure 4.2: Log-log plot of I [Eq. (4.4)] as a function of temperature for fixed chemical potential $\mu/k_B = 50$ K (indicated by the solid vertical line). I shows a clear change from T^2 to $T^2/9.62$.

4.3.3 Assumption 3

The lower limit of integration in Eq. (4.4) can be taken to $-\infty$. In fact, since the lower limit in Eq. (4.1) is set by the conduction-band minimum ($\varepsilon = 0$), the lower limit of integral I should be $-\mu/k_BT$. If $\mu \gg k_BT$, Assumption 3 is valid and $I = T^2$. However, if $\mu \ll k_BT$, Eq. (4.4) should instead run from 0 to ∞, and $I = T^2(1/4 - 3(\ln 2)^2/\pi^2) \approx T^2/9.62$. These different prefactors imply that an intermediate regime ($\mu \sim k_BT$) must exist, in which $I \not\propto T^2$. This becomes obvious when evaluating I versus T numerically, as shown in Fig. 4.2. A similar approximation is also discussed in Ref. [76].

4.4 Sodium

We now apply this methodology, starting with the test case of sodium metal. The sodium band structure was modeled by fitting a parabolic dispersion relation to a density functional theory calculation (as implemented in the Vienna *Ab initio* Simulation Package (VASP) [11], employing the Perdew, Burke and Ernzerhof [5] functional). We find that a parabolic effective mass of $m = 1.06\, m_e$ fits the first-principles result with an accuracy better than 0.05 eV. Since sodium has a single parabolic band, momentum relaxation comes from Umklapp scattering. Electrons interact through a screened Coulomb potential

$$U_{\mathbf{q}}^{(\text{eff})} = \frac{4\pi e^2}{q^2 + \kappa^2}\,, \tag{4.6}$$

where $\mathbf{q} = \mathbf{k} - \mathbf{k}'$ and $\kappa^2 = 4\pi e^2 \frac{\partial n}{\partial \mu}$ is the Lindhard screening length. The zero-temperature chemical potential is $\mu = 1.96$ eV. This guarantees $\mu \gg k_B T$, so we expect the chemical potential to stay fairly constant with temperature (Assumption 1), and we expect to be in the regime where $I = T^2$ (Assumption 3). Additionally, since the scattering mechanism is usually observed at very low T, the thermal envelope is quite narrow, so we would expect Assumption 2 to hold as well. Our numerical results confirm these expectations (Fig. 4.3). All the assumptions hold well in sodium, so $\rho_{\text{el-el}} \propto T^2$.

It is worth noting that the prefactor $A = 1.4 \times 10^{-5}\, \mu\Omega\, \text{cm/K}^2$ is larger than that observed experimentally ($A = 1.7 - 2.2 \times 10^{-6}\, \mu\Omega\, \text{cm/K}^2$ [60]). A careful inclusion of phonon-mediated electron-electron scattering could bring the calculated value closer to experiment [77]. This mechanism will not invalidate the assumptions or change the T^2 power law, so we do not discuss it further here.

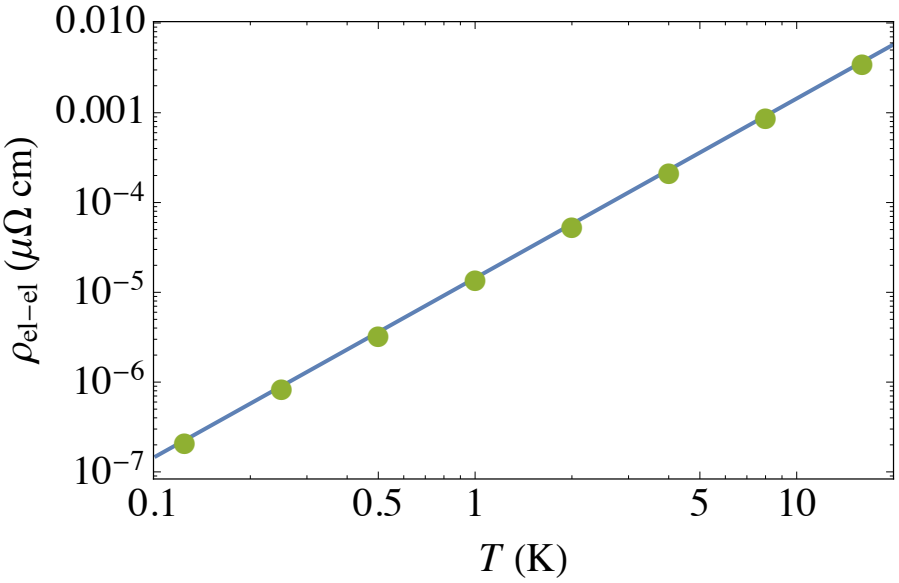

Figure 4.3: Resistivity due to electron-electron scattering versus temperature for metallic sodium. The solid blue line was calculated using all the assumptions while the green data points were calculated without any assumptions. The assumptions hold in this case, so the two computations agree.

4.5 Strontium titanate

We now turn to electron-electron scattering in doped STO. We consider doping levels and temperatures that correspond to experimental conditions over which a T^2 dependence of the carrier mobility has been reported [68, 38, 69]. STO has a low critical density for degenerate doping [78], so we assume that all the electron donors remain ionized as a function of temperature, leading to a constant carrier density. We also assume the cubic structure and neglect spin-orbit coupling. Away from the conduction-band minimum at the Γ point, the bands split into two "light" bands (mass m_π) and one "heavy" band (mass m_δ) with lobes along the Cartesian directions. This allows momentum relaxation through scattering between bands. As discussed in Sec. 2.9.2, we model the dispersion

relation as an anisotropic parabola:

$$\varepsilon_i = \frac{\hbar^2 k_x^2}{2m_{ix}} + \frac{\hbar^2 k_y^2}{2m_{iy}} + \frac{\hbar^2 k_z^2}{2m_{iz}}\,, \tag{4.7}$$

where i indexes the three conduction bands, $m_{1x} = m_{2y} = m_{3z} = m_\delta$, and the other masses are m_π. STO band masses of $m_\pi = 1.16 m_e$ and $m_\delta = 15.31 m_e$ were fit to a first-principles band structure (using VASP with the Heyd, Scuseria, and Ernzerhof [9, 10] functional). This fit produced an accuracy better than 8 meV in the region of interest. The effective electron-electron interaction as discussed in Sec. 2.9.1 is

$$U_{\mathbf{q}}^{(\mathrm{eff})} = \frac{4\pi e^2}{\varepsilon_\infty (q^2+\kappa^2)} - \sum_\lambda \frac{2\left|V_{\mathbf{q},\lambda}\right|^2}{\hbar\omega_\lambda (q^2+\kappa^2)^2} - \frac{2\left|V_{\mathbf{q}}^{(ac)}\right|^2}{\hbar\omega_{\mathbf{q}}^{(ac)}}\,. \tag{4.8}$$

The three terms represent screened Coulomb interaction, optical-phonon-mediated scattering, and acoustic-phonon-mediated scattering. ε_∞ is the high-frequency dielectric constant, κ^2 is the Lindhard screening length defined above, and $V_{\mathbf{q},\lambda}$ is the Fröhlich interaction with optical phonons [79]. The acoustic potential is given by

$$V_{\mathbf{q}}^{(ac)} = \sqrt{4\pi\alpha_{ac}}\frac{\hbar^2}{m_D} q^{1/2} \quad \text{with} \quad \alpha_{ac} = \frac{E_d^2 m_D^2}{8\pi n \hbar^3 v}\,, \tag{4.9}$$

where $\omega_{\mathbf{q}} = vq$ is the acoustic phonon frequency, $n = 5.11\,\mathrm{g\,cm^{-3}}$ is the density of STO, E_d is the deformation potential, $m_D = (m_\pi^2 m_\delta)^{1/3}$ is the density-of-states mass, and $v = 8.1 \times 10^3\,\mathrm{m/s}$ is the speed of sound in STO. Optical phonon frequencies were taken from the calculations in Ref. [80], and the deformation potential for the conduction band was taken to be -4.0 eV as calculated in Ref. [81].

With all Assumptions in place, $\rho_{\text{el-el}} \propto T^2$, as shown in Fig. 4.4. However, none of these Assumptions actually hold in STO, due to the significant change of the chemical

potential with temperature and its position close to the band edge, as illustrated in Fig. 4.1. The full result, obtained without any assumptions, does not follow a T^2 power law (Fig. 4.4). The deviation is particularly pronounced for lower doping (10^{18} cm^{-3}). The temperature dependence is closer to T^2 for higher doping (10^{20} cm^{-3}) and lower temperature ($T < 30$ K) because the chemical potential is higher and changes less with temperature in this regime (as shown in Fig. 4.1), so the Assumptions are closer to being satisfied.

It is worthwhile to discuss our results in the context of earlier work by Klimin *et al.* [38]. While we use the same expression for $\rho_{\text{el-el}}$, our values for the parameters are different and thus we obtain a different scattering rate. Our masses give a better fit to the first-principles band structure of STO, and our deformation potential is calculated instead of being used as a fitting parameter. This affects the relative contributions of the various scattering mechanisms: while we find that Coulomb scattering is dominant, Klimin *et al.* found a competition between Coulomb and acoustic-phonon-mediated scattering due to their much larger deformation potential (23.3 eV). However, their $\rho_{\text{el-el}} \propto T^2$ dependence is a result of employing the Assumptions, so these quantitative differences do not impact our main conclusion. Tests employing the assumptions and parameters used by Klimin *et al.* [38] reproduce their results, and if we use their parameters but do not make the Assumptions, no T^2 dependence is found.

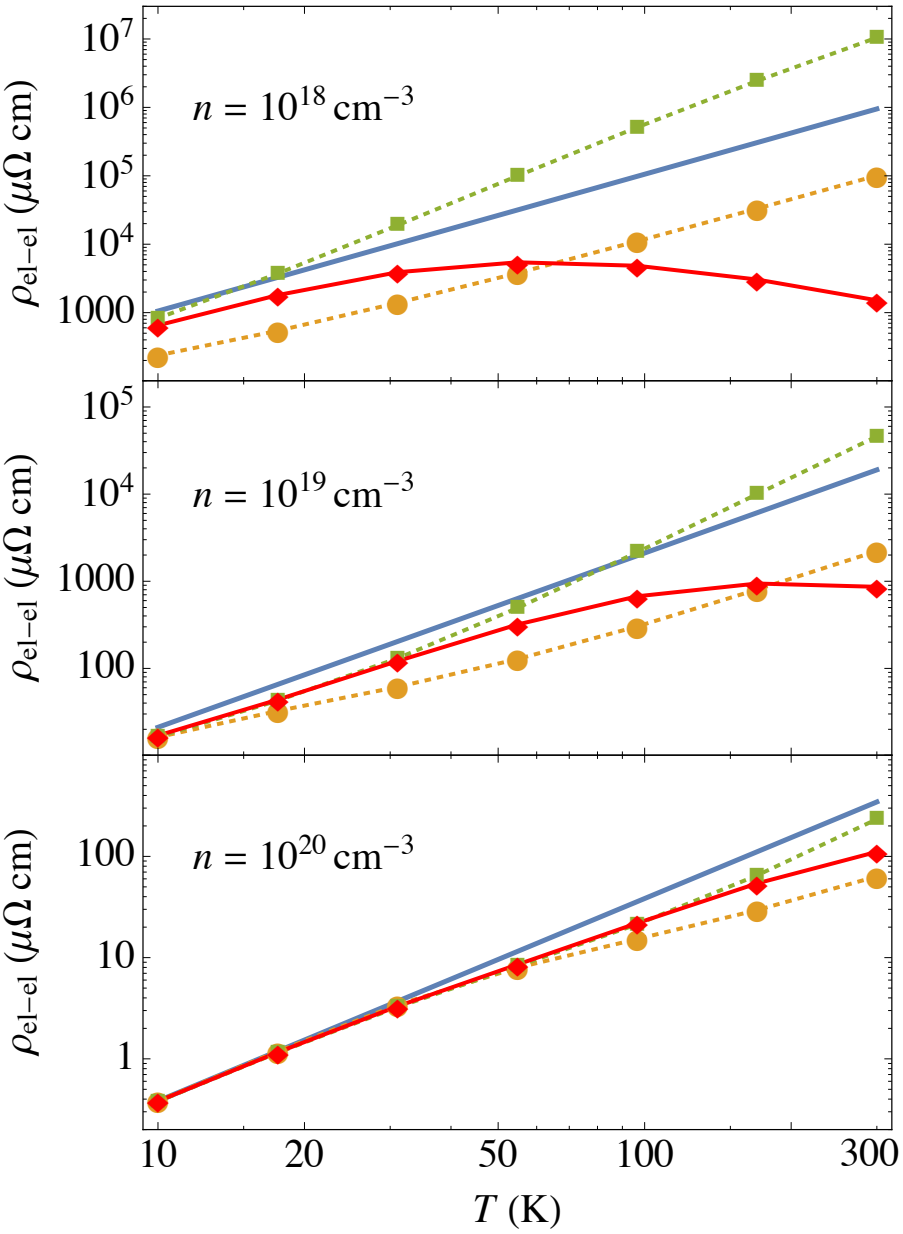

Figure 4.4: Log-log plots of $\rho_{\text{el-el}}$ versus T in STO, with zero-temperature carrier densities as indicated in the panels. Solid blue lines are the pure T^2 law, obtained using all three Assumptions. Orange circles are calculated by computing I [Eq. (4.4)] numerically (i.e., by removing Assumption 3). Green squares show data for which the radial variation of the non-Fermi-function terms is also included (removing Assumptions 2 and 3). Red diamonds show data in which the chemical potential is also allowed to move with temperature to keep the carrier density fixed; all the Assumptions have been removed, so this represents our final results for the electron-electron resistivity.

4.6 Conclusions

When the Assumptions listed here are satisfied (as in sodium metal or STO at high doping and low temperature), electron-electron scattering gives rise to a T^2 power law in the resistivity. When the Assumptions are not satisfied, there is no reason to believe the power law will still hold, and numerical calculations in the case of STO show that in fact the temperature dependence is far from T^2. This has significant implications for the interpretation of measured temperature dependences of transport properties. The common practice of interpreting a T^2 power law as a signature of electron-electron scattering is only supported by theory if the Assumptions are satisfied in the regime over which the power law is observed. If the Assumptions are not satisfied, there is no basis for such a conclusion. This is particularly salient for systems (such as lightly- and moderately-doped semiconductors) in which the chemical potential of the electrons may be close to a band edge, since the Assumptions are likely to be invalid in these systems. In conclusion, T^2 resistivity should not be taken as evidence of Fermi-liquid electron-electron scattering unless the validity of the Assumptions can be established, and caution must always be used when attempting to identify the physical mechanism behind an observed T^2 power law.

Chapter 5

Electron Doping in $Sr_3Ir_2O_7$: Metal-Insulator Transition and Collapse of Magnetic Order

5.1 Introduction

Materials with strong electron correlations and/or strong spin-orbit coupling host many unconventional electronic phases, with many exciting applications such as superconducting circuits for quantum computation or a host of other novel device types. In the Ruddlesden-Popper iridates ($Sr_{n+1}Ir_nO_{3n+1}$), the correlation energy U is comparable in magnitude to the spin-orbit coupling energy λ. This gives rise to an unusual variation on typical Mott insulating behavior in which a combination of U and λ opens a charge gap [82, 83, 84]. Iridium in these compounds is in the 4+ oxidation state with the t_{2g} states occupied with 5 electrons; however in both the $n = 2$ case ($Sr_3Ir_2O_7$, or Sr-327) and the $n = 1$ case (Sr_2IrO_4, or Sr-214), spin-orbit coupling entangles these states and lifts their orbital degeneracy, resulting in a fully occupied $J_{\text{eff}} = 3/2$ quadruplet and

a half-occupied $J_{\text{eff}} = 1/2$ doublet. This splitting, combined with on-site Coulomb repulsion, opens a Mott-Hubbard gap in the half-occupied doublet, forming an insulating antiferromagnetic (AF) $J_{\text{eff}} = 1/2$ ground state. The spin-orbit-assisted stabilization of a Mott gap amongst $J_{\text{eff}} = 1/2$ electrons renders these materials excellent platforms for the observation of many exotic phenomena including proposals of high-temperature superconductivity [85].

The metallic state realized just beyond the antiferromagnetic insulating $J_{\text{eff}} = 1/2$ Mott state is often an anomalous one. The propensity for these weakly correlated spin-orbit assisted Mott states to host unconventional metallic phases is rapidly being established. Examples include the formation of pseudogapped metals [86, 87, 88] with proposals of incipient superconductivity [89, 90], the formation of spin density wave metals [91] and paramagnetic states with unconventional spin dynamics [92, 93, 94], the emergence of competing electronic order parameters [95, 96, 97, 98], two-dimensional metallic phases [99], and reports of negative electronic compressibility [100]. Understanding the underlying mechanisms driving many of these exotic phase phenomena remains an ongoing challenge.

Of particular interest is the metal-insulator transition (MIT) obtained upon electron doping in Sr-327—a transition recently reported to stabilize a metallic state hosting a charge-density-wave (CDW)-like instability [98]. Through substitution of lanthanum on the strontium site [forming $(Sr_{1-x}La_x)_3Ir_2O_7$], experiments have observed a transition from an AF insulating state into a paramagnetic metallic state near a lanthanum concentration $x = 0.04$ [95]. The mechanism behind this transition and a theoretical model of how it arises remain open questions. Further open questions concern the nature of the correlated metallic state that results across the MIT as well as the origin of the proposed CDW instability and its relation to the coincident structural distortion [98, 101].

In this chapter, we seek to advance the understanding of these questions through the

use of first-principles calculations modeling the response of Sr-327 to electron doping. While previous theoretical works have discussed the band structure [82, 83, 84, 102, 103], crystal structure [92], and magnetic order [104, 105] of the Ruddlesden-Popper iridates, first-principles calculations addressing electron doping directly or calculating the metal-insulator transition are notably absent. We will separate the effects of ionic substitution from electron doping, finding that ionic substitution leads to a steric tendency to contract the lattice, which competes with the electronic tendency to expand the lattice.

In Sec. 5.3.2 we address the effect of La impurities used to introduce electrons in experiments on the lattice of the system, separating the effects of ionic substitution from electron doping. The ionic substitution leads to a steric tendency to contract the lattice, which competes with the electronic tendency to expand the lattice.

We calculate an MIT at an electron concentration corresponding to 4.8% substitution of strontium with lanthanum, consistent with experimental results; however, our calculations do not fully model the correlated metallic state on the high-doping side of the phase transition. We will argue that the experimental observation of a low-temperature structural distortion in the metallic phase necessarily arises from many-body correlation physics active in the metallic regime. Our results provide a step forward in understanding the MIT that occurs in electron-doped Sr-327 and suggest that phase competition from the electronic order parameter observed within the unconventional metallic state of this system is not the primary driver of the MIT.

5.2 Computational methods

Our calculations use the general methodology described in Chapter 2. Spin-orbit coupling is included using the non-collinear spinor method as implemented in VASP. The spin quantization axis is chosen along an in-plane lattice vector; tests show that

results are insensitive to this choice. Correlation effects are taken into account using the DFT+U approach [106] with the Perdew-Burke-Ernzerhof (PBE) functional [5]. The value of the on-site Hubbard U parameter is taken to be $U = 1.6$ eV based on constrained random-phase-approximation calculations from Ref. [105].

Experimental results for lattice parameters of doped samples at 300 K are extracted from Le Bail refinements of laboratory-source x-ray diffraction (XRD) profiles to the structural model in Ref. [92] by our collaborators Zach Porter and Stephen Wilson. They measured lanthanum and calcium substitution levels for the samples using wavelength-dispersive x-ray fluorescence spectroscopy (WDXRF), in addition to energy-dispersive x-ray spectroscopy (EDS) to confirm microscopic uniformity.

The starting structure in the calculations is taken from the 100-K refinement in Ref. [92], and the lattice parameters and ionic positions are fully relaxed in all calculations. The Brillouin zone is sampled using a $4\times4\times1$ Γ-centered grid; only a single **k**-point point is needed in the k_z direction because of the size of the c lattice parameter and because of the quasi-2D nature of the material. To capture the details of the conduction band with sufficient accuracy, the zone is sampled more finely near the conduction-band minimum (CBM). The Voronoi cell of the k point closest to the CBM is sampled with a fine mesh, with density equivalent to a $24 \times 24 \times 1$ grid. Supercells used for studying lanthanum and calcium substitution contain $2 \times 2 \times 1$ unit cells and use a $2 \times 2 \times 1$ Γ-centered k point grid. All calculations use a plane-wave energy cutoff of 500 eV.

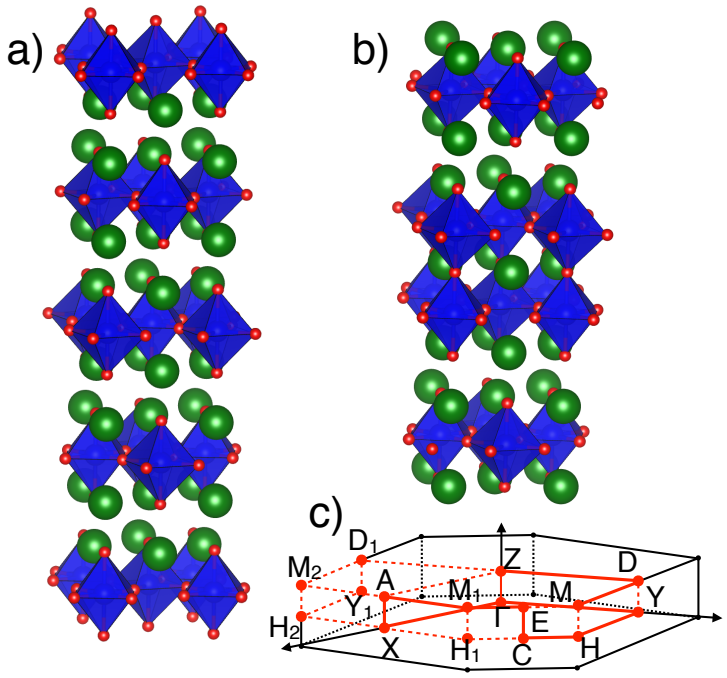

Figure 5.1: Structural visualizations of a) Sr_2IrO_4 and b) $Sr_3Ir_2O_7$. Sr-214 takes a tetragonal structure (space group $I4_1/acd$) [109], and slight deviations from tetragonal make Sr-327 monoclinic (space group $C2/c$) [92]. The first Brillouin zone for Sr-327 is shown in c), with high-symmetry points labeled [110].

5.3 Results and discussion

5.3.1 Electron doping Sr-327

The Ruddlesden-Popper iridates ($n = 1$ and $n = 2$) are formed of n layers of corner-sharing IrO_6 octahedra with Sr in the voids, interspersed with SrO rock-salt layers [83]. Visualizations of the structures are given in Fig. 5.1, and the band structure of Sr-327 is shown in Fig. 5.2. The lattice structure of Sr-327 was recently identified to have a subtly monoclinic C2/c symmetry [92] and the system is known to order antiferromagnetically below 280 K [107, 98] with an ordered moment of $m \approx \frac{1}{3}\ \mu_B$ [108, 102, 95].

Initially, the magnitude of the charge gap of Sr-327 was difficult to experimentally access, with reported values ranging from 85 meV from optical spectroscopy [83, 111]

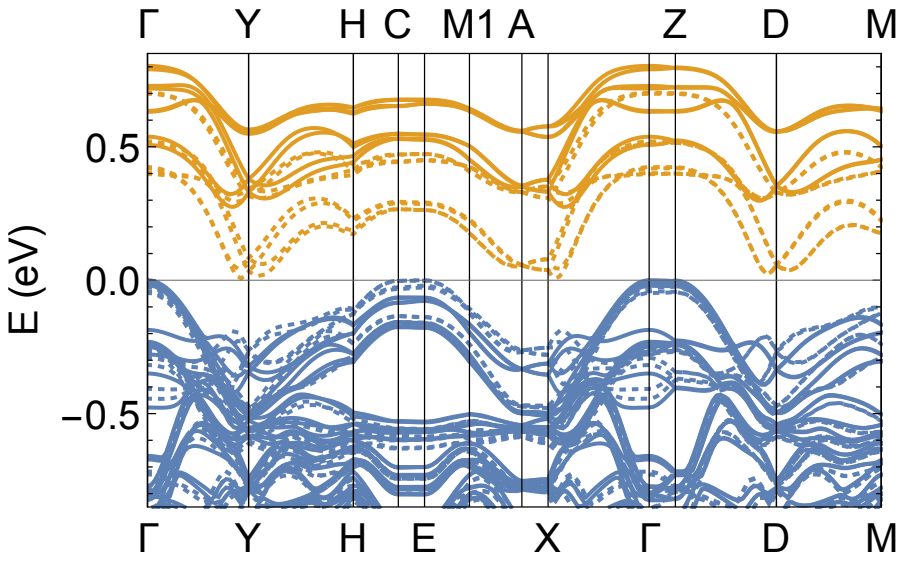

Figure 5.2: DFT+U band structure of Sr-327. Solid lines show the undoped (insulating) case, and dashed lines show the band structure at a doping level above the MIT (at $x = 0.08$). Occupied states (Ir $5d$ states with a mix of $J_{\text{eff}} = 3/2$ and $J_{\text{eff}} = 1/2$) are shown in blue, and unoccupied states (Ir $5d$ states with $J_{\text{eff}} = 1/2$) are shown in orange. The gap in the undoped case is 0.27 eV, indirect between Γ and a point 81% of the way from Γ to X. The smallest direct gap is 0.44 eV, 78% of the way from Γ to X. The gap in the doped case is negligibly small at 7 meV.

to 0.3 eV from angle-resolved photoemission spectroscopy (ARPES) data on doped samples [112, 100]. This suggests the optical spectroscopy (as well as DC transport) measurements may probe a sub-band-gap or phonon-assisted transition [111] rather than the gap itself. In a number of other Mott insulators, defects or small polarons have been identified as sources of sub-band-gap transitions observed in optical spectroscopy [113, 114]. Our calculated value of the band gap, 0.27 eV, agrees well with reported ARPES data and is consistent with the notion of polaronic effects in Sr-327 [115].

In experiments, doping is typically accomplished by substituting some fraction of the strontium with lanthanum, which acts as an electron donor [116, 112, 117, 100, 95, 118, 98]. The effects of cation substitution and electron doping are thus inextricably linked. The bare effect of cation substitution may be approximated by substituting calcium, since it is isoelectronic with strontium but similar in size to lanthanum [95], but this approximation is imperfect. First-principles calculations can explicitly separate the cationic and electronic effects.

To examine pure electron doping, we introduce fractional electrons to the unit cell, with overall charge neutrality ensured by a uniform compensating background. This allows us to capture the physics of electron doping in isolation from the effects of lanthanum impurities that introduce electrons in an experiment. As the number of electrons in the cell increases, there is a slight decreasing trend in the gap and the magnetization. We are able to stabilize two different states: one antiferromagnetic state (aligned out-of-plane) with a larger gap and a second non-magnetic state with a smaller gap. This is consistent with the experimentally observed enhancement of the gap in the antiferromagnetic state [95].

At each doping level the structure with the lower total energy was identified as the ground state. As seen in Fig. 5.3, at low doping the antiferromagnetic insulator is more stable, but the smaller-gap state becomes increasingly favorable as doping increases. At

$x = 0.048$, or 0.144 electrons per formula unit, the non-magnetic state becomes the favored ground state. This is the MIT, at which the gap and magnetization collapse simultaneously. The calculated critical doping value is in good agreement with $x = 0.04$ from experiments, as is the magnitude of the sublattice magnetization and its evolution with doping [95]. Below the transition, the doped electrons in the high-gap state will likely localize, leading to reduced conductivity which will still show an activated (insulating) behavior. This expectation is consistent with resistivity measurements [95]. The collapse of the gap past the transition is consistent with the switch to metallic resistivity in transport experiments [95] as well as the direct measurements of the band gap in doped samples using ARPES [100].

The shape of the conduction and valence bands remain fairly constant with doping; the collapse in the band gap is due primarily to an overall shift of the bands, with changes in band shape playing only a minor role. The CBM remains at the valley 81% of the way from Γ to X for all values of doping ($x = 0.0$ to 0.10). The valence band has two extrema, one at Γ and the other at C. At $x = 0$ the valence-band maximum (VBM) is at Γ; C is lower by 52 meV. As doping increases, the extremum at C rises, until it passes Γ to become the VBM beyond $x = 0.06$. At $x = 0.10$, the highest level of doping we tested, the Γ maximum is lower than the C maximum by 38 meV. See Fig. 5.2.

The character of the bands, nominally iridium d, actually shows significantly hybridization with oxygen. The valence band at Γ consists of 39% oxygen p character and the CBM is 27% O p. These values remain constant to within one percentage point from $x = 0$ to $x = 0.1$. Changes are only slightly larger at the C point, going from 35% O p at $x = 0$ to 31% O p at $x = 0.1$. This strong hybridization is consistent with earlier work [83], explains observed magnetic moments on the oxygen sites [119] and various signatures in optical spectroscopy [111], and plays a role in the dimensionality-induced phase transition across the Ruddlesden-Popper series [103].

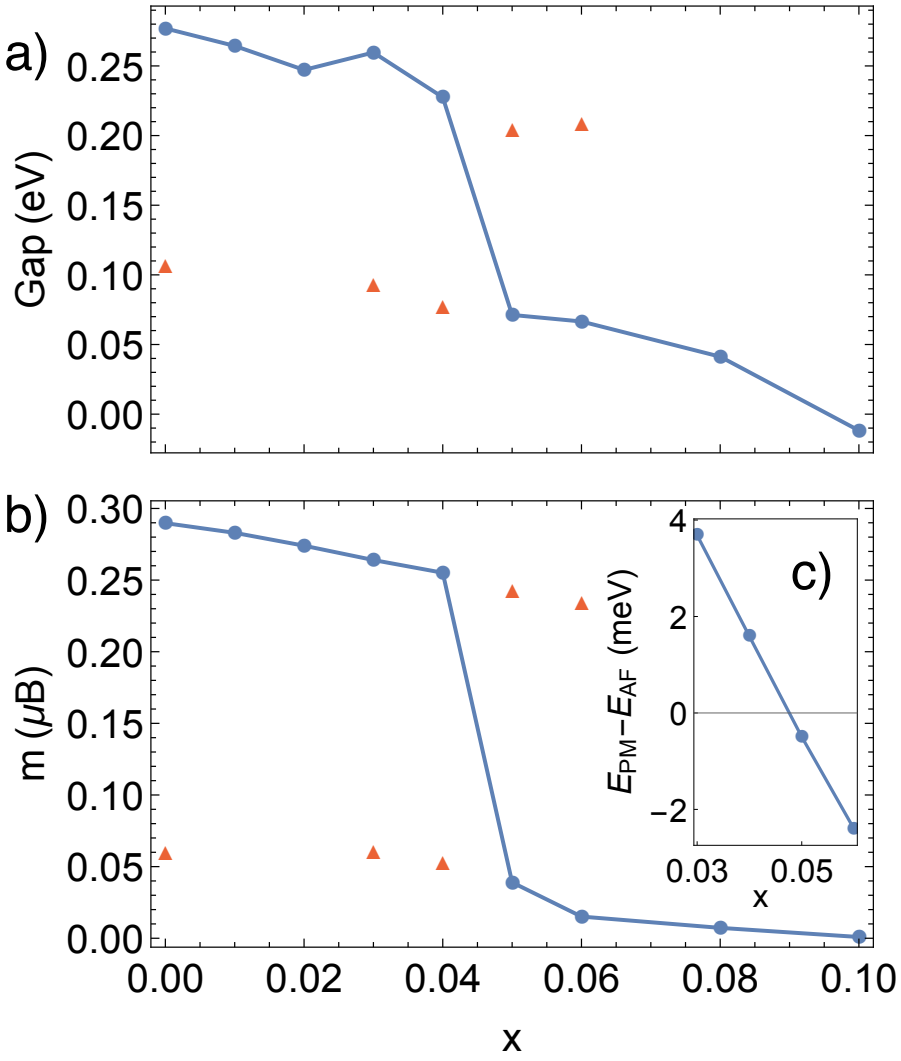

Figure 5.3: a) Indirect band gap and b) out-of-plane magnetization as a function of the number of doping electrons per strontium atom (x). Lowest-energy structures for each doping level are shown in blue circles, connected by lines as a guide to the eye. Calculated metastable structures are shown in red triangles. Inset c): energy difference between the non-magnetic state and antiferromagnetic (AF) state. The crossover at $x = 0.048$ is the critical doping level for the phase transition.

It is significant that the collapse of the charge gap is associated with the collapse in magnetization, even in the metastable states. This is strong evidence that these two phenomena are fundamentally related, and both are captured via the quasi-two-dimensional spin-orbit Mott state as described by DFT+U with spin-orbit coupling. Recent experiments, however, have suggested a CDW instability in the metallic phase of Sr-327, accompanied by a lattice distortion that creates two inequivalent iridium sites with significantly modified octahedral tilting [98]. Though we allow for this symmetry breaking in our calculations, it does not occur, and when the distortion is introduced manually the calculations show it to be unstable. It is significant that, while DFT is able to capture the MIT, the CDW and lattice distortions in the metallic state are not captured. This suggests that these phenomena emerge from many-body effects in the correlated metal distinct from the mechanism behind the transition itself. It is worth noting that the non-magnetic state in our calculations is only a mean-field approximation to the magnetism of the true paramagnetic state; a more thorough treatment of paramagnetic fluctuations requires a supercell approach [120]. More work is needed to explore the metallic state of this material and determine the source of the CDW-like instability.

5.3.2 Impurity substitution and lattice parameters

We now consider the other aspect of doping: ionic substitution. Our results show that the primary effect of cation substitution is steric. Since the ionic radii of lanthanum and calcium are smaller than that of strontium, they are expected to shrink the lattice. We replace one strontium ion with a lanthanum or calcium ion within a supercell that is large enough to minimize the interaction between the defect and its periodic images. The steric effect of lanthanum substitution is isolated from the electronic effect by removing the electron that the donor would donate to the conduction band (i.e., placing the system

in a positive charge state). As in the electron doping study, overall charge neutrality is ensured by a uniform compensating background. Calculations which include electron doping show the same MIT found in bulk cells doped purely with electrons, without any atomic substitution. Figure 5.4 shows the lattice parameter decreasing with increasing incorporation of calcium and positively charged lanthanum, confirming the expectation based on ionic size. Figure 5.4 also shows the pure electronic effect of doping, which is a tendency toward lattice expansion.

The effect of electron doping on the lattice is well known in semiconductors and referred to as a "deformation potential" effect. Deformation potentials describe the shift of the bands as a function of strain, and when the conduction band is occupied with electrons, the energy of the system can be lowered by a deformation that lowers the energy of the conduction-band minimum. This creates a driving force for the expansion or contraction of the lattice, depending on the sign of the deformation potential [121]. This theory has been successfully applied to other complex oxides [81], and we expect that it explains the effect of electron doping on the lattice in Sr-327. When both the electronic and ionic effects are applied [through a supercell containing both the lanthanum donor(s) and the associated free electron(s)], the electronic effect largely cancels out the steric effect.

Figure 5.4(b) includes a comparison with experiment. Lanthanum doping results are taken from Refs. [95, 101], calcium doping results were obtained using the methodology outlined above. Our calculated results are consistent with measurements of the fractional volume change for both lanthanum- and calcium-substituted samples [Fig. 5.4(b)]. For lanthanum, a very small effect on volume is observed; for calcium, the experimental results by our collaborators Zach Porter and Stephen Wilson show a sizeable decrease in volume with increasing calcium doping, again consistent with our calculations.

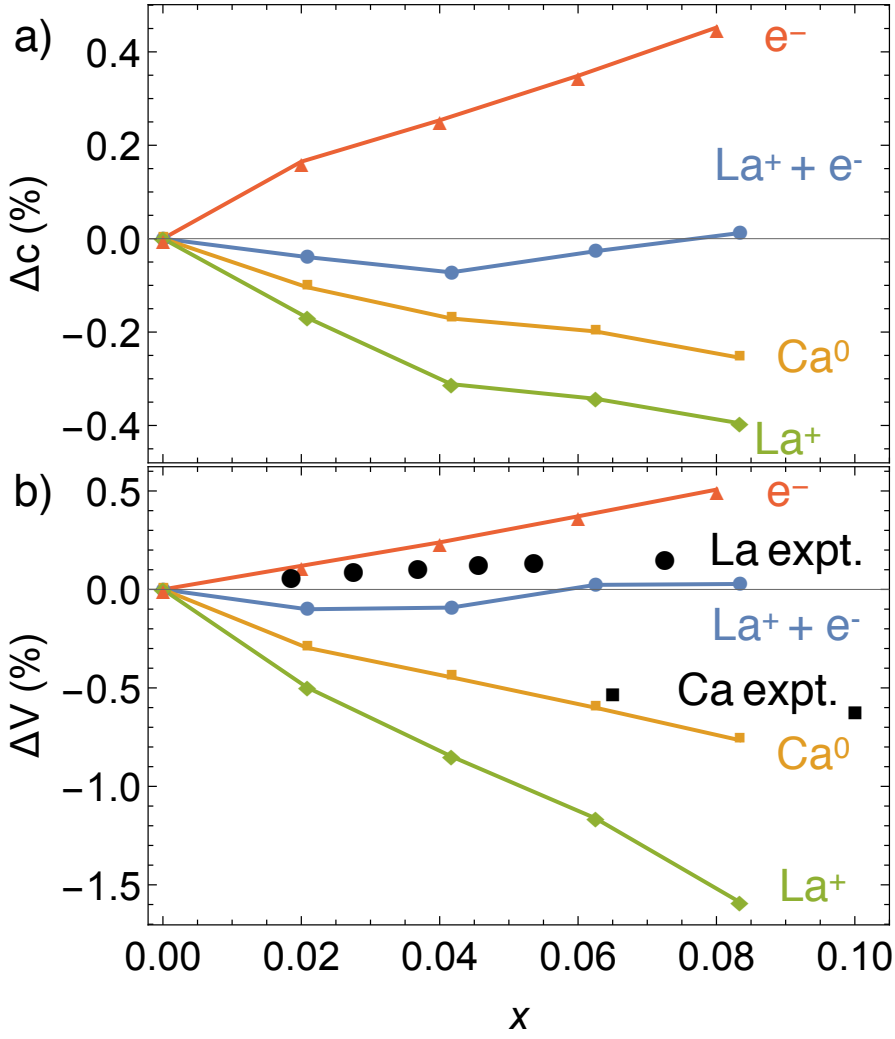

Figure 5.4: Percentage change of a) out-of-plane lattice parameter c and b) cell volume as a function of doping. Note the tendency of the lattice to contract on calcium doping (or incorporation of La^+), driven by steric effects, and the tendency toward lattice expansion on electron doping, driven by the deformation-potential effect. Lines connecting data points are a guide to the eye. Electron doping (without ionic substitution) is shown in red triangles, La^+ (lanthanum substitution without the donated electron) is shown in green diamonds, and $La^+ + e^-$ (lanthanum substitution including the donated electron) is shown in blue circles. Experimental data for lanthanum doping [95, 101] are shown as solid black circles. For comparison, calculated results for calcium substitution are shown as orange squares, and experimental results by our collaborators Zach Porter and Stephen Wilson are shown as black squares.

5.4 Conclusion

In summary, our calculations show a MIT and the concomitant collapse of magnetization in $(Sr_{1-x}La_x)_3Ir_2O_7$ at $x = 0.048$, in good agreement with experimental results. This transition comes about purely through the effect of electronic doping; ionic effects are primarily steric. The tendency toward lattice contraction driven by ionic size is counteracted by the tendency of the electrons to expand the lattice through the deformation potential of the conduction bands. Our calculations do not show the CDW instability nor lattice distortions observed in the paramagnetic state of Sr-327. This suggests that the CDW and accompanying lattice distortion in the metallic state arise from many-body effects not present in our calculations, whereas the spin-orbit-assisted MIT and the collapse of magnetization both arise from physics that is well-described by DFT+U with spin orbit coupling.

Chapter 6

Small Polarons and Point Defects in Barium Cerate

6.1 Introduction

Hydrogen is known to readily incorporate in many oxides with the perovskite crystal structure, such as barium cerate [122] (Fig. 6.1(a)). $BaCeO_3$ has been explored for use in numerous applications, including steam electrolysis for hydrogen production, hydrogen gas sensors, hydrogen pumps and membranes, and solid oxide fuel cells for operation at intermediate temperatures [123]. Historically, *ab initio* techniques based on density functional theory (DFT) have encountered obstacles when applied to cerium-containing compounds. This is due in large part to the important role cerium $4f$ electrons play in the physics of these materials. Localization and correlation effects are strong for bands of f electrons, and exchange-correlation functionals such as the local density approximation (LDA) or generalized gradient approximation (GGA) fall short in capturing the physics of f states. Hybrid functionals, on the other hand, combine exact Hartree-Fock exchange with GGA, and have been shown to improve the description of strongly localized car-

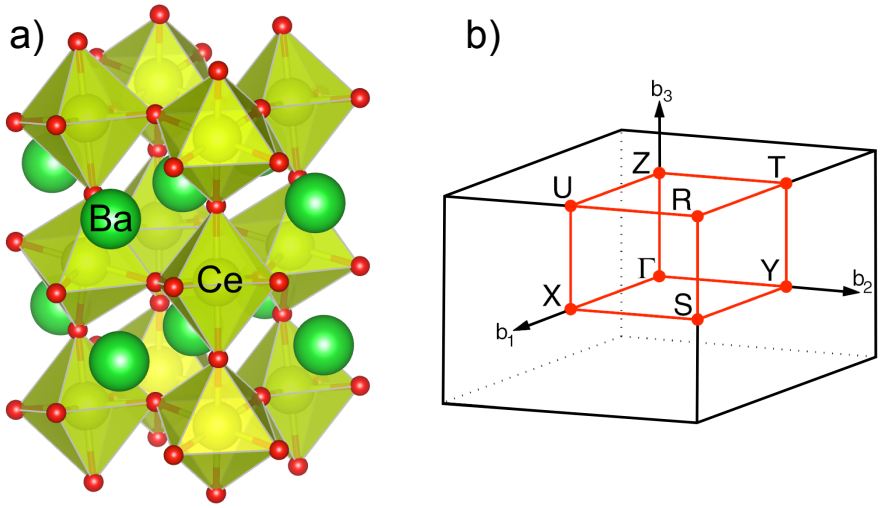

Figure 6.1: a) Visualization of the orthorhombic perovskite structure of barium cerate. Cerium ions are octahedrally coordinated by oxygen, with barium ions interspersed. (Barium ions are green, cerium-centered octahedra are yellow, and oxygen ions are red.) b) Brillouin zone of the orthorhombic lattice, illustrating the conventional path along high-symmetry directions [110].

riers [124, 125, 126, 127]. They have also proven accurate in the description of defects in a wide variety of semiconductor systems, correcting the band-gap problem of LDA and GGA [128]. These advantages make DFT with hybrid functionals very well suited for the study of barium cerate. We calculate formation energies of defects and binding energies of defect complexes, which are essential for describing hydrogen motion through the material.

Hydrogen incorporation into $BaCeO_3$ often proceeds through the reaction [123]

$$H_2O + V_O^{2+} \leftrightarrow O_O + 2H_i^+ \tag{6.1}$$

where V_O^{2+} indicates an oxygen vacancy acting as a double donor, O_O indicates an occupied oxygen site, and H_i^+ indicates a proton occupying an interstitial position in the lattice. A thorough understanding of ionic conduction in barium cerate thus requires an

investigation of interstitial hydrogen and oxygen vacancies, as well as of their interaction, including the possible formation of a defect complex.

$BaCeO_3$ is often doped with elements such as yttrium ($BaCe_{1-x}Y_xO_3$) or neodymium ($BaCe_{1-x}Nd_xO_3$). This process increases the chemical stability of the material and enhances oxygen vacancy concentrations, while still maintaining good ionic conduction. We therefore also investigate substitutional yttrium, Y_{Ce}, as well as its complexes. Since yttrium has one fewer valence electron than cerium, yttrium on the cerium site is expected to act as a single acceptor. In its negative charge state, it will strongly interact with positively charged defects such as interstitial hydrogen or oxygen vacancies.

6.2 Computational methods

Our calculations use the general methodology described in Chapter 2. All calculations used the HSE hybrid functional with standard parameters (HSE06). The chosen pseudopotential for cerium included 46 electrons in the core ([Kr] $4d^{10}$), leaving 12 valence electrons ($5s^25p^64f5d6s^2$) for the PAW calculation. Lattice parameters and band structure were calculated for a 20-atom conventional cell using a $4\times4\times4$ Monkhorst-Pack grid in reciprocal space [129]. Defect and polaron calculations were performed in a 160-atom supercell using a single point in reciprocal space, $k = (0.25, 0.25, 0.25)$. All calculations used a plane-wave energy cutoff of 400 eV. We verified precision by performing tests with 500 eV cutoffs and a $2\times2\times2$ k-point mesh. The tests gave discrepancies of less than 2% for formation energies, lattice parameters, and the band gap, indicating that our results are converged with respect to both k-point density and plane-wave cutoff.

Table 6.1: Structural parameters of $BaCeO_3$ as calculated using HSE, compared with experimental values [130]. The angles measure the degree of octahedral tilting: $\angle_1$ is the in-plane ($\perp z$) Ce-O-Ce angle for cerium atoms separated along the z direction, and $\angle_2$ is the out-of-plane ($\parallel z$) Ce-O-Ce angle.

	Theory	Exp
a (Å)	6.233	6.237
b (Å)	6.223	6.218
c (Å)	8.782	8.780
$\angle_1$	159.4°	158.8°
$\angle_2$	156.6°	156.1°

6.3 Results

6.3.1 Structural Parameters

The low-temperature phase of barium cerate is an orthorhombic perovskite with moderate octahedral tilting and very similar a and b lattice parameters [130]. Table 6.1 shows the structural parameters of pure $BaCeO_3$ as calculated using HSE, and Fig. 6.1 shows a visualization of the structure. The calculated structural parameters are in good agreement with experiment.

6.3.2 Band Structure

Fig. 6.2 shows the calculated band structure of barium cerate. The band gap of 4.17 eV is in very good agreement with the experimental value of 4.1 eV obtained from optical absorption spectroscopy [132]. Since HSE has been shown to correctly describe the cerium-containing oxides CeO_2 and Ce_2O_3 [133, 134], including the $4f$ conduction-band states, we expect $BaCeO_3$ to also be well described by HSE. The valence band is primarily composed of O $2p$ states, and is separated from the conduction band by a direct gap at Γ. There is a further gap of 0.54 eV between the Ce $4f$ and $5d$ bands.

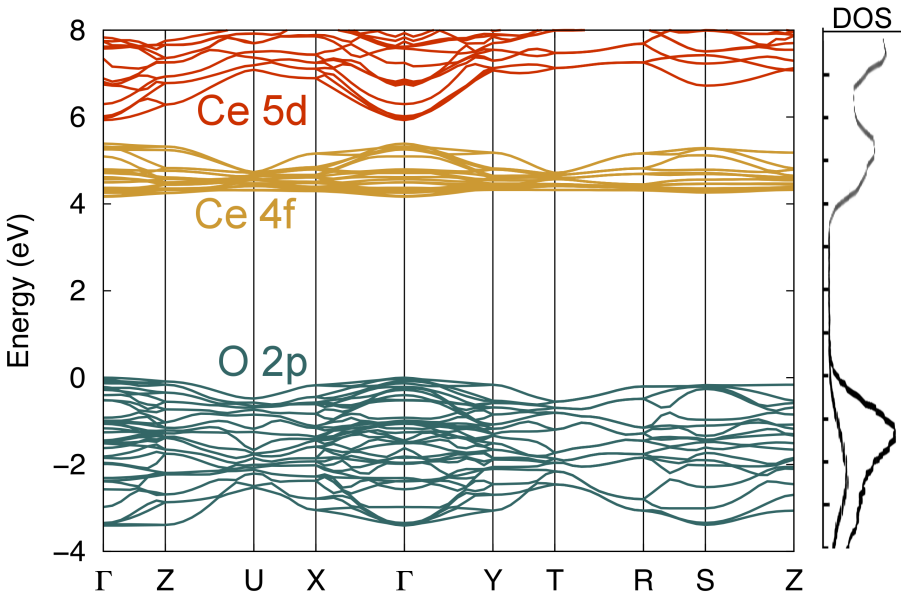

Figure 6.2: Band structure of $BaCeO_3$ as calculated with HSE, plotted along the high-symmetry lines illustrated in Fig. 6.1(b). The valence bands are primarily O $2p$ states. The band gap is 4.17 eV. The lowest conduction bands are composed of Ce $4f$ states; they are separated from the higher-lying Ce $5d$ states by a gap of 0.54 eV. The experimental density of states from Ref. [131] is plotted on the right-hand side for comparison.

HSE corrects the band-gap problem of the commonly-used GGA of Perdew, Burke, and Ernzerhof (PBE) [5], which predicts a gap of 2.21 eV for $BaCeO_3$. HSE also reduces the width of the $4f$ band and narrows the gap between the $4f$ and $5d$ bands as compared to PBE results. This brings the band structure into good agreement with experimental density of states results [131], as shown in Figure 6.2.

6.3.3 Formation Energies

Formation energies are calculated using the methodology described in Sec. 2.7. We used an experimental value of 98 for the static dielectric constant, calculated from the capacitance measurements and experimental geometry of Ref. [135]. Due to the high value of the dielectric constant, the magnitude of Δ^q is small (of order a few 0.01 eV and uniformly less than 0.07 eV). The equilibrium conditions limiting the chemical potentials of the relevant atomic species are as follows:

$$\mu_{\mathrm{Ba}} + \mu_{\mathrm{Ce}} + 3\mu_{\mathrm{O}} = \Delta H_f(\mathrm{BaCeO_3}), \tag{6.2}$$

where $\Delta H_f(\mathrm{BaCeO_3})$ is the formation enthalpy of $BaCeO_3$. In order to prevent formation of bulk Ba and Ce phases, and to prevent loss of O_2, the chemical potentials are bounded from above by

$$\mu_{\mathrm{Ba}}, \mu_{\mathrm{Ce}}, \mu_{\mathrm{O}} \leq 0. \tag{6.3}$$

To prevent formation of secondary BaO, BaO_2, CeO_2 and Ce_2O_3 phases, it is also required that:

$$\mu_{\mathrm{Ba}} + \mu_{\mathrm{O}} \leq \Delta H_f(\mathrm{BaO}), \tag{6.4}$$

$$\mu_{\mathrm{Ba}} + 2\mu_{\mathrm{O}} \leq \Delta H_f(\mathrm{BaO_2}), \tag{6.5}$$

$$\mu_{\mathrm{Ce}} + 2\mu_{\mathrm{O}} \leq \Delta H_f(\mathrm{CeO_2}), \text{and} \tag{6.6}$$

$$2\mu_{\mathrm{Ce}} + 3\mu_{\mathrm{O}} \leq \Delta H_f(\mathrm{Ce_2O_3}). \tag{6.7}$$

The quantities $\Delta H_f(\mathrm{BaO})$, $\Delta H_f(\mathrm{BaO_2})$, $\Delta H_f(\mathrm{CeO_2})$ and $\Delta H_f(\mathrm{Ce_2O_3}))$ are the enthalpies of formation of BaO, BaO_2, CeO_2 and Ce_2O_3, respectively, and these are calculated from first principles and listed in Table 6.2. The inequalities above allow us to describe the region of chemical potentials in the μ_{Ce}-μ_{O} plane for which $BaCeO_3$ is stable.

It is worth noting that PBE has been shown to outperform HSE in the calculation of the reduction energy of CeO_2 to Ce_2O_3 [134, 136]. However, the HSE formation enthalpies themselves are closer to experiment; the PBE reduction energies are accurate due to a cancellation of errors in formation enthalpies for the particular case of ceria [134]. To allow comparison with other materials and to maintain consistency with the electronic structure calculations we have chosen to use HSE throughout this work.

Fig. 6.3 shows the resulting phase diagram for the system. For a fixed μ_{O}, we observe that $BaCeO_3$ forms in a narrow μ_{Ce} window of width 0.26 eV. For our calculations of defect formation energies, we fix μ_{Ce} as a function of μ_{O} by assuming the system lies on a line running through the middle of the $BaCeO_3$ region of stability (which is quite narrow). We can then choose μ_{O} to reflect different growth conditions. For impurities, we perform similar calculations to fix μ_{H} (limited by formation of H_2O) and μ_{Y} (limited by the formation of Y_2O_3). Thus the only remaining variable is μ_{O}. For the calculation of formation energies, we considered two values: $\mu_{\mathrm{O}} = -0.42$ eV (near the oxygen rich

Table 6.2: Calculated enthalpy of formation per formula unit of barium cerate and the possible limiting phases. Experimental values [137, 138] are provided for comparison.

Compound	ΔH_f (eV)	
	Theory	Experiment
$BaCeO_3$	-17.23	-17.52
BaO	-5.10	-5.68
BaO_2	-5.77	-6.57
CeO_2	-11.61	-11.30
Ce_2O_3	-19.75	-18.65
H_2O	-2.67	-2.51
Y_2O_3	-19.18	-19.74

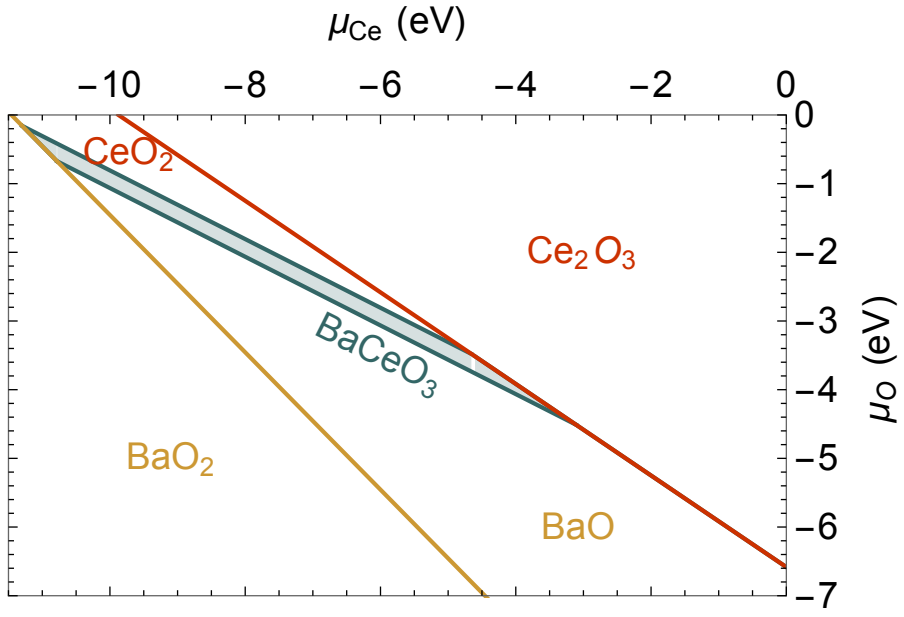

Figure 6.3: Phase diagram of $BaCeO_3$. The region of cerium and oxygen chemical potentials for which $BaCeO_3$ is stable is indicated by the (green) shaded region. Above this region, CeO_2 will form. Below this region, BaO or BaO_2 will form.

limit) and $\mu_O = -2.5$ eV (relatively oxygen poor, corresponding to O_2 gas at 1100 K and 0.1 MPa [139]).

Following Eq. (2.15), we calculate the formation energy of various defects and defect complexes in all possible charge states. We plot the formation energies by finding the most stable charge state at each value of the Fermi level, and then plotting the energy of that charge state (Fig. 6.4). Note that using Y_2O_3 as the solubility-limiting phase for μ_Y leads to the lowest possible formation energy for Y_{Ce} defects before precipitation of Y_2O_3. Realistic μ_Y values will be lower, and formation energies correspondingly higher.

Figure 6.4 shows that the formation energy of Y_{Ce} is low, and hence the impurity will easily incorporate in the lattice, particularly under more oxygen-rich (=cerium-poor) conditions. The incorporation of yttrium, which acts as an acceptor, will drive the Fermi level down, which in turn promotes the incorporation of point defects or impurities with donor character, such as oxygen vacancies or hydrogen. Charge neutrality between the positively charged donors and the negatively charged acceptors will then determine the position of the Fermi level. Hydrogen impurities have low formation energies, which enables high solubility and is conducive to good proton conduction.

When hydrogen and yttrium are simultaneously present, $Y_{Ce}^{-} + H_i^{+}$ complexes will easily form. This may impede proton diffusion. To assess the impact of these complexes, we calculate a binding energy of hydrogen to the yttrium impurity. The binding energy E_b between two entities A and B when they form a complex AB is defined by adding the formation energies of the isolated species and subtracting the energy of the complex [140]:

$$E_b(AB) = E^f(A) + E^f(B) - E^f(AB) \tag{6.8}$$

Calculated values are listed in Table 6.3. While the binding energy between Y_{Ce}^{-} and H_i^{+} is relatively modest (0.26 eV), it is sizeable on the scale of the proton migration barrier

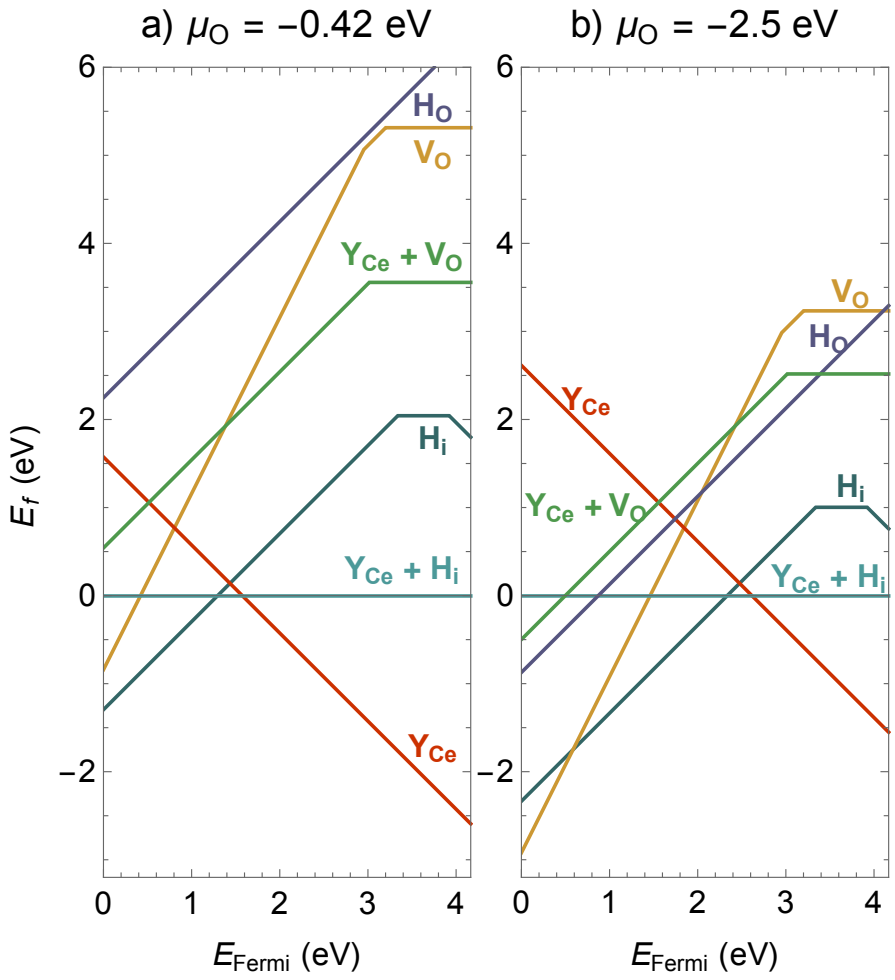

Figure 6.4: Calculated formation energies of various impurities, defects, and complexes as a function of Fermi level for given values of the oxygen chemical potential.

Table 6.3: Calculated binding energies of defect complexes and between defects and polarons in barium cerate, as given by Eq. (6.8).

Complex	Binding Energy (eV)
$Y_{Ce}^{-} + H_i^{+}$	0.26
$Y_{Ce}^{-} + V_O^{2+}$	0.19
$H_i^{+} + e_{polaron}^{-}$	0.05
$V_O^{2+} + e_{polaron}^{-}$	0.44
$V_O^{2+} + 2\,e_{polaron}^{-}$	0.62
$Y_{Ce}^{-} + h_{polaron}^{+}$	0.22

in this material (0.22 to 0.58 eV) [141]. In equilibrium, at a given temperature, Y_{Ce}^{-}-H_i^{+} complexes will only be present in concentrations larger than those of the isolated species if the binding energy of 0.26 eV exceeds the formation energies of the isolated species [142]; however, even if this criterion is not met, trapping of hydrogen at Y impurities may impact kinetics.

If yttrium forms a complex with an oxygen vacancy, the resulting entity is positively charged over a range of Fermi levels between 0 and almost 3 eV; such positive charged complexes would not trap protons, due to Coulomb repulsion. Formation of such complexes would therefore be desirable, but unfortunately the binding energy is quite small (0.19 eV, Table 6.3) and hence they are unlikely to occur.

6.3.4 Polarons

We expect that localization of carriers will be important in barium cerate, due to the relatively flat dispersion of the bands. This localization manifests itself in the form of polarons: localized electrons together with a lattice distortion. In our calculations, we form an isolated polaron by introducing an extra electron into bulk $BaCeO_3$ and locally breaking the symmetry of the lattice through small perturbations of the atomic positions.

This allows an electron to localize near the perturbation. The lattice is then allowed to relax, forming a polaron. The energy of this configuration is lower than that of an electron in the conduction-band minimum, and the energy difference is the self-trapping energy.

Our calculations show that polaron formation is extremely favorable for an electron in the conduction band [Fig. 6.5(a)]: the self-trapping energy is 780 meV. A hole polaron in the valence band has a smaller, but still significant, self-trapping energy of 150 meV. An electron polaron on a cerium atom stretches the Ce-O bond length by 2% and decreases Ce-O-Ce angles by 2%. This distortion is highly localized; the displacements from the nominal lattice sites are smaller than the calculational error bars already for cerium atoms directly adjacent to the polaron. This high degree of localization of the lattice distortion indicates that electrons in $BaCeO_3$ localize in the form of small polarons.

Polarons are likely to occur in the vicinity of defects that have a charge opposite to that of the carrier. This can be more energetically favorable than having electrons localize on the defect itself. The neutral charge state of interstitial hydrogen is an example. While H_i^- is a "genuine" defect state (the proton sits between two barium atoms and two electrons are localized on the defect center), we find that similar configurations with only one electron (H_i^0) are unstable. Instead, the proton tends to bond to an oxygen atom (as in H_i^+), while an electron polaron forms on an adjacent cerium atom. [Fig. 6.5(b)]. This leads to an entity that is overall neutral, but it would be inaccurate to describe this as "neutral interstitial hydrogen"since the electron is not localized on the defect center.

The case of oxygen vacancies is similar: the +1 charge state consists of $V_O^{2+} + e^-_{\text{polaron}}$, and the neutral charge state consists of $V_O^{2+} + 2e^-_{\text{polaron}}$ [Fig. 6.5(c)]. While the structure of the polaron bound to H_i^+ is similar to that of an isolated polaron, polarons bound to the oxygen vacancy have a different magnetic quantum number. This state is likely favored because it allows higher electron density near the positively charged defect center. When two polarons are bound to the same vacancy, they have opposite spins due to the partial

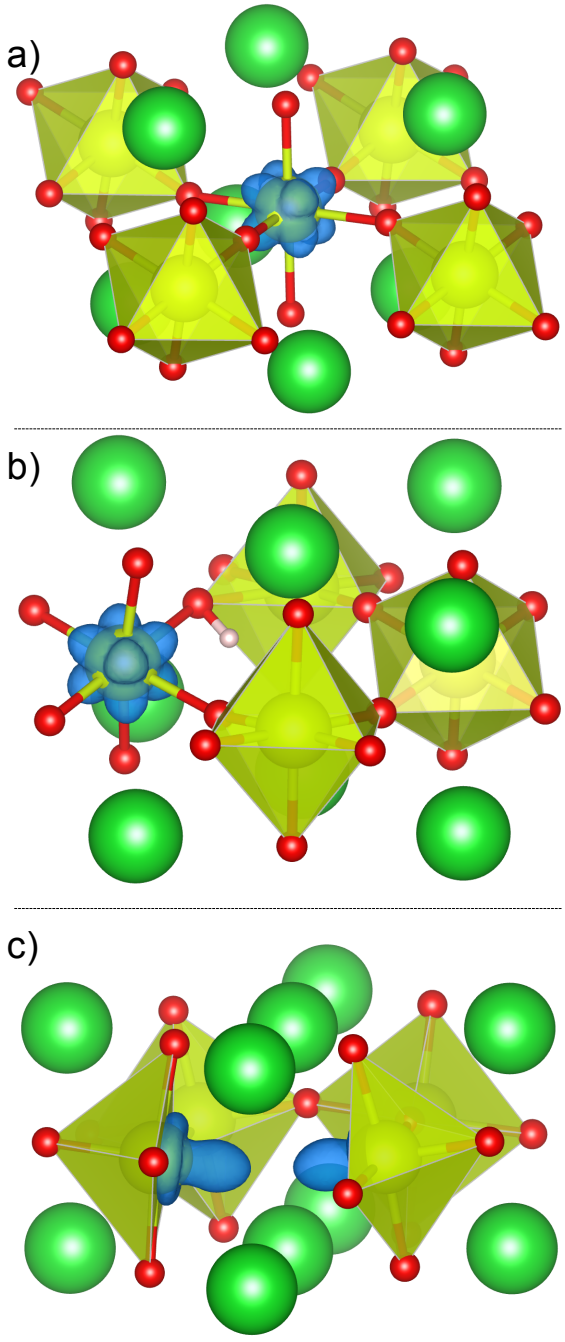

Figure 6.5: Visualization of the structure of electron polarons in various configurations: a) e^-_{polaron} in bulk; b) $H^+_i + e^-_{\text{polaron}}$; c) $V^{2+}_O + 2e^-_{\text{polaron}}$. Color coding as in Fig. 6.1; the hydrogen ion is white. Charge-density isosurfaces at 10% of the maximum are also shown (in blue) for the polaron state.

overlap of their wavefunctions at the defect center.

Binding energies of polarons to various donors in $BaCeO_3$ are listed in Table 6.3. Note that when two polarons are bound to an oxygen vacancy, the energy cost to remove one of the polarons is only 0.18 eV.

In order to study the hopping of polarons, we calculated the energies of a series of structures with atomic positions interpolating between polaron configurations on two adjacent sites. The highest energy among these structures has roughly half of the polaron localized on both sites. This was taken to be the transition state for hopping between the sites, and its energy (referenced to the relaxed polaron) is the activation energy for polaron hopping. This activation energy is 0.29 eV for in-plane hopping ($\perp$ c) and 0.31 eV for out-of-plane hopping ($\parallel$ c).

6.3.5 Optical Properties

Our first-principles studies allow for the calculation of optical properties, including the energetics of radiative transitions [143]. We have applied this methodology to barium cerate. Our results for key processes are presented in Table 6.4, and two important cases are illustrated in Fig. 6.6. In these diagrams, the horizontal axis is a generalized "configuration coordinate": atomic configurations were generated by interpolating the atomic positions between two structures. In Fig. 6.6(a) the first structure corresponds to the atomic configuration for the ground state of the oxygen vacancy in a 2+ charge state, and the second structure to the atomic configuration for the ground state of the oxygen vacancy in a + charge state. The generalized coordinate is thus representative of the displacements of atoms surrounding the oxygen vacancy as the charge state is changed. In Fig. 6.6(b) the first structure corresponds to the atomic positions in bulk $BaCeO_3$, and the second structure to the atomic configuration corresponding to an elec-

Table 6.4: Calculated energy peaks of optical absorption and emission processes in barium cerate. h^+_{VBM} indicates a hole at the valence-band maximum (VBM), and e^-_{CBM} indicates an electron at the conduction-band minimum (CBM).

Ground state	Excited state	Absorption (eV)	Emission (eV)
H_i^+	$\mathrm{H}_i^0 + h^+_{\mathrm{VBM}}$	4.25	2.31
$\mathrm{V}_{\mathrm{O}}^{2+}$	$V_{\mathrm{O}}^+ + h^+_{\mathrm{VBM}}$	3.38	2.43
Bulk	$h^+_{\mathrm{polaron}} + e^-_{\mathrm{CBM}}$	4.17	2.99
Bulk	$e^-_{\mathrm{polaron}} + h^+_{\mathrm{VBM}}$	4.17	2.43

tron polaron. Here, the coordinate represents the relaxation of (mainly) oxygen atoms away from the localizing electron (cf. Sec. 6.3.4). For each intermediate configuration, the electronic structure was solved self-consistently. The upward-pointing arrow illustrates the formation of an electron-hole pair through absorption of a photon. Absorption is followed by lattice relaxation through phonon-mediated nonradiative processes. The downward-pointing arrow illustrates the luminescence step, in which the electron-hole pair recombines radiatively, emitting a photon. Finally, the lattice goes through another phonon-mediated relaxation into the ground-state configuration. A full description of these processes would involve transitions between vibronic states, and would allow the prediction of luminescence lineshapes [143]. Here, we focus on the most probable radiative transitions, which are represented by the arrows in Fig. 6.6 and correspond to peaks in absorption or luminescence spectra; these peak energies are listed in Table 6.4.

Kompan *et al.* [144] reported luminescence spectra for $BaCeO_3$ prepared under various conditions. The authors observed luminescence peaks at 2.48 and 2.92 eV after sub-gap UV excitation. They suggested that this luminescence originated from the capture of an electron in the conduction band by a cerium atom to form Ce^{3+}, i.e., an electron polaron. The formation of a polaron from an electron in the conduction band involves

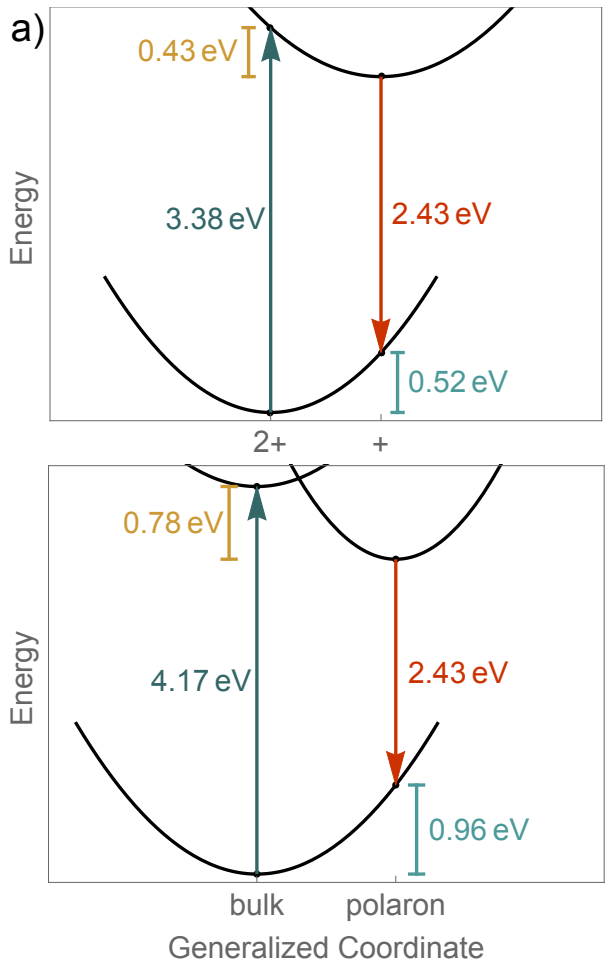

Figure 6.6: a) Configuration coordinate diagram illustrating absorption and luminescence processes associated with oxygen vacancies. The lower parabola represents an oxygen vacancy in its 2+ charge state, while the upper parabola represents the 1+ charge state. We predict absorption peaked near 3.4 eV and luminescence peaked around 2.4 eV. b) Configuration coordinate diagram showing band-to-band absorption, polaron formation, and luminescence due to radiative recombination of the polaron with a free hole. The lowest parabola represents the bulk, the highest parabola represents the bulk with an e^-, h^+ pair, and the intermediate parabola represents an electron polaron. We predict this process will also contribute to the luminescence peak near 2.4 eV.

an energy gain of 0.78 eV, a phonon-assisted process that is nonradiative. We therefore feel the luminescence mechanism proposed in Ref. [144] cannot be correct. Instead, we propose a process in which the incoming 3.68 eV photons in the experiment can excite $V_{\mathrm{O}}^{2+} \rightarrow V_{\mathrm{O}}^{+} + h_{\mathrm{VBM}}^{+}$. Our calculated 2.43 eV luminescence peak corresponding to $V_{\mathrm{O}}^{+} + h_{\mathrm{VBM}}^{+} \rightarrow V_{\mathrm{O}}^{2+}$ is in very good agreement with the observed peak at 2.48 eV, and our 2.99 eV peak for $h_{\mathrm{polaron}}^{+} + e_{\mathrm{CBM}}^{-}$ is in very good agreement with the observed peak at 2.92 eV. Kompan *et al.* also reported that the luminescence signal disappears when the sample is prepared in an oxygen-rich environment, supporting our attribution of the signal to oxygen vacancies.

6.4 Conclusions

We have investigated the structural and electronic properties of barium cerate, and shown that they are well described by DFT using a hybrid exchange-correlation functional. Formation, properties, and interactions were calculated for the impurities and intrinsic defects that are most relevant for proposed applications. We have found that polaron formation is an important phenomenon in the study of $BaCeO_3$, and it is essential to take the effects of polarons into account when describing the behavior of defects and impurities. These effects have been explored in detail, calculating formation energies, favorable charge states, polaron binding energies, and optical transition levels. In Chapter 7, we will compare the case of $SrCeO_3$, in which the same general principles hold. We expect this also to be the case in the case of other cerium-containing oxides such as CeO_2.

Chapter 7

Impact of Point Defects on Proton Conduction in Strontium Cerate

7.1 Introduction

Hydrogen readily incorporates in many oxides with the perovskite crystal structure.[145, 146, 122] Strontium cerate ($SrCeO_3$) (Fig. 7.1) has been investigated for use in numerous applications, including solid oxide fuel cells, hydrogen sensors, and steam electrolysis [147, 148, 149, 150]. Acceptor dopants are typically introduced to enhance the stability and increase the proton solubility; during this process, oxygen vacancies are created to compensate for the acceptors. Subsequent exposure to H_2O then leads to incorporation of hydrogen while simultaneously removing oxygen vacancies [151]. After this exchange has taken place, hydrogen plays the role of the compensating donor, but the preparation technique potentially leaves a sizeable fraction of oxygen vacancies in the samples. In spite of the critical role played by hydrogen in $SrCeO_3$, the microscopic mechanisms of its incorporation and interactions with other defects and impurities have not yet been explored in detail.

As discussed in Chapter 6, computational studies using density functional theory (DFT) have often encountered obstacles when attempting to describe cerium-containing compounds [152], particularly with regard to the strongly localized $4f$ electrons. Exchange-correlation functionals such as the local density approximation (LDA) or the generalized gradient approximation (GGA) tend to over-delocalize carriers, leading to a poor description of systems in which localization plays a central role. This shortcoming can be addressed by using hybrid functionals, which combine exact Hartree-Fock exchange with GGA, and have been shown to improve the description of strongly localized carriers [124, 125, 126, 127]. Hybrids also correct the "band-gap problem" of traditional functionals [128], and have been successfully applied to the study of defects in many semiconductors and insulators. We therefore expect DFT with a hybrid functional to describe strontium cerate accurately. To our knowledge, this is the first application of hybrid functionals to this material.

In this work, we provide a thorough microscopic description of proton conduction and the factors that can affect it. We first investigate the thermodynamics of $SrCeO_3$ formation and its decomposition into various alternate phases. We calculate the electronic band structure and perform a slab calculation to find the absolute position of the bands with respect to the vacuum level; this provides insight into the electronic character of the material and the likelihood of donor versus acceptor incorporation. Next, we look at proton conducting behavior directly, predicting the energetics of hydrogen incorporation, its location in the crystal lattice, the strength of its interactions with other defects, and energy barriers to migration. We also investigate vacancies of strontium and cerium, which act as acceptors and are therefore expected to strongly interact with protons and potentially act as traps. Comparisons with our results in barium cerate (Chapter 6) establish trends across these well-known proton conductors.

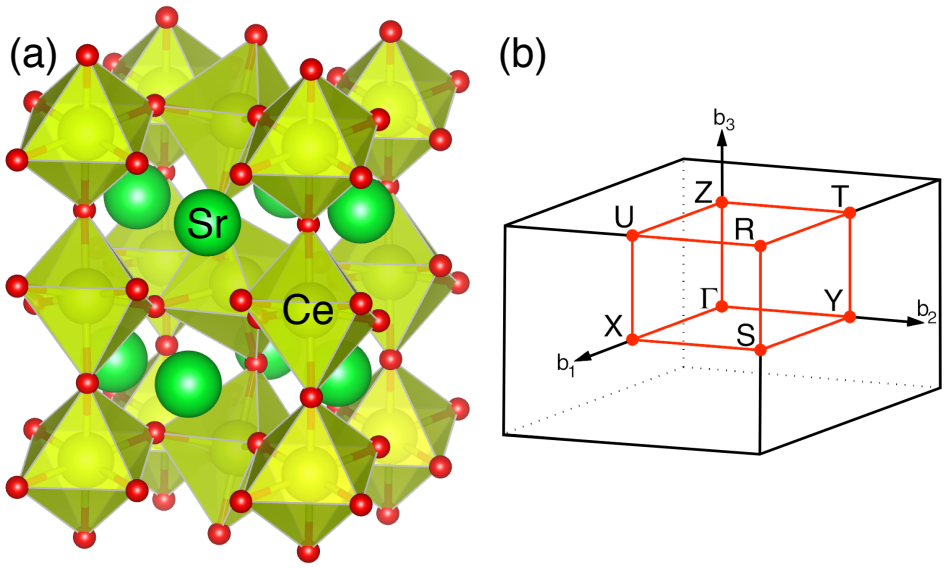

Figure 7.1: (a) Visualization of the crystal structure of strontium cerate. Cerium–centered octahedra are yellow, strontium ions are green, and oxygen ions are red. $SrCeO_3$ occurs in the perovskite crystal structure. The unit cell is orthorhombic due to octahedral tilting. (b) High-symmetry points in the first Brillouin zone of an orthorhombic lattice. Lines connecting the points indicate the conventional path for band-structure plots [110].

7.2 Computational methods

Our calculations use the general methodology described in Chapter 2.

All calculations used the HSE hybrid functional with standard parameters (HSE06). The cerium pseudopotential included 46 electrons in the core ([Kr] $4d^{10}$), so the PAW calculation contained 12 valence electrons per cerium ($5s^2 5p^6 4f 5d 6s^2$). The 20-atom unit cell was used for calculation of lattice parameters and band structure. The Brillouin zone was sampled using a $4 \times 4 \times 4$ Monkhorst-Pack grid [129]. Defects were introduced into a 160-atom supercell to minimize interaction with periodic images. The supercells used a single special k-point, $k = (0.25, 0.25, 0.25)$. The plane-wave energy cutoff for all calculations was 400 eV.

Surface calculations were performed for slabs oriented in the (001) direction with a CeO_2 termination on both sides. The slabs contained 4 CeO_2 and 3 SrO layers (approximately 13 Å total thickness). The vacuum spacing between slabs was 21 Å. Tests indicate the results are converged to within 0.01 eV with respect to vacuum spacing.

Formation energies are calculated using the methodology described in Sec. 2.7. We used an experimental value of 68, calculated from the bulk capacitance measurements of Ref. [153].

Migration barriers were calculated by finding the minimum-energy path with the climbing image nudged elastic band method [154]. The migration barrier is the total energy difference between the saddle-point configuration and the stable configuration. The path was found using PBE [5] rather than HSE to reduce computational cost, but the saddle-point energy was then calculated using HSE for greater accuracy. This method has been used with success to calculate migration barriers in other materials [155].

Table 7.1: Structural parameters of $SrCeO_3$ and comparison with $BaCeO_3$. Calculated results based on HSE; experimental values from Ref. [158]. The angles are for Ce-O-Ce and measure octahedral tilting: $\angle_1 = \angle_2 = 180°$ for a cubic perovskite. The degree of tilting is different along different directions: $\angle_1$ is the angle involving cerium atoms separated along the c direction, and $\angle_2$ involves cerium atoms which lie in the plane perpendicular to the c axis.

	$SrCeO_3$		$BaCeO_3$	
	Theory	Exp	Theory	Exp
a (Å)	5.945	6.012	6.233	6.237
b (Å)	6.103	6.154	6.223	6.218
c (Å)	8.506	8.589	8.782	8.780
$\angle_1$	146.3°	146.9°	159.4°	158.8°
$\angle_2$	144.0°	144.9°	156.6°	156.1°

7.3 Results

7.3.1 Structural parameters

Strontium cerate is a perovskite with an orthorhombic unit cell (Fig. 7.1), space group *Pbnm*. The structural parameters as calculated by HSE are shown in Table 7.1 and show good agreement with experiment. As typical of an orthorhombic perovskite, the cerium-centered octahedra are tilted. The a and b lattice parameters are very similar. For comparison, Table 7.1 also shows the calculated parameters of $BaCeO_3$ from Sec. 6.3.1. $SrCeO_3$ has a smaller lattice parameter and more significant octahedral tilting, due to the smaller ionic radius of strontium as compared to barium. This effect is quantified by the Goldschmidt tolerance factor t [156], which is calculated based on the ionic radii of the constituents and can predict the level of distortion in a perovskite. For $SrCeO_3$, $t = 0.80$, less than $t = 0.86$ for $BaCeO_3$. This leads to a greater distortion from the cubic phase; the latter is seen in perovskites with $0.89 \leq t \leq 1.0$ [157].

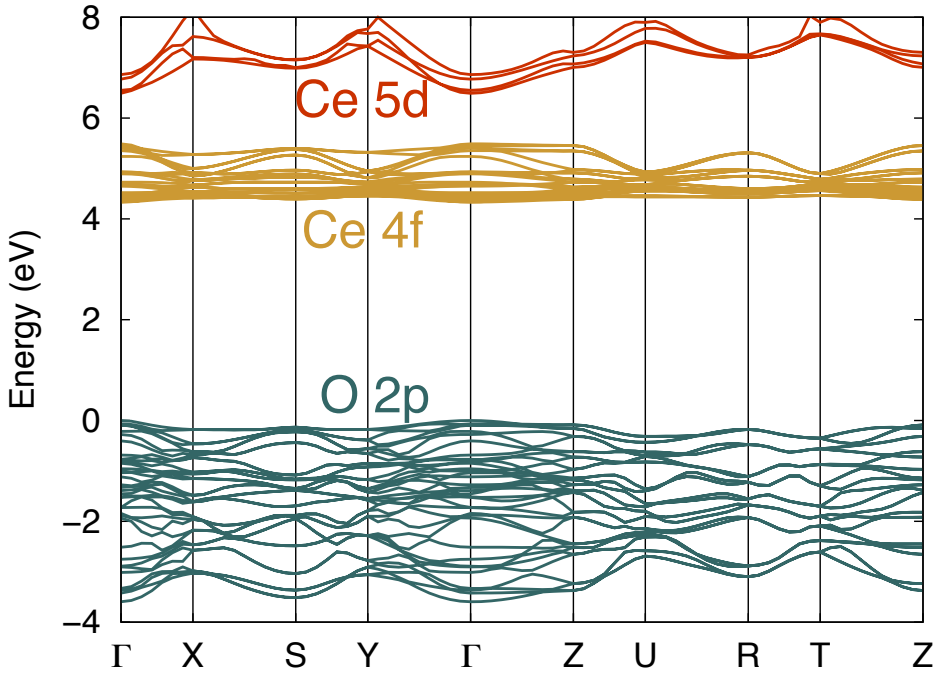

Figure 7.2: HSE band structure of $SrCeO_3$, plotted along the high-symmetry path illustrated in Fig. 7.1(b). The valence bands have primarily O $2p$ character, the lowest conduction bands are composed of Ce $4f$ states, and the next higher bands are Ce $5d$ states. The 4.33 eV band gap is direct $\Gamma \rightarrow \Gamma$. The $4f$ and $5d$ states are separated by a second gap of width 1.00 eV.

7.3.2 Band structure

Figure 7.2 shows the calculated band structure of strontium cerate. The accuracy of HSE in producing the gap of $BaCeO_3$ (Sec. 6.3.2) provides us with confidence that the predicted gap value of 4.33 eV for $SrCeO_3$ is also accurate. Experimental measurements have yielded a variety of values, ranging from 3.5 eV based on electron energy loss spectroscopy and diffuse reflection [152], to 5-6 eV based on optical absorption [159]. The present hybrid functional results represent an improvement over the results given by traditional functionals such as PBE, which underestimate the gap [152].

7.3.3 Chemical potentials and phase stability

As discussed in Sec. 2.7, the atomic chemical potentials μ_i are subject to various constraints:

$$\mu_{\mathrm{Sr}}, \mu_{\mathrm{Ce}}, \mu_{\mathrm{O}} \leq 0, \tag{7.1}$$

$$\mu_{\mathrm{Sr}} + \mu_{\mathrm{Ce}} + 3\mu_{\mathrm{O}} = \Delta H_f(\mathrm{SrCeO_3}), \tag{7.2}$$

$$\mu_{\mathrm{Sr}} + \mu_{\mathrm{O}} \leq \Delta H_f(\mathrm{SrO}), \tag{7.3}$$

$$\mu_{\mathrm{Sr}} + 2\mu_{\mathrm{O}} \leq \Delta H_f(\mathrm{SrO_2}), \tag{7.4}$$

$$\mu_{\mathrm{Ce}} + 2\mu_{\mathrm{O}} \leq \Delta H_f(\mathrm{CeO_2}), \text{and} \tag{7.5}$$

$$2\mu_{\mathrm{Ce}} + 3\mu_{\mathrm{O}} \leq \Delta H_f(\mathrm{Ce_2O_3}). \tag{7.6}$$

where $\Delta H_f(\mathrm{X})$ is enthalpy of formation of compound X. Expression (7.1) avoids formation of bulk Sr and Ce phases and prevents loss of O_2, (7.2) ensures that $SrCeO_3$ is thermodynamically stable, and (7.3)-(7.6) exclude formation of secondary BaO, BaO_2, CeO_2 and Ce_2O_3 phases. Enthalpies of formation are calculated from first principles and listed in Table 7.2. The inequalities above allow us to describe the region of chemical potentials in the μ_{Ce}-μ_{O} plane for which $SrCeO_3$ is stable.

The phase diagram of this system in μ_{O}-μ_{Ce} space is shown in Fig. 7.3. For a fixed μ_{O}, the window of $SrCeO_3$ stability in μ_{Ce} is only 0.05 eV wide. In order to calculate defect formation energies, we fix μ_{Ce} as a function of μ_{O} by assuming the system is in the middle of the $SrCeO_3$ region of stability. We perform similar calculations to fix μ_{H} (limited by formation of H_2O) and μ_{Y} (limited by the formation of Y_2O_3). Thus the only remaining variable is μ_{O}, which we adjust to reflect different growth conditions. We considered two values: $\mu_{\mathrm{O}} = -0.17$ eV (point A in Fig. 7.3, near the oxygen-rich limit) and $\mu_{\mathrm{O}} = -2.5$ eV (point B in Fig. 7.3, relatively oxygen-poor, corresponding to O_2 gas

Table 7.2: Enthalpy of formation of $SrCeO_3$ and possible precipitates. Experimental values [137, 138] are provided for comparison.

Compound	ΔH_f (eV)	
	Theory	Experiment
$SrCeO_3$	-17.36	-17.49
SrO	-5.64	-6.13
SrO_2	-5.88	-6.57
CeO_2	-11.61	-11.30
Ce_2O_3	-19.75	-18.65
H_2O	-2.67	-2.51
Y_2O_3	-19.18	-19.74

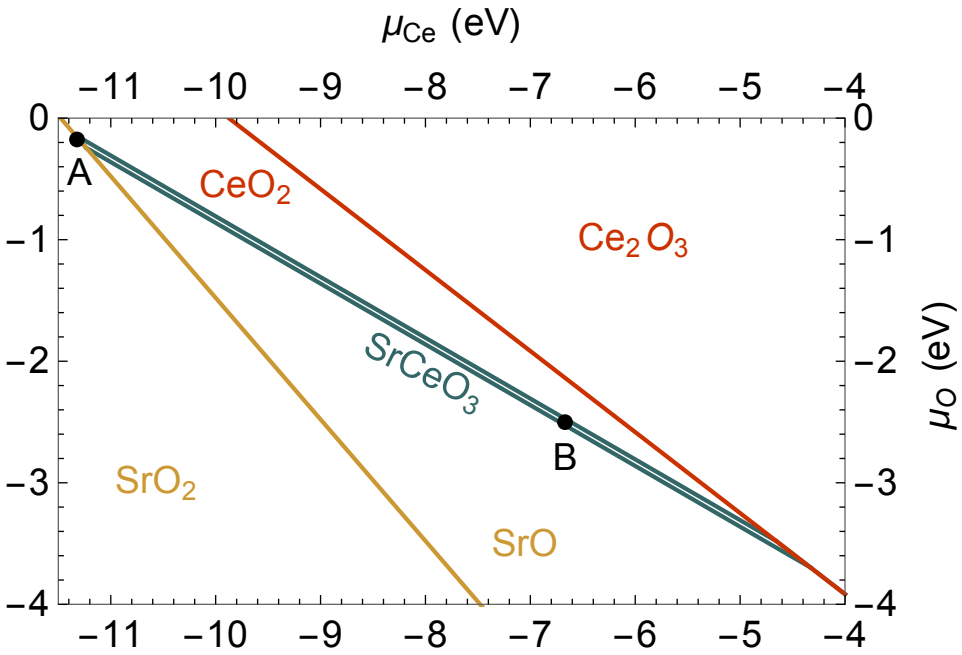

Figure 7.3: Phase diagram of $SrCeO_3$. The dominant phase for each region of cerium and oxygen chemical potentials is indicated. The region of stability for $SrCeO_3$ is indicated by the narrow (green) shaded region. Chemical potential conditions used for plotting formation energies in Fig. 7.4 are at points A and B.

at 1100 K and 0.1 MPa [139]).

The phase diagram of $BaCeO_3$ is similar, but the window of stability is wider (0.26 eV) and extends approximately 1 eV lower in oxygen chemical potential (Figure 6.3). This suggests that stability concerns may be even more important in $SrCeO_3$ than in $BaCeO_3$.

7.3.4 Point defects and impurities

Formation energies for defects and impurities in various charge states are calculated using Eq. (2.15) and plotted as a function of Fermi level in Fig. 7.4. For each Fermi-level position, only the most stable charge state of a given defect is plotted. As may be seen from Eq. (2.15), the slope of a line corresponds to its charge state, and therefore charge-state transition levels occur at kinks where the line changes slope.

There are two symmetry-inequivalent oxygen sites: "apical" and "in-plane" with reference to the plane perpendicular to the c axis. Our calculations find that a vacancy on the apical site is lower in energy by 27 meV, so the results shown are for apical oxygen vacancies. Similarly, there are 8 distinct hydrogen interstitial sites, four on each oxygen. We follow the numbering scheme of Ref. [141], in which sites are labeled with 1 or 2 (bonded to apical or in-plane oxygen respectively) and a, b, c, or d (according to the orientation of the bond). We used PBE tests to find the two lowest-energy configurations, and then compared them using HSE to find the minimum-energy site. We found that 1b (bonded to the apical oxygen, oriented in the same direction as the octahedral tilting) is the most stable, and 2b (bonded to the in-plane oxygen, oriented in the same direction as the octahedral tilting) is higher in energy by 64 meV.

Yttrium substituted on the cerium site is stable only in the negative charge state and thus acts as an electron acceptor at all Fermi levels. The possible donors that

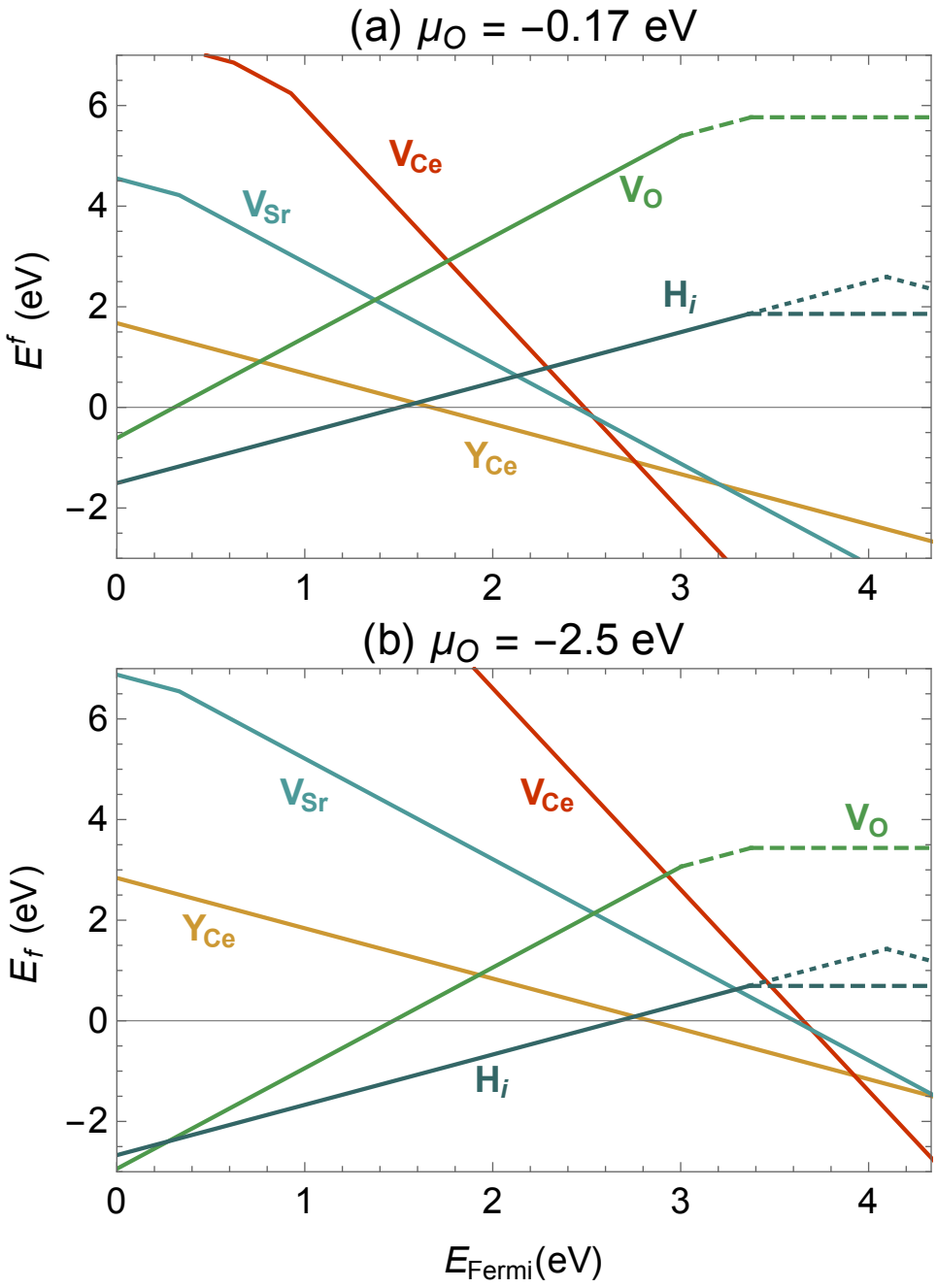

Figure 7.4: Calculated formation energies as a function of Fermi level in the gap, for two values of the oxygen chemical potential: (a) $\mu_O = -0.17$ eV and (b) $\mu_O = -2.5$ eV. Dashed segments for V_O and H_i indicate states which have one or more electron polarons localized on cerium ions adjacent to the defect, rather than localized on the defect itself as in a "true" defect state. Dotted lines for H_i^+ and H_i^- extend above the dashed line to show the +/− transition level at their intersection 4.10 eV above the VBM.

compensate the yttrium acceptor are oxygen vacancies (V_O) and hydrogen impurities (protons). Figure 7.4 shows that hydrogen has a lower formation energy than V_O. The formation energies plotted here assume equilibrium with H_2O, so we indeed find that upon exposure to water hydrogen becomes the most favorable donor in the system, replacing oxygen vacancies. This agrees with the experimental findings of Ref. [151].

The other point defects included in Fig. 7.4 are the Ce and Sr vacancies, both of which act as acceptors: V_{Ce} accepts four electrons, and V_{Sr} accepts two, consistent with the valence of these cations. The Fermi level of the system system is fixed by the requirement of overall charge neutrality. Since defect and impurity concentrations have an exponential dependence on formation energy [13], the Fermi level will be pinned very close to the point where two oppositely charged defects have the same formation energy. In the absence of any impurities, the Fermi level would be determined by equilibrium between V_O^{2+} and V_{Sr}^{2-}. Doping with yttrium lowers the Fermi level (and will hence reduce the concentration of V_{Ce} and V_{Sr}). Introducing hydrogen replaces V_O as the dominant donor and pushes the Fermi level higher. These qualitative considerations apply irrespective of the precise value of the oxygen chemical potential [Figs. 7.4 (a) and (b)].

For all of the Fermi levels that are relevant to the physical system, hydrogen prefers the positive charge state (H_i^+) and thus incorporates as an interstitial proton and acts as a donor. The proton interacts with an oxygen lone-pair electron, forming a covalent bond of length 1.01 Å oriented at a 6° angle from the c axis. It is also of interest to examine what happens at higher Fermi levels. Unlike its behavior in most other materials, in which interstitial hydrogen can assume different charge states [160], we find that the hydrogen in $SrCeO_3$ is intrinsically stable only in the positive charge state (i.e., as a proton). However, an electron can localize on a cerium ion adjacent to the proton, forming an electron polaron (much like in $BaCeO_3$, see Sec. 6.3.4). This can be equivalently viewed as a Ce^{4+} becoming Ce^{3+}). The polaron and the H_i^+ together make up an overall charge-

neutral entity represented by the horizontal part of the H_i line in Fig. 7.4 at Fermi levels above 3.36 eV. However, it would be inaccurate to call this state "H_i^0", since that would imply the electron was localized on the hydrogen itself. It should rather be denoted $H_i^+ + e^-_{\text{polaron}}$, and is thus indicated by a dashed line in the figure. It *is* possible to stabilize a negatively charged hydrogen interstitial, i.e., a true H_i^- state in which both electrons localize on the hydrogen, which is located between two strontium ions); however, this state is stable only for Fermi levels well above the conduction-band minimum, and thus it will not be observed. Still, its energy is of interest for band alignment as discussed below, and therefore we included it in Fig. 7.4.

The microscopic process by which a proton diffuses through the lattice is quite complicated, involving hops from an oxygen atom to one of many nearby oxygens as well as reorientations of the OH bond [141]. A full treatment of diffusion is beyond the scope of this work. In order to capture some of the physics involved, we calculated the migration barrier from a 2b site to a neighboring 2b site (see the second paragraph of this section for a discussion of proton sites). This path was chosen because it is a direct transfer between spatially separated but equivalent sites, and can thus lead to long-range diffusion on without separate reorientation steps. A visualization of hydrogen in an intermediate state during this diffusion process is shown in Figure 7.5. We found an activation energy of 0.67 eV, in good agreement with the experimental value of 0.63 eV [161]. This is slightly larger than the barrier in $BaCeO_3$, which is 0.22 to 0.58 eV from calculation [141] and 0.54 eV from experiment [162].

Protons moving through the lattice will interact with defects in the lattice, particularly negatively charged defects. We characterize this interaction by a binding energy, defined as

$$E_b(AB) = E^f(A) + E^f(B) - E^f(AB) \tag{7.7}$$

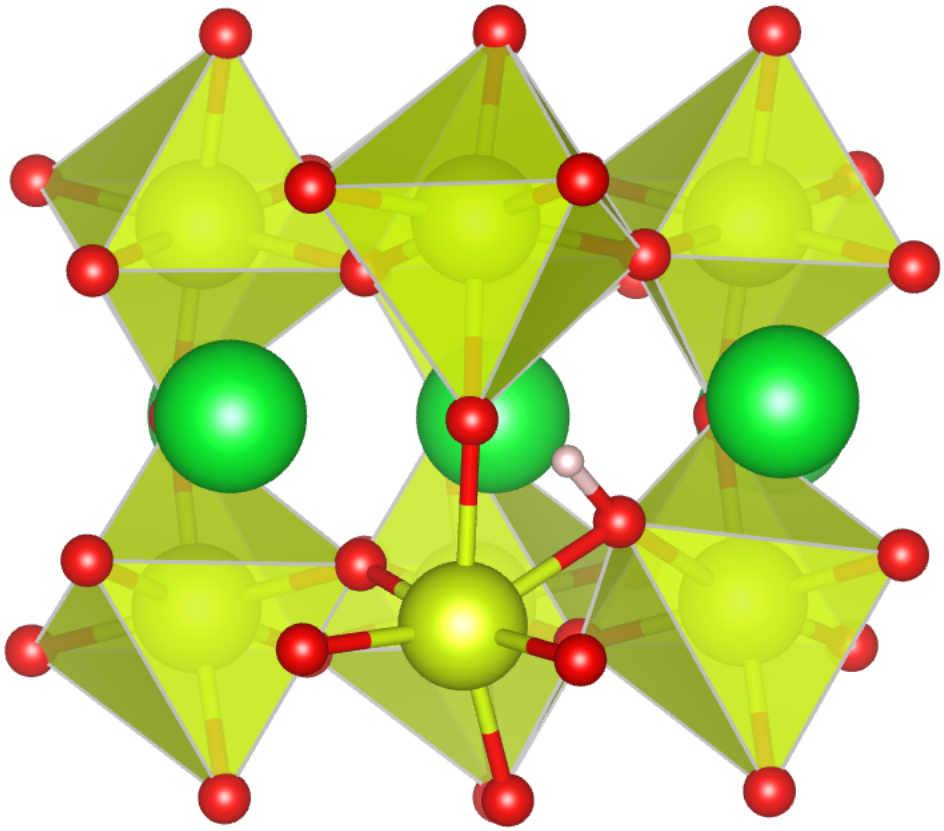

Figure 7.5: A proton in an intermediate state during the process of hopping from one equlibrium site to the next.

The binding energy of H_i^+ with Y_{Ce}^- is 0.18 eV. This is fairly small compared to the migration barrier (0.67 eV), and hence trapping at yttrium acceptors will not be a major concern for proton diffusion. Binding to cation vacancies is more significant. The binding energy of a proton with V_{Sr}^{2-} is 0.88 eV, and a second proton can bind with 7 meV. The binding energy of a proton with V_{Ce}^{4-} is 1.43 eV, and a second proton can bind with energy 1.07 eV. These large numbers indicate that any cation vacancies present in the material will trap hydrogen very effectively, and a significant concentration of these vacancies would negatively impact proton conductivity. Though the binding energy with yttrium is small, dopants are typically incorporated in concentrations well above the equilibrium concentrations of cation vacancies, so dopant sites may also be an important source of proton trapping. As we already discussed, doping with yttrium (or other acceptors) tends to reduce the concentration of cation vacancies, but for the relevant Fermi levels a significant concentration of V_{Ce}^{2-} and, in particular, V_{Sr}^{2-} may still be present, especially under oxygen-rich conditions [Fig. 7.4(a)]. The strong binding of hydrogen to the cation vacancies also implies that these vacancies will more readily form in the presence of hydrogen, since the vacancy-hydrogen complexes have lower formation energy than the bare vacancies. All of this points to the need for more detailed experimental characterization and better control of cation vacancies in the material.

7.3.5 Band alignment

Band alignments provide valuable information about the electronic properties of a solid. They of course determine the band offsets when two materials are joined at an interface, but the alignment of the band structure on an absolute energy scale also provides insight into the ability to dope a material n-type or p-type (see Sec. I.A.1 of Ref. [13]). To calculate the absolute position of the bands with respect to the vacuum we use a slab

geometry, following the approach of Ref. [163]. The geometry of the setup is visualized in Fig. 7.7. The slab is oriented in the (001) direction with CeO_2 layers at both surfaces to ensure mirror symmetry. The CeO_2 termination was chosen instead of the SrO termination because it gives more physically representative results. Additionally, the shared CeO_2 surface of $BaCeO_3$ and $SrCeO_3$ makes comparison more straightforward. The band alignment results are shown in Fig. 7.7, for both $SrCeO_3$ and $BaCeO_3$.

Another way of assessing the band alignment of materials is provided by the energy of the $+/-$ charge-state transition level of interstitial hydrogen, i.e., the Fermi level at which the $+$ and $-$ charge states of hydrogen have equal formation energy. It has been demonstrated [164, 165] that this level can serve as a means of aligning the band structures in many classes of materials. Figure 7.7 shows the position of this level within the band gaps of $SrCeO_3$ and $BaCeO_3$, confirming that it is indeed aligned across these two materials.

The position of the $+/-$ charge-state transition level of H_i level is expected to occur at about 4.5 eV below the vacuum level.[164] In $SrCeO_3$, this level is only 2.32 eV below the vacuum level (4.10 eV above the VBM). This discrepancy is due to the character of the positively charged hydrogen interstitial (H_i^+). In $SrCeO_3$, $BaCeO_3$, and many other perovskites, the proton strongly interacts with oxygen lone-pair electrons to form an O-H bond approximately 1 Å in length [166, 167, 168]. This is in contrast to the configuration of H_i^+ in the materials explored in Ref. [164], in which H_i^+ takes a bond-center or antibonding position. The lone-pair O-H configuration of $SrCeO_3$ is lower in energy than the bond-center or antibonding position, thus raising the energy of the $+/-$ transition level.

One might expect that the configuration in which H_i^+ is attached to the lone pair would not provide a suitable value for the $+/-$ level, since it is not in the spirit of the alignment physics discussed in Ref. [164]. However, as can be seen from Fig. 7.7, it turns

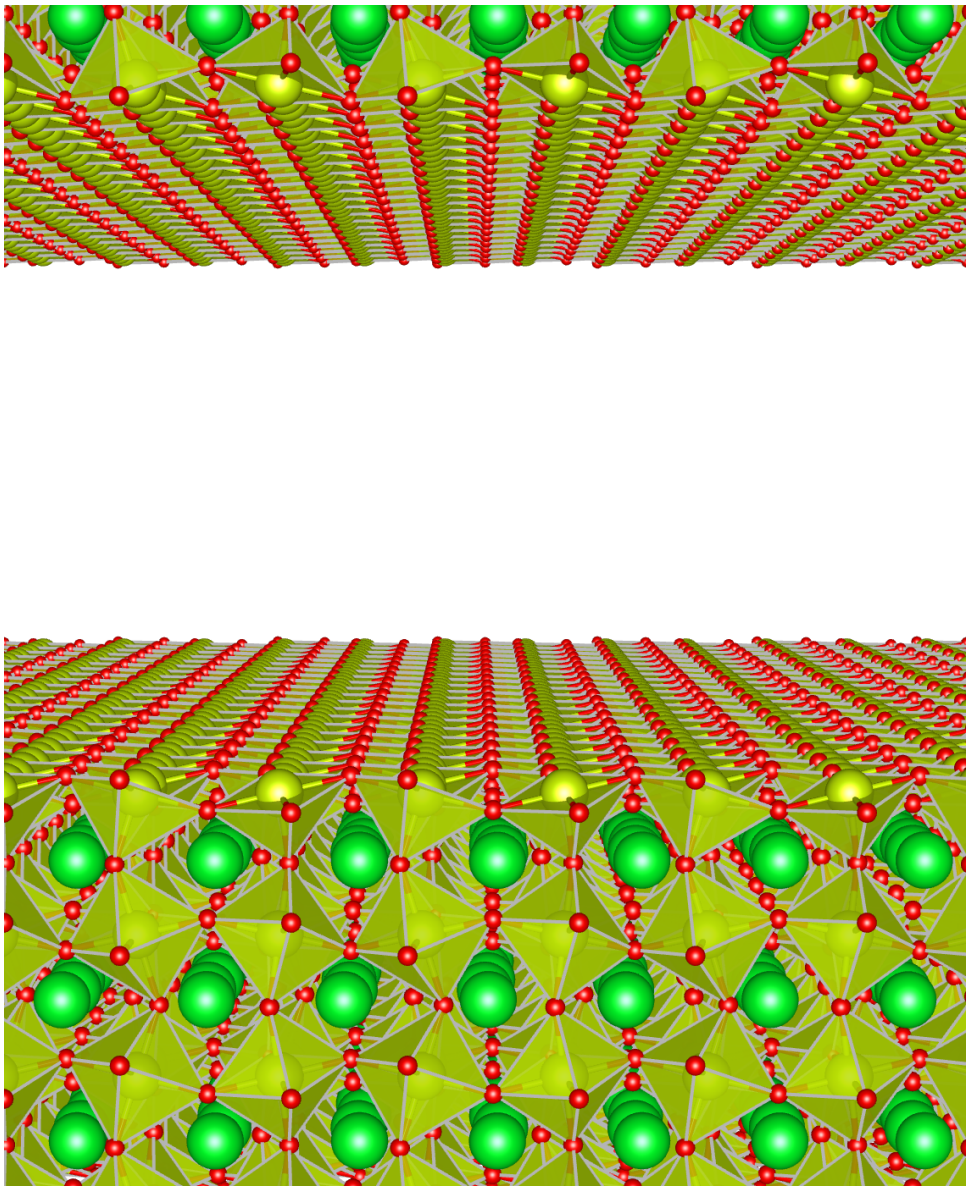

Figure 7.6: Perspective view of the $SrCeO_3$ slab used for surface calculation. The slab thickness is ∼13 Å, and vacuum spacing between slabs is 21 Å. Color coding of atoms as in Fig. 7.1.

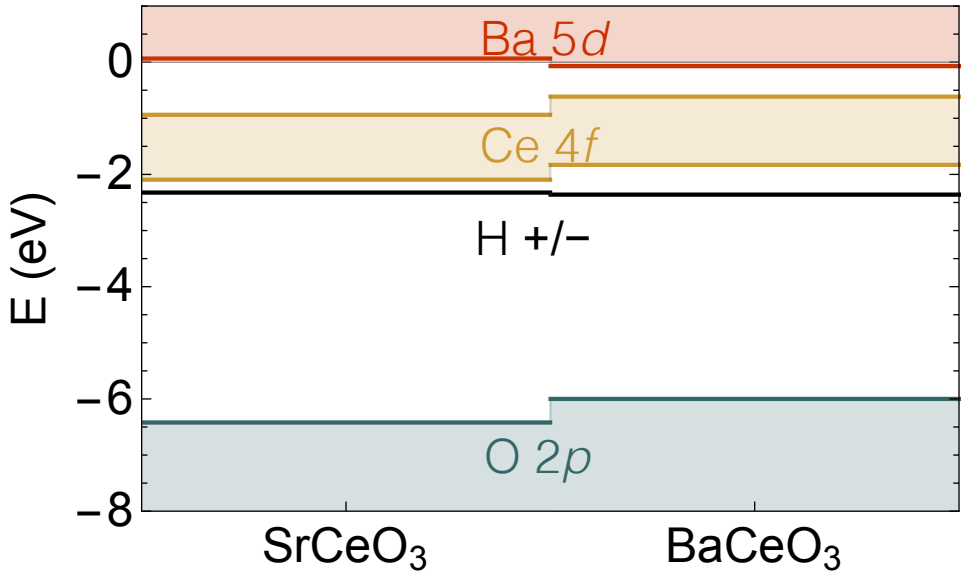

Figure 7.7: Band alignments of $SrCeO_3$ and $BaCeO_3$ on an absolute scale referenced to the vacuum level. Also shown is the hydrogen +/− transition level, which is found to be aligned within 50 meV across the two materials.

out that the level still serves as a reliable means of aligning the band structures of $SrCeO_3$ and $BaCeO_3$, probably due to the similarity of the two hosts.

7.4 Conclusions

We have calculated the structural and electronic properties of strontium cerate from first principles. The aim was to provide a comprehensive microscopic picture of proton conductivity in $SrCeO_3$, and establish trends across this class of proton conductors. This is the first time a hybrid functional has been applied to this material, as well as the first *ab initio* analysis of defects in this material. We mapped out the electronic structure, and based on surface calculations we found the alignment of the bands with respect to vacuum. We also compared the alignment of the bands in $BaCeO_3$, and found an alignment between hydrogen +/− transition levels in these materials.

We reported the behavior of various important point defects in $SrCeO_3$: hydrogen,

vacancies, and the common acceptor dopant yttrium. The migration barrier for hydrogen was calculated to be 0.67 eV, in very good agreement with experiment. The interactions between hydrogen and the other defects were studied. Strong binding energies between hydrogen and cation vacancies were found (0.88 eV with V_{Sr} and 1.43 eV with V_{Ce}). When present, these vacancies will strongly trap hydrogen and significantly impact proton conduction.

Chapter 8

Conclusions and Outlook

We have performed first-principles calculations to explore fundamental topics in condensed-matter physics with experimental relevance and real-world applications for energy and computation. Our work provides guidance for experimentalists and engineers, sheds light on open research questions, and paves the way for future work in these materials.

We began with silicon, the basis of modern electronics. Shallow donors in silicon have long been well-characterized experimentally, but the details have previously eluded precise calculation by first-principles methods because of the large extent of the wavefunction and the over-delocalization inherent in traditional exchange-correlation functionals. We found a new technique to overcome both of these challenges, allowing unprecedented accuracy in the prediction of the properties of shallow donors. Future work may extend the hybrid functional calculations to larger cell sizes or expand this technique to a wide variety of dopants and host materials. We also calculated the linear shift of the hyperfine parameter of these shallow donors with the hydrostatic component of strain, providing theoretical background for the use of strain to fine-tune atomic clock transitions. Our results help develop the understanding necessary to build spin qubits based on shallow donors in silicon.

We moved from silicon to complex oxides, exciting materials that are being considered for next-generation electronics. Many complex oxides show a regime in which resistivity scales with the square of the temperature, which is often attributed to electron-electron scattering. We explored the conditions under which electron-electron scattering may be expected to give rise to such a power law, providing guidance to experimental groups seeking to identify the source of signatures observed in transport experiments. The results also prevent the mis-identification of a T^2 power law in $SrTiO_3$ as arising from electron-electron scattering; recent unpublished work by Edelman and Littlewood has suggested a polaron-mediated mechanism for this transport signature. We have also opened the way for the direct calculation of electron-electron scattering rates in other materials using our methodology.

Turning to more exotic electronic behavior, we explored $Sr_3Ir_2O_7$, an excellent platform for studying the interactions between spin-orbit coupling and Coulomb correlations. This is a rapidly growing area of research, relevant to the study of topological phases and high-T_c superconductivity. In our work, we established that DFT+U captures both the electronic transition and the concomitant magnetic transition. This limits the types of mechanisms which may be at play in this transition, and suggests that magnetism is an important factor in the transition. The fact that the calculated phase transition is not accompanied by the charge-density-wave-like structural distortion also limits the types of mechanisms which may be at play in the transition. In particular, our results rule out a joint cause for the distortion and the phase transition. These results will guide future theoretical attempts to explain the transition and experimental attempts to probe it. In addition, joint experimental and theoretical work investigating the topotactic transformation of this material into the band insulator $Sr_3Ir_2O_7F_2$ is ongoing.

Finally, turning from electron conduction to proton conduction, we applied our first-principles methodology to barium cerate and strontium cerate. We showed that cation

vacancies act as hydrogen traps and may limit proton conductivity. This provides an explanation for the efficacy of acceptor-type dopants, which lower the Fermi level and reduce the concentration of cation vacancies, and opens the way for experiments in which optimizing doping or growth conditions to minimize these vacancies may improve proton conductivity. We also identified the position of the bands on an absolute energy scale, providing data for possible water-splitting experiments in the future. We predicted that electrons will self-trap as polarons in this material; a wide variety of experimental probes, including further luminescence experiments, could be brought to bear to verify and characterize these polarons.

In conclusion, we have used first-principles computational methods to tackle fundamental questions about materials, providing answers with practical impacts in novel computation and energy applications.

Appendix A

Electron-Electron Scattering Notes

The notes in this section are written by J. T. Devreese and S. N. Klimin and are reproduced by permission.

On the resistivity and relaxation rate of Nb-doped strontium titanate provided by the Baber scattering (explanatory note)

J. T. Devreese, S. N. Klimin

(Dated: May 19, 2016)

In the present note, the derivation of the "Baber contribution" to the relaxation rate is described. Within the Baber mechanism, the DC conductivity is provided by the interaction between the charge carriers with different band masses (or between electrons and holes, as in the original paper [1, 2]). When the carriers with different masses are present in a crystal, the *normal* electron-electron scattering processes (i. e., the scattering processes without *umklapp*) can bring a nonzero contribution to the relaxation rate and to the DC conductivity.

The calculation is performed using the Boltzmann equation and following Ref. [3] (Chapters 7 to 9). Within this approach, the non-equilibrium distribution function $f_{n,\mathbf{k}}$ for the carriers is the n-th subband determined as

$$f_{n,\mathbf{k}} = f^{(0)}_{n,\mathbf{k}} - \Phi_{n,\mathbf{k}} \frac{\partial f^{(0)}_{n,\mathbf{k}}}{\partial \varepsilon_{n,\mathbf{k}}}, \tag{1}$$

where $f^{(0)}_{n,\mathbf{k}} \equiv f\left(\varepsilon_{n,\mathbf{k}}\right)$ is the equilibrium (Fermi) distribution. The function $\Phi_{n,\mathbf{k}}$ is a measure of the deviation from equilibrium in the electron distribution. We use here the notations from Ref. [3]. The inner product of two functions Ψ and Φ is defined by

$$\langle \Psi, \Phi \rangle \equiv \int d\mathbf{k}\ \Psi\left(\mathbf{k}\right) \Phi\left(\mathbf{k}\right). \tag{2}$$

As established in Ref. [3], from a mathematical point of view, the collision integral of the Boltzmann equation can be represented even as $\langle \Phi, P\Phi \rangle$ where P is a scattering operator which transforms the function Φ into another function $\Psi = P\Phi$. In the notations by Ziman, the DC resistivity is expressed as

$$\rho = \frac{\langle \Phi, P\Phi \rangle}{\left[\langle \Phi, X\left(E=1\right) \rangle\right]^2}, \tag{3}$$

where $X\left(E=1\right)$ represents the left-hand side of the Boltzmann equation in a unit electric field,

$$\langle \Phi, X\left(E=1\right) \rangle = 2 \sum_n \int e \mathbf{v}_{n,\mathbf{k}} \Phi_{n,\mathbf{k}} \frac{\partial f\left(\varepsilon_{n,\mathbf{k}}\right)}{\partial \varepsilon_{n,\mathbf{k}}} \frac{d\mathbf{k}}{\left(2\pi\right)^3}.$$

Here, $\mathbf{v}_{n,\mathbf{k}}$ is the velocity in the n-th subband,

$$\mathbf{v}_{n,\mathbf{k}} = \frac{1}{\hbar}\frac{\partial \varepsilon_{n,\mathbf{k}}}{\partial \mathbf{k}}.$$

In Ref. [3], the collision integral for the electron-electron scattering processes is determined as

$$\begin{aligned}\langle \Phi, P\Phi \rangle = \frac{1}{2k_BT}\sum_{n,n'}\int \frac{d\mathbf{k}_1}{(2\pi)^3}\frac{d\mathbf{k}_2}{(2\pi)^3}\frac{d\mathbf{k}_3}{(2\pi)^3}\frac{d\mathbf{k}_4}{(2\pi)^3}\left(\Phi_{n,1}+\Phi_{n',2}-\Phi_{n,3}-\Phi_{n',4}\right)^2 \\ \times \mathcal{P}\left(n,1,n',2\rightarrow n,3,n',4\right) \qquad (4)\end{aligned}$$

Here, $\mathcal{P}\left(n,1,n',2\rightarrow n,3,n',4\right)$ is the scattering probability,

$$\begin{aligned}\mathcal{P}\left(n,1,n',2\rightarrow n,3,n',4\right) = \left(U^{(eff)}_{\mathbf{k}_1,\mathbf{k}_3}\right)^2 f\left(\varepsilon_{n,\mathbf{k}_1}\right) f\left(\varepsilon_{n',\mathbf{k}_2}\right)\left[1-f\left(\varepsilon_{n,\mathbf{k}_3}\right)\right]\left[1-f\left(\varepsilon_{n',\mathbf{k}_4}\right)\right] \\ \times \frac{2\pi}{\hbar}\delta\left(\varepsilon_{n,\mathbf{k}_1}+\varepsilon_{n',\mathbf{k}_2}-\varepsilon_{n,\mathbf{k}_3}-\varepsilon_{n',\mathbf{k}_4}\right) \\ \times (2\pi)^3\,\delta\left(\mathbf{k}_1+\mathbf{k}_2-\mathbf{k}_3-\mathbf{k}_4\right)\end{aligned}$$

with the matrix element of the effective electron-electron interaction $U^{(eff)}_{\mathbf{k}_1,\mathbf{k}_3}$. In general, the effective electron-electron interaction includes both the Coulomb repulsion and the phonon-mediated attraction.

The function $\Phi_{n,\mathbf{k}}$ is a trial function for the variational principle from Ref. [3]. In the theory of the electric resistivity [3], $\Phi_{n,\mathbf{k}}$ is chosen in the form

$$\Phi_{n,\mathbf{k}} = \mathbf{v}_{n,\mathbf{k}} \cdot \mathbf{u}$$

where $\mathbf{u}$ is the unit vector parallel to the applied dielectric field. Thus the collision integral is

$$\begin{aligned}\langle \Phi, P\Phi \rangle = \frac{1}{2k_BT}\frac{1}{(2\pi)^9}\frac{2\pi}{\hbar}\sum_{n,n'}\int d\mathbf{k}_1 d\mathbf{k}_2 d\mathbf{k}_3 d\mathbf{k}_4 \left(\left(\mathbf{v}_{n,\mathbf{k}_1}+\mathbf{v}_{n',\mathbf{k}_2}-\mathbf{v}_{n,\mathbf{k}_3}-\mathbf{v}_{n',\mathbf{k}_4}\right)\cdot\mathbf{u}\right)^2 \\ \times \left(U^{(eff)}_{\mathbf{k}_1,\mathbf{k}_3}\right)^2 f\left(\varepsilon_{n,\mathbf{k}_1}\right) f\left(\varepsilon_{n',\mathbf{k}_2}\right)\left[1-f\left(\varepsilon_{n,\mathbf{k}_3}\right)\right]\left[1-f\left(\varepsilon_{n',\mathbf{k}_4}\right)\right] \\ \times \delta\left(\varepsilon_{n,\mathbf{k}_1}+\varepsilon_{n',\mathbf{k}_2}-\varepsilon_{n,\mathbf{k}_3}-\varepsilon_{n',\mathbf{k}_4}\right)\delta\left(\mathbf{k}_1+\mathbf{k}_2-\mathbf{k}_3-\mathbf{k}_4\right) \qquad (5)\end{aligned}$$

The electrons in the conduction band are described by the matrix Hamiltonian from Ref. [4]

$$H = 4\begin{pmatrix}\varepsilon_1(\mathbf{k}) & 0 & 0 \\ 0 & \varepsilon_2(\mathbf{k}) & 0 \\ 0 & 0 & \varepsilon_3(\mathbf{k})\end{pmatrix} + \frac{1}{2}W, \qquad (6)$$

with the energies

$$\varepsilon_1 = t_\delta \sin^2\left(\frac{a_0 k_x}{2}\right) + t_\pi \sin^2\left(\frac{a_0 k_y}{2}\right) + t_\pi \sin^2\left(\frac{a_0 k_z}{2}\right),$$
$$\varepsilon_2 = t_\pi \sin^2\left(\frac{a_0 k_x}{2}\right) + t_\delta \sin^2\left(\frac{a_0 k_y}{2}\right) + t_\pi \sin^2\left(\frac{a_0 k_z}{2}\right),$$
$$\varepsilon_3 = t_\pi \sin^2\left(\frac{a_0 k_x}{2}\right) + t_\pi \sin^2\left(\frac{a_0 k_y}{2}\right) + t_\delta \sin^2\left(\frac{a_0 k_z}{2}\right), \tag{7}$$

where a_0 is the lattice constant. The matrix W

$$W = \begin{pmatrix} 2D & \xi & \xi \\ \xi & 2D & \xi \\ \xi & \xi & -4D \end{pmatrix} \tag{8}$$

describes the mixing of subbands within the conductivity band.

In the present note, we neglect the band mixing and assume the anisotropic parabolic dispersion in each of three subbands of the conductivity band (as in Refs. [4, 5]) with the tensor effective masses $\left|m_{jj}^{(n)}\right|$ $(j = x, y, z,\ n = 1, 2, 3)$. The masses $m_{jj}^{(n)}$ can take two values: the "light" mass $m_\pi = \hbar^2/\left(2a_0^2 t_\pi\right)$ and the "heavy" mass $m_\delta = \hbar^2/\left(2a_0^2 t_\delta\right)$. In addition, it is assumed that the temperature is sufficiently low so that the chemical potential of the carriers μ is relatively close to their Fermi energy E_F. In this approximation, both the collision integral and the normalization factor the resistivity are substantially simplified. The normalization factor becomes

$$\left[\langle \Phi, X\left(E = 1\right)\rangle\right]^2 = e^2 \frac{8}{9\pi^4} \frac{\mu^3}{\hbar^6} \frac{\left(2m_\delta + m_\pi\right)^2}{m_\delta}. \tag{9}$$

Using the definitions of the average inverse band mass m_b and the density-of-state band mass m_D,

$$\frac{1}{m_b} = \frac{1}{3}\left(\frac{2}{m_\pi} + \frac{1}{m_\delta}\right),\ m_D = \left(m_\pi^2 m_\delta\right)^{1/3} \tag{10}$$

the normalization factor takes the form

$$\left[\langle \Phi, X\left(E = 1\right)\rangle\right]^2 = e^2 \frac{8}{\pi^4} \frac{\mu^3}{\hbar^6} \frac{m_D^3}{m_b^2}. \tag{11}$$

In the same approximation, the collision integral is

$$\begin{aligned} \langle \Phi, P\Phi\rangle = {} & \frac{1}{2k_B T} \frac{1}{(2\pi)^9} \frac{2\pi}{\hbar} \sum_{n,n'} \int d\mathbf{k}_1 d\mathbf{k}_2 d\mathbf{k}_3 d\mathbf{k}_4 \left(v_{n,z,\mathbf{k}_1} - v_{n,z,\mathbf{k}_3} + v_{n',z,\mathbf{k}_2} - v_{n',z,\mathbf{k}_4}\right)^2 \\ & \times \left(U_{\mathbf{k}_1,\mathbf{k}_3}^{(eff)}\right)^2 f\left(\varepsilon_{n,\mathbf{k}_1}\right) f\left(\varepsilon_{n',\mathbf{k}_2}\right) \left[1 - f\left(\varepsilon_{n,\mathbf{k}_3}\right)\right] \left[1 - f\left(\varepsilon_{n',\mathbf{k}_4}\right)\right] \\ & \times \delta\left(\varepsilon_{n,\mathbf{k}_1} + \varepsilon_{n',\mathbf{k}_2} - \varepsilon_{n,\mathbf{k}_3} - \varepsilon_{n',\mathbf{k}_4}\right) \delta\left(\mathbf{k}_1 - \mathbf{k}_3 + \mathbf{k}_2 - \mathbf{k}_4\right). \end{aligned} \tag{12}$$

Here, the factor $\left(v_{n,z,\mathbf{k}_1} - v_{n,z,\mathbf{k}_3} + v_{n',z,\mathbf{k}_2} - v_{n',z,\mathbf{k}_4}\right)^2$ is other than zero when $n \neq n'$

$$\left(v_{n,z,\mathbf{k}_1} - v_{n,z,\mathbf{k}_3} + v_{n',z,\mathbf{k}_2} - v_{n',z,\mathbf{k}_4}\right)^2 = \hbar^2 \left(\frac{1}{m_{zz}^{(n)}} - \frac{1}{m_{zz}^{(n')}}\right)^2 \left(k_{1,z} - k_{3,z}\right)^2. \tag{13}$$

Thus the Baber scattering is realized here through the interaction of the electrons in different subbands. The collision integral is then

$$\begin{aligned}\langle \Phi, P\Phi \rangle = \frac{1}{2k_BT} \frac{1}{(2\pi)^9} \frac{2\pi}{\hbar} \hbar^2 \sum_{n,n'} \left(\frac{1}{m_{zz}^{(n)}} - \frac{1}{m_{zz}^{(n')}}\right)^2 \int d\mathbf{k}_1 d\mathbf{k}_2 d\mathbf{k}_3 d\mathbf{k}_4 \left(k_{1,z} - k_{3,z}\right)^2 \\ \times \left(U_{\mathbf{k}_1,\mathbf{k}_3}^{(eff)}\right)^2 f\left(\varepsilon_{n,\mathbf{k}_1}\right) f\left(\varepsilon_{n',\mathbf{k}_2}\right) \left[1 - f\left(\varepsilon_{n,\mathbf{k}_3}\right)\right] \left[1 - f\left(\varepsilon_{n',\mathbf{k}_4}\right)\right] \\ \times \delta\left(\varepsilon_{n,\mathbf{k}_1} + \varepsilon_{n',\mathbf{k}_2} - \varepsilon_{n,\mathbf{k}_3} - \varepsilon_{n',\mathbf{k}_4}\right) \delta\left(\mathbf{k}_1 - \mathbf{k}_3 + \mathbf{k}_2 - \mathbf{k}_4\right). \end{aligned} \tag{14}$$

Let us perform the replacement of variables [separately for each term with a given (n, n')]:

$$\begin{aligned} k_{1,x} \equiv \frac{1}{\hbar}\sqrt{m_{xx}^{(n)}} p_{1,x},\ k_{1,y} \equiv \frac{1}{\hbar}\sqrt{m_{yy}^{(n)}} p_{1,y},\ k_{1,z} \equiv \frac{1}{\hbar}\sqrt{m_{zz}^{(n)}} p_{1,z}, \\ k_{3,x} \equiv \frac{1}{\hbar}\sqrt{m_{xx}^{(n)}} p_{3,x},\ k_{3,y} \equiv \frac{1}{\hbar}\sqrt{m_{yy}^{(n)}} p_{3,y},\ k_{3,z} \equiv \frac{1}{\hbar}\sqrt{m_{zz}^{(n)}} p_{3,z}, \\ k_{2,x} \equiv \frac{1}{\hbar}\sqrt{m_{xx}^{(n')}} p_{2,x},\ k_{2,y} \equiv \frac{1}{\hbar}\sqrt{m_{yy}^{(n')}} p_{2,y},\ k_{2,z} \equiv \frac{1}{\hbar}\sqrt{m_{zz}^{(n')}} p_{2,z}, \\ k_{4,x} \equiv \frac{1}{\hbar}\sqrt{m_{xx}^{(n')}} p_{4,x},\ k_{4,y} \equiv \frac{1}{\hbar}\sqrt{m_{yy}^{(n')}} p_{4,y},\ k_{4,z} \equiv \frac{1}{\hbar}\sqrt{m_{zz}^{(n')}} p_{4,z}. \end{aligned}$$

After this replacement, we find that

$$\varepsilon_{n,\mathbf{k}} = \frac{1}{2}\left(p_x^2 + p_y^2 + p_z^2\right) = \frac{p^2}{2},$$

and

$$\int d\mathbf{k}_j \ldots = \frac{m_D^{3/2}}{\hbar^3} \int d\mathbf{p}_j \ldots \qquad (j = 1, \ldots, 4).$$

In these variables, the collision integral takes the form

$$\begin{aligned}\langle \Phi, P\Phi \rangle = \frac{1}{k_BT} \frac{1}{(2\pi)^8} \frac{m_D^6}{2\hbar^{13}} \sum_{n,n'} \left(\frac{1}{m_{zz}^{(n)}} - \frac{1}{m_{zz}^{(n')}}\right)^2 m_{zz}^{(n)} \int d\mathbf{p}_1 d\mathbf{p}_2 d\mathbf{p}_3 d\mathbf{p}_4 \left(k_{1,z} - k_{3,z}\right)^2 \\ \times \left(U_{\mathbf{k}_1,\mathbf{k}_3}^{(eff)}\right)^2 f\left(\varepsilon_{n,\mathbf{k}_1}\right) f\left(\varepsilon_{n',\mathbf{k}_2}\right) \left[1 - f\left(\varepsilon_{n,\mathbf{k}_3}\right)\right] \left[1 - f\left(\varepsilon_{n',\mathbf{k}_4}\right)\right] \\ \times \delta\left(\varepsilon_{n,\mathbf{k}_1} + \varepsilon_{n',\mathbf{k}_2} - \varepsilon_{n,\mathbf{k}_3} - \varepsilon_{n',\mathbf{k}_4}\right) \delta\left(\mathbf{k}_1 - \mathbf{k}_3 + \mathbf{k}_2 - \mathbf{k}_4\right). \end{aligned} \tag{15}$$

The integrals are further calculated in the spherical coordinates,

$$d\mathbf{p}_j = p_j^2 dp_j d\Omega_j, \qquad d\Omega_j = \sin\theta_j d\theta_j d\varphi_j.$$

what gives us the result

$$\begin{aligned}\langle \Phi, P\Phi \rangle = \frac{1}{2k_BT}\frac{1}{(2\pi)^9}\frac{2\pi}{\hbar}\hbar^2\frac{m_D^6}{\hbar^{14}}\sum_{n,n'}\left(\frac{1}{m_{zz}^{(n)}}-\frac{1}{m_{zz}^{(n')}}\right)^2 m_{zz}^{(n)}\int d\Omega_1\int d\Omega_2\int d\Omega_3\int d\Omega_4 \\ \int\sqrt{2\varepsilon_1}d\varepsilon_1\int\sqrt{2\varepsilon_2}d\varepsilon_2\int\sqrt{2\varepsilon_3}d\varepsilon_3\int\sqrt{2\varepsilon_4}d\varepsilon_4 \\ \times f(\varepsilon_1)f(\varepsilon_2)[1-f(\varepsilon_3)][1-f(\varepsilon_4)]\delta(\varepsilon_1+\varepsilon_2-\varepsilon_3-\varepsilon_4) \\ \times\left(U_{\mathbf{k}_1,\mathbf{k}_3}^{(eff)}\right)^2(p_1\cos\theta_1-p_3\cos\theta_3)^2\delta(\mathbf{k}_1-\mathbf{k}_3+\mathbf{k}_2-\mathbf{k}_4). \end{aligned} \tag{16}$$

The next approximation is the same as in Chap.9 of Ref. [3]. Under the condition

$$\varepsilon_1+\varepsilon_2-\varepsilon_3-\varepsilon_4=0$$

provided by the delta function $\delta(\varepsilon_1+\varepsilon_2-\varepsilon_3-\varepsilon_4)$, the product of the functions

$$f(\varepsilon_1)f(\varepsilon_2)[1-f(\varepsilon_3)][1-f(\varepsilon_4)] \tag{17}$$

is not negligibly small only inside the thermal layer of the width $\delta\varepsilon\sim k_BT$ near the Fermi surface. Therefore the other functions can be assumed slowly varying with respect to (17) and replaced by their values at the Fermi surface. In particular, we set $p_j\approx\sqrt{2\mu}\equiv p_\mu$.

The argument of the delta function $\delta(\mathbf{k}_1-\mathbf{k}_3+\mathbf{k}_2-\mathbf{k}_4)$ is (by components)

$$k_{1,j}-k_{3,j}+k_{2,j}-k_{4,j}=\frac{1}{\hbar}\sqrt{m_{jj}^{(n)}}(p_{1,j}-p_{3,j})+\frac{1}{\hbar}\sqrt{m_{jj}^{(n')}}(p_{2,j}-p_{4,j})$$

Herefrom we find that

$$\begin{aligned}&\delta(\mathbf{k}_1-\mathbf{k}_3+\mathbf{k}_2-\mathbf{k}_4) \\ &=\frac{\hbar^3}{\prod\limits_{j=x,y,z}\sqrt{m_{jj}^{(n')}}}\prod_{j=x,y,z}\delta\left((p_{2,j}-p_{4,j})+\sqrt{\frac{m_{jj}^{(n)}}{m_{jj}^{(n')}}}(p_{1,j}-p_{3,j})\right) \\ &=\frac{\hbar^3}{m_D^{3/2}}\prod_{j=x,y,z}\delta\left(p_{2,j}-p_{4,j}+\sqrt{\frac{m_{jj}^{(n)}}{m_{jj}^{(n')}}}(p_{1,j}-p_{3,j})\right).\end{aligned}$$

Therefore the vector $\mathbf{Q}_{n,n'}$ can be introduced, with the components

$$\left(\mathbf{Q}_{n,n'}\right)_j\equiv\sqrt{\frac{m_{jj}^{(n)}}{m_{jj}^{(n')}}}(p_{1,j}-p_{3,j}), \tag{18}$$

and the delta function is expressed as

$$\delta\left(\mathbf{k}_1-\mathbf{k}_3+\mathbf{k}_2-\mathbf{k}_4\right)=\frac{\hbar^3}{m_D^{3/2}}\delta\left(\mathbf{p}_2-\mathbf{p}_4+\mathbf{Q}_{n,n'}\right).$$

The integrals over the energies with the distribution functions

$$f\left(\varepsilon\right)=\frac{1}{e^{(\varepsilon-\mu)/(k_BT)}+1}.$$

are calculated analytically using the change of the variables

$$\varepsilon_4=\varepsilon_1+\Delta,\ \varepsilon_3=\varepsilon_2+\Delta'.$$

The Jacobian of this transformation is equal to 1:

$$\left|\frac{\partial\left(\varepsilon_1,\varepsilon_2,\varepsilon_3,\varepsilon_4\right)}{\partial\left(\varepsilon_1,\varepsilon_2,\Delta,\Delta'\right)}\right|=1.$$

Using the variables

$$\frac{\varepsilon-\mu}{k_BT}=x,\qquad\frac{\Delta}{k_BT}=z$$

we find that

$$\int_0^\infty d\varepsilon_1 f\left(\varepsilon_1\right)\left[1-f\left(\varepsilon_1+\Delta\right)\right]=k_BT\frac{z}{1-e^{-z}},$$
$$\int_0^\infty d\varepsilon_2 f\left(\varepsilon_2\right)\left[1-f\left(\varepsilon_2-\Delta\right)\right]=k_BT\frac{ze^{-z}}{1-e^{-z}}.$$

The integral over the energies gives the result

$$\int_{-\infty}^\infty d\Delta\int_0^\infty d\varepsilon_1 f\left(\varepsilon_1\right)\left[1-f\left(\varepsilon_1+\Delta\right)\right]\int_0^\infty d\varepsilon_2 f\left(\varepsilon_2\right)\left[1-f\left(\varepsilon_2-\Delta\right)\right]$$
$$=\left(k_BT\right)^3\int_{-\infty}^\infty z^2\frac{e^{-z}}{\left(1-e^{-z}\right)^2}dz=\frac{2\pi^2}{3}\left(k_BT\right)^3.$$

Using this result, we find that $\langle\Phi,P\Phi\rangle$ is explicitly proportional to T^2:

$$\langle\Phi,P\Phi\rangle=\left(k_BT\right)^2\frac{1}{12\hbar^{10}}\left(\frac{m_D^{3/2}}{4\pi^2}\right)^3\sum_{n,n'}\left(\frac{1}{m_{zz}^{(n)}}-\frac{1}{m_{zz}^{(n')}}\right)^2 m_{zz}^{(n)}p_\mu^6$$
$$\times\int d\Omega_1\int d\Omega_3\left(U_{\mathbf{k}_1,\mathbf{k}_3}^{(eff)}\right)^2\left(\cos\theta_1-\cos\theta_3\right)^2$$
$$\times\int d\Omega_2\int d\Omega_4\delta\left(\mathbf{p}_2-\mathbf{p}_4+\mathbf{Q}_{n,n'}\right). \tag{19}$$

The integral $\int d\Omega_2\int d\Omega_4\delta\left(\mathbf{p}_2-\mathbf{p}_4+\mathbf{Q}_{n,n'}\right)$ is calculated analytically (similar calculations can be found in Ref. [3]). Let us introduce the momentum $\mathbf{P}=\mathbf{p}_2-\mathbf{p}_4$. Its modulus is

$$P^2=\left|\mathbf{p}_2-\mathbf{p}_4\right|^2=p_2^2+p_4^2-2p_2p_4\cos\Theta, \tag{20}$$

where Θ is the angle between p_2 and p_4 Therefore, at fixed p_2, p_4

$$2PdP = 2p_2p_4 \sin\Theta d\Theta,$$

and hence

$$\sin\Theta d\Theta = \frac{P}{p_2p_4}dP. \tag{21}$$

The modulus P varies between the bounds

$$P_{\min} = |p_2 - p_4|, \quad P_{\max} = p_2 + p_4.$$

The element $d\Omega_4$ of the angular integration (choosing the z axis parallel to p_2) can be written as

$$d\Omega_4 = 2\pi \sin\Theta d\Theta.$$

Therefore, using (21), we find that:

$$d\Omega_4 = 2\pi \frac{P}{p_2p_4}dP$$

The differential element of the three-dimensional space $d\mathbf{P}$ is:

$$d\mathbf{P} = P^2 dP d\Omega_P = P^2 dP d\Omega_2.$$

Hence, the product $dPd\Omega_2$ is expressed as:

$$dPd\Omega_2 = \frac{1}{P^2}d\mathbf{P}.$$

Using these formulae, we represent the angular integral $\int d\Omega_2 d\Omega_4 \ldots$ in the form

$$\begin{aligned}\int d\Omega_2 d\Omega_4 \ldots &= 2\pi \int_{P_{\min}}^{P_{\max}} \frac{P}{p_2p_4}dP \int d\Omega_2 \ldots \\ &= 2\pi \int\limits_{P_{\min}<P<P_{\max}} \frac{P}{p_2p_4}\frac{1}{P^2}d\mathbf{P}\ldots = \frac{2\pi}{p_2p_4}\int\limits_{P_{\min}<P<P_{\max}} \frac{1}{P}d\mathbf{P}\ldots \end{aligned} \tag{22}$$

Consequently the integral with the δ-function $\delta(\mathbf{Q}_{n,n'} + \mathbf{p}_2 - \mathbf{p}_4)$ is explicitly calculated:

$$\begin{aligned}&\int d\Omega_2 \int d\Omega_4 \delta(\mathbf{Q}_{n,n'} + \mathbf{p}_2 - \mathbf{p}_4) \\ &= \int d\Omega_2 \int d\Omega_4 \delta(\mathbf{P} + \mathbf{Q}_{n,n'}) \\ &= \frac{2\pi}{p_2p_4}\int\limits_{P_{\min}<P<P_{\max}} \frac{1}{P}\delta(\mathbf{P} + \mathbf{Q}_{n,n'})\, d\mathbf{P} \\ &= \frac{2\pi}{p_2p_4}\frac{1}{|\mathbf{Q}_{n,n'}|}\Theta(P_{\min} < |\mathbf{Q}_{n,n'}| < P_{\max}) \\ &\approx \frac{2\pi}{p_\mu^2}\frac{1}{|\mathbf{Q}_{n,n'}|}\Theta(2p_\mu - |\mathbf{Q}_{n,n'}|),\end{aligned}$$

where $\Theta\left(2p_\mu - |\mathbf{Q}_{n,n'}|\right)$ is the unit step function. Substituting these results to (19) and using the normalization factor (11) we arrive at the resistivity

$$\begin{aligned}\rho = (k_B T)^2 \frac{\pi}{192} \frac{1}{(4\pi)^2 e^2} \frac{m_D^{3/2} m_b^2}{\hbar^4 \mu^3} \sum_{n,n'} \left(\frac{1}{m_{zz}^{(n)}} - \frac{1}{m_{zz}^{(n')}} \right)^2 m_{zz}^{(n)} p_\mu^4 \\ \times \int_0^\pi \sin\theta_1 d\theta_1 \int_0^\pi \sin\theta_3 d\theta_3 \int_0^{2\pi} d\varphi_1 \int_0^{2\pi} d\varphi_3 \left(U_{\mathbf{k}_1,\mathbf{k}_3}^{(eff)} \right)^2 \\ \times \frac{\left(\cos\theta_1 - \cos\theta_3\right)^2}{|\mathbf{Q}_{n,n'}|} \Theta\left(2p_\mu - |\mathbf{Q}_{n,n'}|\right) \end{aligned} \tag{23}$$

with

$$\begin{aligned}|\mathbf{k}_1 - \mathbf{k}_3|^2 = \frac{p_\mu^2}{\hbar^2} \left[m_{xx}^{(n)} \left(\sin\theta_1 \cos\varphi_1 - \sin\theta_3 \cos\varphi_3\right)^2 \right. \\ \left. + m_{yy}^{(n)} \left(\sin\theta_1 \sin\varphi_1 - \sin\theta_3 \sin\varphi_3\right)^2 + m_{zz}^{(n)} \left(\cos\theta_1 - \cos\theta_3\right)^2 \right] \end{aligned}$$

and

$$\begin{aligned}|\mathbf{Q}_{n,n'}| = p_\mu \left[\frac{m_{xx}^{(n)}}{m_{xx}^{(n')}} \left(\sin\theta_1 \cos\varphi_1 - \sin\theta_3 \cos\varphi_3\right)^2 \right. \\ \left. + \frac{m_{yy}^{(n)}}{m_{yy}^{(n')}} \left(\sin\theta_1 \sin\varphi_1 - \sin\theta_3 \sin\varphi_3\right)^2 + \frac{m_{zz}^{(n)}}{m_{zz}^{(n')}} \left(\cos\theta_1 - \cos\theta_3\right)^2 \right]^{1/2}. \end{aligned} \tag{24}$$

The relaxation rate $1/\tau$ and the resistivity are proportional to each other as

$$\frac{1}{\tau} = \frac{\omega_p^2}{4\pi} \rho, \tag{25}$$

where $\omega_p = \sqrt{\frac{4\pi e^2 n_0}{m_b}}$ is the plasma frequency for the electron gas in the conductivity band. Thus we obtain the resulting expression of the relaxation rate

$$\begin{aligned}\frac{1}{\tau} = (k_B T)^2 \frac{\pi}{192} \frac{n_0}{(4\pi)^2} \frac{m_D^{3/2} m_b}{\hbar^4 \mu^3} p_\mu^4 \sum_{n,n'} \left(\frac{1}{m_{zz}^{(n)}} - \frac{1}{m_{zz}^{(n')}} \right)^2 m_{zz}^{(n)} \\ \times \int_0^\pi \sin\theta_1 d\theta_1 \int_0^\pi \sin\theta_3 d\theta_3 \int_0^{2\pi} d\varphi_1 \int_0^{2\pi} d\varphi_3 \left(U_{\mathbf{k}_1,\mathbf{k}_3}^{(eff)} \right)^2 \\ \times \frac{\left(\cos\theta_1 - \cos\theta_3\right)^2}{|\mathbf{Q}_{n,n'}|} \Theta\left(2p_\mu - |\mathbf{Q}_{n,n'}|\right). \end{aligned} \tag{26}$$

The remaining four-fold integral over the angles is calculated numerically.

---

[1] W. G. Baber, Proc. R. Soc. A **158**, 383 (1937).

[2] T. Giamarchi and B. S. Shastry, Phys. Rev. B **46**, 5528 (1992).

[3] J. M. Ziman, *Electrons and Phonons* (Oxford U.P., Oxford, England, 1960).

[4] D. van der Marel, J. L. M. van Mechelen, and I. I. Mazin, Phys. Rev. B **84**, 205111 (2011).

[5] J. T. Devreese, S. N. Klimin, J. L. M. van Mechelen, and D. van der Marel, Phys. Rev. B **81**, 125119 (2010).

Bibliography

[1] M. W. Swift and C. G. Van de Walle, *Conditions for T^2 resistivity from electron-electron scattering*, *European Physical Journal B* **90** (2017) 151.

[2] M. Swift, A. Janotti and C. G. Van de Walle, *Small polarons and point defects in barium cerate*, *Phys. Rev. B* **92** (2015) 214114.

[3] M. Swift and C. G. Van de Walle, *Impact of Point Defects on Proton Conduction in Strontium Cerate*, *The Journal of Physical Chemistry C* **120** (2016) 9562–9568.

[4] P. Hohenberg and W. Kohn, *Inhomogeneous Electron Gas*, *Phys. Rev.* **136** (1964) B864–B871.

[5] J. P. Perdew, K. Burke and M. Ernzerhof, *Generalized Gradient Approximation Made Simple*, *Phys. Rev. Lett.* **77** (1996) 3865–3868.

[6] B. Himmetoglu, A. Floris, S. de Gironcoli and M. Cococcioni, *Hubbard-corrected DFT energy functionals: The LDA+U description of correlated systems*, *Int. J. of Quantum Chem* **114** (2014) 14–49.

[7] R. M. Martin, *Electronic Structure: Basic Theory and Practical Methods*. Cambridge University Press, Cambridge, 2004, doi:10.1017/cbo9780511805769.

[8] J. P. Perdew, M. Ernzerhof and K. Burke, *Rationale for mixing exact exchange with density functional approximations*, *J. Chem. Phys.* **105** (1996) 9982–9985.

[9] J. Heyd, G. E. Scuseria and M. Ernzerhof, *Hybrid functionals based on a screened Coulomb potential*, *J. Chem. Phys.* **118** (2003) 8207–8215.

[10] J. Paier, M. Marsman, K. Hummer, G. Kresse, I. C. Gerber and J. G. Angyan, *Erratum: Screened hybrid density functionals applied to solids [J. Chem. Phys.124, 154709 (2006)]*, *J. Chem. Phys.* **125** (2006) 249901.

[11] G. Kresse and J. Furthmüller, *Efficient iterative schemes for ab initio total-energy calculations using a plane-wave basis set*, *Phys. Rev. B* **54** (1996) 11169–11186.

[12] P. E. Blöchl, *Projector augmented-wave method*, *Phys. Rev. B* **50** (1994) 17953–17979.

[13] C. Freysoldt, B. Grabowski, T. Hickel, J. Neugebauer, G. Kresse, A. Janotti et al., *First-principles calculations for point defects in solids*, *Rev. Mod. Phys.* **86** (2014) 253–305.

[14] C. Freysoldt, J. Neugebauer and C. Van de Walle, *Fully Ab Initio Finite-Size Corrections for Charged-Defect Supercell Calculations*, *Phys. Rev. Lett.* **102** (2009) 016402.

[15] C. Freysoldt, J. Neugebauer and C. G. Van de Walle, *Electrostatic interactions between charged defects in supercells*, *Phys. Status Solidi B* **248** (2011) 1067–1076.

[16] J. M. Luttinger and W. Kohn, *Motion of Electrons and Holes in Perturbed Periodic Fields*, *Phys. Rev.* **97** (1955) 869–883.

[17] W. Kohn and J. M. Luttinger, *Theory of Donor States in Silicon*, *Phys. Rev.* **98** (1955) 915–922.

[18] W. Kohn, *Shallow Impurity States in Silicon and Germanium*, *Solid State Phys* **5** (1957) 257–320.

[19] M. Grundmann, *The Physics of Semiconductors*. Springer Science & Business Media, 11, 2010, doi:10.1007/978-3-319-23880-7.

[20] A. L. Saraiva, A. Baena, M. J. Calderón and B. Koiller, *Theory of one and two donors in silicon*, *J. Phys. Condens. Matter* **27** (2015) 154208.

[21] T. H. Ning and C. T. Sah, *Multivalley Effective-Mass Approximation for Donor States in Silicon. I. Shallow-Level Group-V Impurities*, *Phys. Rev. B* **4** (1971) 3468–3481.

[22] T. Yamamoto, T. Uda, T. Yamasaki and T. Ohno, *First-principles supercell calculations for simulating a shallow donor state in Si*, *Phys. Lett. A* **373** (2009) 3989–3993.

[23] C. J. Wellard and L. C. L. Hollenberg, *Donor electron wave functions for phosphorus in silicon: Beyond effective-mass theory*, *Phys. Rev. B* **72** (2005) 085202.

[24] A. Debernardi, A. Baldereschi and M. Fanciulli, *Computation of the Stark effect in P impurity states in silicon*, *Phys. Rev. B* **74** (2006) 035202.

[25] H. Nara and A. Morita, *Shallow Donor Potential in Silicon*, *J. Phys. Soc. Jpn* **21** (1966) 1852–1853.

[26] A. Baena, A. L. Saraiva, B. Koiller and M. J. Calderón, *Impact of the valley degree of freedom on the control of donor electrons near a Si/SiO_2 interface*, *Phys. Rev. B* **86** (2012) 035317.

[27] J. K. Gamble, N. T. Jacobson, E. Nielsen, A. D. Baczewski, J. E. Moussa, I. Montaño et al., *Multivalley effective mass theory simulation of donors in silicon*, *Phys. Rev. B* **91** (2015) 235318.

[28] A. S. Martins, T. B. Boykin, G. Klimeck and B. Koiller, *Conduction-band tight-binding description for Si applied to P donors*, *Phys. Rev. B* **72** (2005) 193204.

[29] B. Koiller, X. Hu and S. Das Sarma, *Strain effects on silicon donor exchange: Quantum computer architecture considerations*, *Phys. Rev. B* **66** (2002) 115201.

[30] E. C. Niculescu, *Dielectric mismatch and central-cell corrections in doped silicon nanodots*, *Eur. Phys. J. B* **79** (2011) 363–369.

[31] G. Pica, B. W. Lovett, R. N. Bhatt and S. A. Lyon, *Exchange coupling between silicon donors: The crucial role of the central cell and mass anisotropy*, *Phys. Rev. B* **89** (2014) 235306.

[32] G. Pica, G. Wolfowicz, M. Urdampilleta, M. L. W. Thewalt, H. Riemann, N. V. Abrosimov et al., *Hyperfine Stark effect of shallow donors in silicon*, *Phys. Rev. B* **90** (2014) 195204.

[33] M. Usman, R. Rahman, J. Salfi, J. Bocquel, B. Voisin, S. Rogge et al., *Donor hyperfine Stark shift and the role of central-cell corrections in tight-binding theory*, *J. Phys. Condens. Matter* **27** (2015) 154207.

[34] C. G. Van de Walle, *Structural identification of hydrogen and muonium centers in silicon: First-principles calculations of hyperfine parameters*, *Phys. Rev. Lett.* **64** (1990) 669–672.

[35] H. Overhof and U. Gerstmann, *Ab Initio Calculation of Hyperfine and Superhyperfine Interactions for Shallow Donors in Semiconductors*, *Phys. Rev. Lett.* **92** (2004) 087602.

[36] H. Huebl, A. R. Stegner, M. Stutzmann, M. S. Brandt, G. Vogg, F. Bensch et al., *Phosphorus Donors in Highly Strained Silicon*, *Phys. Rev. Lett.* **97** (2006) 166402.

[37] J. M. Ziman, *Electrons and Phonons*. Oxford University Press, Oxford, 1960.

[38] S. N. Klimin, J. Tempere, D. van der Marel and J. T. Devreese, *Microscopic mechanisms for the Fermi-liquid behavior of Nb-doped strontium titanate*, *Phys. Rev. B* **86** (2012) 045113.

[39] H. K. Pal, V. I. Yudson and D. L. Maslov, *Resistivity of non-Galilean-invariant Fermi- and non-Fermi liquids*, *Lith. J. Phys.* **52** (2012) 142–164.

[40] N. W. Ashcroft and N. D. Mermin, *Solid State Physics*. Brooks/Cole, Bellmont, CA, 1976.

[41] T. Hahn, *Cubaa library for multidimensional numerical integration*, *Computer Physics Communications* **168** (2005) 78 – 95.

[42] W. Kohn and J. M. Luttinger, *Hyperfine Splitting of Donor States in Silicon*, *Phys. Rev.* **97** (1955) 883–888.

[43] G. Wolfowicz, A. M. Tyryshkin, R. E. George, H. Riemann, N. V. Abrosimov, P. Becker et al., *Atomic clock transitions in silicon-based spin qubits*, *Nature Nanotechnology* **8** (2013) 881.

[44] K. Saeedi, M. Szech, P. Dluhy, J. Z. Salvail, K. J. Morse, H. Riemann et al., *Optical pumping and readout of bismuth hyperfine states in silicon for atomic clock applications*, *Scientific Reports* **5** (2015) 10493.

[45] J. J. Pla, A. Bienfait, G. Pica, J. Mansir, F. A. Mohiyaddin, A. Morello et al., *Strain-induced nuclear quadrupole splittings in silicon devices*, arXiv:1608.07346v1 [cond-mat.mes-hall].

[46] D. K. Wilson and G. Feher, *Electron Spin Resonance Experiments on Donors in Silicon. III. Investigation of Excited States by the Application of Uniaxial Stress and Their Importance in Relaxation Processes*, *Phys. Rev.* **124** (1961) 1068–1083.

[47] H. M. Petrilli, P. E. Blöchl, P. Blaha and K. Schwarz, *Electric-field-gradient calculations using the projector augmented wave method*, *Phys. Rev. B* **57** (1998) 14690–14697.

[48] J. Mansir, P. Conti, Z. Zeng, J. J. Pla, P. Bertet, B. Sklenard et al., *Linear hyperfine tuning of donor spins in silicon using hydrostatic strain*, arXiv:1710.00723 [quant-ph].

[49] L.-W. Wang, *Density functional calculations of shallow acceptor levels in Si*, *J. Appl. Phys* **105** (2009) 123712.

[50] J. S. Smith, A. Budi, M. C. Per, N. Vogt, D. W. Drumm, L. C. L. Hollenberg et al., *Ab initio calculation of energy levels for phosphorus donors in silicon*, *Sci. Rep* **7** (2017) 6010.

[51] G. A. Samara, *Temperature and pressure dependences of the dielectric constants of semiconductors*, *Phys. Rev. B* **27** (1983) 3494–3505.

[52] J. C. Hensel, H. Hasegawa and M. Nakayama, *Cyclotron Resonance in Uniaxially Stressed Silicon. II. Nature of the Covalent Bond*, *Phys. Rev.* **138** (1965) A225–A238.

[53] H. J. McSkimin and P. Andreatch, Jr., *Elastic Moduli of Silicon vs Hydrostatic Pressure at 25.0C and 195.8C*, *J. Appl. Phys* **35** (1964) 2161–2165.

[54] C. G. Van de Walle and P. E. Blöchl, *First-principles calculations of hyperfine parameters*, *Phys. Rev. B* **47** (1993) 4244.

[55] P. E. Blöchl, *First-principles calculations of defects in oxygen-deficient silica exposed to hydrogen*, *Phys. Rev. B* **62** (2000) 6158–6179.

[56] F. A. Cotton, *Chemical Applications of Group Theory*. John Wiley & Sons, third ed., 1990.

[57] G. K. White and S. B. Woods, *Electrical and Thermal Resistivity of the Transition Elements at Low Temperatures*, *Phil. Trans. R. Soc. A* **251** (1959) 273–302.

[58] G. K. White and R. J. Tainsh, *Electron Scattering in Nickel at Low Temperatures*, *Phys. Rev. Lett.* **19** (1967) 165–166.

[59] A. C. Anderson, R. E. Peterson and J. E. Robichaux, *Thermal and Electrical Conductivity of Ag and Pt Below 1K*, *Phys. Rev. Lett.* **20** (1968) 459–461.

[60] J. Bass, W. P. Pratt and P. A. Schroeder, *The temperature-dependent electrical resistivities of the alkali metals*, *Rev. Mod. Phys.* **62** (1990) 645–744.

[61] H. van Kempen, J. S. Lass, J. H. J. M. Ribot and P. Wyder, *Low-Temperature Limit of the Temperature-Dependent Part of the Resistivity of Potassium*, *Phys. Rev. Lett.* **37** (1976) 1574–1577.

[62] B. Levy, M. Sinvani and A. J. Greenfield, *Sample Dependence of the Electron-Electron Contribution to the Electrical Resistivity of Sodium and Potassium*, *Phys. Rev. Lett.* **43** (1979) 1822–1825.

[63] W. G. Baber, *The Contribution to the Electrical Resistance of Metals from Collisions between Electrons*, *Proc. R. Soc. Lond. A* **158** (1937) 383–396.

[64] M. J. Rice, *Electron-Electron Scattering in Transition Metals*, *Phys. Rev. Lett.* **20** (1968) 1439–1441.

[65] W. E. Lawrence and J. W. Wilkins, *Electron-Electron Scattering in the Transport Coefficients of Simple Metals*, *Phys. Rev. B* **7** (1973) 2317–2332.

[66] A. H. MacDonald, R. Taylor and D. J. W. Geldart, *Umklapp electron-electron scattering and the low-temperature electrical resistivity of the alkali metals*, *Phys. Rev. B* **23** (1981) 2718–2730.

[67] D. van der Marel, J. L. M. van Mechelen and I. I. Mazin, *Common Fermi-liquid origin of T^2 resistivity and superconductivity in n-type $SrTiO_3$*, *Phys. Rev. B* **84** (2011) 205111.

[68] E. Mikheev, B. Himmetoglu, A. P. Kajdos, P. Moetakef, T. A. Cain, C. G. Van de Walle et al., *Limitations to the room temperature mobility of two- and three-dimensional electron liquids in $SrTiO_3$*, *Appl. Phys. Lett.* **106** (2015) 062102.

[69] X. Lin, B. Fauqué and K. Behnia, *Scalable T^2 resistivity in a small single-component Fermi surface*, *Science* **349** (2015) 945–948.

[70] E. Mikheev, S. Raghavan, J. Y. Zhang, P. B. Marshall, A. P. Kajdos, L. Balents et al., *Carrier density independent scattering rate in $SrTiO_3$-based electron liquids*, *Sci. Rep.* **6** (2016) 20865.

[71] J.-S. Zhou, J. B. Goodenough and B. Dabrowski, *Pressure-Induced Non-Fermi-Liquid Behavior of* $PrNiO_3$, *Phys. Rev. Lett.* **94** (2005) 226602.

[72] E. Mikheev, A. J. Hauser, B. Himmetoglu, N. E. Moreno, A. Janotti, C. G. Van de Walle et al., *Tuning bad metal and non-Fermi liquid behavior in a Mott material: Rare-earth nickelate thin films*, *Sci. Adv.* **1** (2015) e1500797.

[73] Y. Ando, Y. Kurita, S. Komiya, S. Ono and K. Segawa, *Evolution of the Hall Coefficient and the Peculiar Electronic Structure of the Cuprate Superconductors*, *Phys. Rev. Lett.* **92** (2004) 197001.

[74] N. Barišić, M. K. Chan, Y. Li, G. Yu, X. Zhao, M. Dressel et al., *Universal sheet resistance and revised phase diagram of the cuprate high-temperature superconductors*, *Proc. Natl. Acad. Sci.* **110** (2013) 12235–12240.

[75] D. L. Maslov and A. V. Chubukov, *Optical response of correlated electron systems.*, *Rep. Prog. Phys.* **80** (2017) 026503.

[76] T. Giamarchi and B. S. Shastry, *Baber scattering and resistivity of a two-dimensional two-band model*, *Phys. Rev. B* **46** (1992) 5528–5535.

[77] A. H. MacDonald, *Electron-Phonon Enhancement of Electron-Electron Scattering in Al*, *Phys. Rev. Lett.* **44** (1980) 489–493.

[78] A. Spinelli, M. A. Torija, C. Liu, C. Jan and C. Leighton, *Electronic transport in doped $SrTiO_3$: Conduction mechanisms and potential applications*, *Phys. Rev. B* **81** (2010) 155110.

[79] J. T. Devreese, S. N. Klimin, J. L. M. van Mechelen and D. van der Marel, *Many-body large polaron optical conductivity in $SrTi_{1-x}Nb_xO_3$*, *Phys. Rev. B* **81** (2010) 125119.

[80] B. Himmetoglu, A. Janotti, H. Peelaers, A. Alkauskas and C. G. Van de Walle, *First-principles study of the mobility of $SrTiO_3$*, *Phys. Rev. B* **90** (2014) 241204.

[81] A. Janotti, B. Jalan, S. Stemmer and C. G. Van de Walle, *Effects of doping on the lattice parameter of SrTiO3*, *Appl. Phys. Lett* **100** (2012) 262104.

[82] B. J. Kim, H. Jin, S. J. Moon, J.-Y. Kim, B.-G. Park, C. S. Leem et al., *Novel* $J_{\text{eff}} = 1/2$ *Mott State Induced by Relativistic Spin-Orbit Coupling in* Sr_2IrO_4, *Phys. Rev. Lett.* **101** (2008) 076402.

[83] S. J. Moon, H. Jin, K. W. Kim, W. S. Choi, Y. S. Lee, J. Yu et al., *Dimensionality-Controlled Insulator-Metal Transition and Correlated Metallic State in* 5*d Transition Metal Oxides* $Sr_{n+1}Ir_nO_{3n+1}$ *(*$n = 1$*, 2, and* ∞*)*, *Phys. Rev. Lett.* **101** (2008) 226402.

[84] R. Arita, J. Kuneš, A. V. Kozhevnikov, A. G. Eguiluz and M. Imada, *Ab initio Studies on the Interplay between Spin-Orbit Interaction and Coulomb Correlation in* Sr_2IrO_4 *and* Ba_2IrO_4, *Phys. Rev. Lett.* **108** (2012) 086403.

[85] F. Wang and T. Senthil, *Twisted Hubbard Model for* Sr_2IrO_4*: Magnetism and Possible High Temperature Superconductivity*, *Phys. Rev. Lett.* **106** (2011) 136402.

[86] Y. K. Kim, O. Krupin, J. D. Denlinger, A. Bostwick, E. Rotenberg, Q. Zhao et al., *Fermi arcs in a doped pseudospin-1/2 Heisenberg antiferromagnet*, *Science* **345** (2014) 187–190.

[87] A. de la Torre, S. McKeown Walker, F. Y. Bruno, S. Riccó, Z. Wang, I. Gutierrez Lezama et al., *Collapse of the Mott Gap and Emergence of a Nodal Liquid in Lightly Doped* Sr_2IrO_4, *Phys. Rev. Lett.* **115** (2015) 176402.

[88] Y. Cao, Q. Wang, J. A. Waugh, T. J. Reber, H. Li, X. Zhou et al., *Hallmarks of the Mott-metal crossover in the hole-doped pseudospin-1/2 Mott insulator Sr2IrO4*, .

[89] Y. J. Yan, M. Q. Ren, H. C. Xu, B. P. Xie, R. Tao, H. Y. Choi et al., *Electron-Doped* Sr_2IrO_4*: An Analogue of Hole-Doped Cuprate Superconductors Demonstrated by Scanning Tunneling Microscopy*, *Phys. Rev. X* **5** (2015) 041018.

[90] Y. K. Kim, N. H. Sung, J. D. Denlinger and B. J. Kim, *Observation of a d-wave gap in electron-doped Sr2IrO4*, *Nat Phys* **12** (2016) 37–41.

[91] C. Dhital, T. Hogan, W. Zhou, X. Chen, Z. Ren, M. Pokharel et al., *Carrier localization and electronic phase separation in a doped spin-orbit-driven Mott phase in Sr3(Ir1xRux)2O7*, *Nature Communications* **5** (2014) 3377.

[92] T. Hogan, L. Bjaalie, L. Zhao, C. Belvin, X. Wang, C. G. Van de Walle et al., *Structural investigation of the bilayer iridate* $Sr_3Ir_2O_7$, *Phys. Rev. B* **93** (2016) 134110.

[93] J. W. Kim, Y. Choi, J. Kim, J. F. Mitchell, G. Jackeli, M. Daghofer et al., *Dimensionality Driven Spin-Flop Transition in Layered Iridates*, *Phys. Rev. Lett.* **109** (2012) 037204.

[94] J. G. Vale, S. Boseggia, H. C. Walker, R. Springell, Z. Feng, E. C. Hunter et al., *Importance of XY anisotropy in* Sr_2IrO_4 *revealed by magnetic critical scattering experiments*, *Phys. Rev. B* **92** (2015) 020406.

[95] T. Hogan, Z. Yamani, D. Walkup, X. Chen, R. Dally, T. Z. Ward et al., *First-Order Melting of a Weak Spin-Orbit Mott Insulator into a Correlated Metal*, *Phys. Rev. Lett.* **114** (2015) 257203.

[96] D. Hsieh, F. Mahmood, D. H. Torchinsky, G. Cao and N. Gedik, *Observation of a metal-to-insulator transition with both Mott-Hubbard and Slater characteristics in* Sr_2IrO_4 *from time-resolved photocarrier dynamics*, *Phys. Rev. B* **86** (2012) 035128.

[97] Q. Wang, Y. Cao, J. A. Waugh, S. R. Park, T. F. Qi, O. B. Korneta et al., *Dimensionality-controlled Mott transition and correlation effects in single-layer and bilayer perovskite iridates*, *Phys. Rev. B* **87** (2013) 245109.

[98] H. Chu, L. Zhao, A. de la Torre, T. Hogan, S. D. Wilson and D. Hsieh, *A charge density wave-like instability in a doped spin-orbit-assisted weak Mott insulator*, *Nat Mater* **16** (2017) 200–203.

[99] Y. Ding, L. Yang, C.-C. Chen, H.-S. Kim, M. J. Han, W. Luo et al., *Pressure-Induced Confined Metal from the Mott Insulator* $Sr_3Ir_2O_7$, *Phys. Rev. Lett.* **116** (2016) 216402.

[100] J. He, T. Hogan, T. R. Mion, H. Hafiz, Y. He, J. D. Denlinger et al., *Spectroscopic evidence for negative electronic compressibility in a quasi-three-dimensional spin-orbit correlated metal*, *Nat Mater* **14** (2015) 577–582.

[101] T. Hogan, X. Wang, H. Chu, D. Hsieh and S. D. Wilson, *Doping-driven structural distortion in the bilayer iridate* $(Sr_{1-x}La_x)_3Ir_2O_7$, *Phys. Rev. B* **95** (2017) 174109.

[102] P. Liu, S. Khmelevskyi, B. Kim, M. Marsman, D. Li, X.-Q. Chen et al., *Anisotropic magnetic couplings and structure-driven canted to collinear transitions in* Sr_2IrO_4 *by magnetically constrained noncollinear DFT*, *Phys. Rev. B* **92** (2015) 054428.

[103] B. Kim, P. Liu and C. Franchini, *Dimensionality-strain phase diagram of strontium iridates*, *Phys. Rev. B* **95** (2017) 115111.

[104] S. Boseggia, R. Springell, H. C. Walker, A. T. Boothroyd, D. Prabhakaran, D. Wermeille et al., *Antiferromagnetic order and domains in* $Sr_3Ir_2O_7$ *probed by x-ray resonant scattering*, *Phys. Rev. B* **85** (2012) 184432.

[105] B. Kim, P. Liu and C. Franchini, *Magnetic properties of bilayer $Sr_3Ir_2O_7$: Role of epitaxial strain and oxygen vacancies*, *Phys. Rev. B* **95** (2017) 024406.

[106] S. L. Dudarev, G. A. Botton, S. Y. Savrasov, C. J. Humphreys and A. P. Sutton, *Electron-energy-loss spectra and the structural stability of nickel oxide: An LSDA+U study*, *Phys. Rev. B* **57** (1998) 1505–1509.

[107] H. Matsuhata, I. Nagai, Y. Yoshida, S. Hara, S. Ikeda and N. Shirakawa, *Crystal structure of Sr3Ir2O7 investigated by transmission electron microscopy*, *J. Solid State Chem* **177** (2004) 3776 – 3783.

[108] C. Dhital, T. Hogan, Z. Yamani, C. de la Cruz, X. Chen, S. Khadka et al., *Neutron scattering study of correlated phase behavior in Sr_2IrO_4*, *Phys. Rev. B* **87** (2013) 144405.

[109] M. K. Crawford, M. A. Subramanian, R. L. Harlow, J. A. Fernandez-Baca, Z. R. Wang and D. C. Johnston, *Structural and magnetic studies of* Sr_2IrO_4, *Phys. Rev. B* **49** (1994) 9198–9201.

[110] W. Setyawan and S. Curtarolo, *High-throughput electronic band structure calculations: Challenges and tools*, *Comput. Mater. Sci.* **49** (2010) 299 – 312.

[111] H. J. Park, C. H. Sohn, D. W. Jeong, G. Cao, K. W. Kim, S. J. Moon et al., *Phonon-assisted optical excitation in the narrow bandgap Mott insulator $Sr_3Ir_2O_7$*, *Phys. Rev. B* **89** (2014) 155115.

[112] A. de la Torre, E. C. Hunter, A. Subedi, S. McKeown Walker, A. Tamai, T. K. Kim et al., *Coherent Quasiparticles with a Small Fermi Surface in Lightly Doped* $Sr_3Ir_2O_7$, *Phys. Rev. Lett.* **113** (2014) 256402.

[113] B. Himmetoglu, A. Janotti, L. Bjaalie and C. G. Van de Walle, *Interband and polaronic excitations in* $YTiO_3$ *from first principles*, *Phys. Rev. B* **90** (2014) 161102.

[114] L. Bjaalie, A. Janotti, K. Krishnaswamy and C. G. Van de Walle, *Point defects, impurities, and small hole polarons in* $GdTiO_3$, *Phys. Rev. B* **93** (2016) 115316.

[115] P. D. C. King, T. Takayama, A. Tamai, E. Rozbicki, S. M. Walker, M. Shi et al., *Spectroscopic indications of polaronic behavior of the strong spin-orbit insulator $Sr_3Ir_2O_7$*, *Phys. Rev. B* **87** (2013) 241106.

[116] L. Li, P. P. Kong, T. F. Qi, C. Q. Jin, S. J. Yuan, L. E. DeLong et al., *Tuning the $J_{\text{eff}} = \frac{1}{2}$ insulating state via electron doping and pressure in the double-layered iridate $Sr_3Ir_2O_7$*, *Phys. Rev. B* **87** (2013) 235127.

[117] X. Chen, T. Hogan, D. Walkup, W. Zhou, M. Pokharel, M. Yao et al., *Influence of electron doping on the ground state of* $(Sr_{1-x}La_x)_2IrO_4$, *Phys. Rev. B* **92** (2015) 075125.

[118] T. Hogan, R. Dally, M. Upton, J. P. Clancy, K. Finkelstein, Y.-J. Kim et al., *Disordered dimer state in electron-doped* $Sr_3Ir_2O_7$, *Phys. Rev. B* **94** (2016) 100401.

[119] M. Miyazaki, R. Kadono, M. Hiraishi, A. Koda, K. M. Kojima, K. Ohashi et al., *Evidence for ordered magnetic moments at oxygen sites in antiferromagnetic* Sr_2IrO_4 *and* $Sr_3Ir_2O_7$, *Phys. Rev. B* **91** (2015) 155113.

[120] G. Trimarchi, Z. Wang and A. Zunger, *Polymorphous band structure model of gapping in the antiferromagnetic and paramagnetic phases of the Mott insulators MnO, FeO, CoO, and NiO*, *Phys. Rev. B* **97** (2018) 035107.

[121] C. G. Van de Walle, *Effects of impurities on the lattice parameters of GaN*, *Phys. Rev. B* **68** (2003) 165209.

[122] H. Iwahara, T. Esaka, H. Uchida and N. Maeda, *Proton Conduction In Sintered Oxides And Its Application to Steam Electrolysis For Hydrogen Production*, *Solid State Ionics* **3** (1981) 359–363.

[123] D. Medvedev, A. Murashkina, E. Pikalova, A. Demin, A. Podias and P. Tsiakaras, $BaCeO_3$*: Materials development, properties and application*, *Prog. Mater Sci.* **60** (2013) 72–129.

[124] B. G. Janesko, T. M. Henderson and G. E. Scuseria, *Screened hybrid density functionals for solid-state chemistry and physics*, *Phys. Chem. Chem. Phys.* **11** (2009) 443–454.

[125] A. Carvalho, A. Alkauskas, A. Pasquarello, A. K. Tagantsev and N. Setter, *A hybrid density functional study of lithium in ZnO: Stability, ionization levels, and diffusion*, *Phys. Rev. B* **80** (2009) 195205.

[126] A. Janotti, C. Franchini, J. B. Varley, G. Kresse and C. G. Van de Walle, *Dual behavior of excess electrons in rutile* TiO_2, *Phys. Status Solidi Rapid Res. Lett.* **7** (2013) 199–203.

[127] A. Janotti, J. B. Varley, M. Choi and C. G. Van de Walle, *Vacancies and small polarons in* $SrTiO_3$, *Phys. Rev. B* **90** (2014) 085202.

[128] T. M. Henderson, J. Paier and G. E. Scuseria, *Accurate treatment of solids with the HSE screened hybrid*, *Phys. Status Solidi B* **248** (2011) 767–774.

[129] H. J. Monkhorst and J. D. Pack, *Special points for Brillouin-zone integrations*, *Phys. Rev. B* **13** (1976) 5188–5192.

[130] K. Takeuchi, C.-K. Loong, J. R. Jr., J. Guan, S. Dorris and U. Balachandran, *The crystal structures and phase transitions in Y-doped $BaCeO_3$: their dependence on Y concentration and hydrogen doping*, *Solid State Ionics* **138** (2000) 63 – 77.

[131] T. Higuchi, H. Fukawa and H. Takahashi, *Valence States of $BaCe_{1-x}Y_xO_{3-\delta}$ Ceramics by Soft-X-Ray Spectroscopy*, *Trans. Mater. Res. Soc. of Japan* **36** (2011) 15–18.

[132] T. He, P. Ehrhart and P. Meuffels, *Optical band gap and Urbach tail in Y doped $BaCeO_3$*, *J. Appl. Phys.* **79** (1996) 3219.

[133] P. J. Hay, R. L. Martin, J. Uddin and G. E. Scuseria, *Theoretical study of CeO_2 and Ce_2O_3 using a screened hybrid density functional*, *J. Chem. Phys.* **125** (2006) 034712.

[134] J. L. F. Da Silva, M. V. Ganduglia-Pirovano, J. Sauer, V. Bayer and G. Kresse, *Hybrid functionals applied to rare-earth oxides: The example of ceria*, *Phys. Rev. B* **75** (2007) 045121.

[135] E. Mladenova, Z. Stoynov and D. Vladikova, *Comparative Studies of Polarizable Dielectric Fluids in Yttrium-Doped Barium Cerate by Permittivity Spectroscopy*, *Impedance Contributions Online* **12** (2014) P9:1–P9:9.

[136] J. Paier, C. Penschke and J. Sauer, *Oxygen Defects and Surface Chemistry of Ceria: Quantum Chemical Studies Compared to Experiment*, *Chem. Rev* **113** (2013) 3949–3985.

[137] E. Cordfunke, A. Booij and M. Huntelaar, *The thermochemical properties of $BaCeO_3(s)$ and $SrCeO_3(s)$ from T=(5 to 1500) K*, *J. Chem. Thermodyn.* **30** (1998) 437 – 447.

[138] W. Martienssen, O. Madelung and K.-H. Hellwege, *Thermodynamic Properties of Inorganic Materials*, *Landolt-Bornstein - Group IV Physical Chemistry - Volume 19* .

[139] M. Chase, *NIST-JANAF Thermochemical Tables*. J. Phys. and Chem. Ref. Dat. Mon. American Inst. of Physics, 1998.

[140] C. G. Van de Walle, *Interactions of hydrogen with native defects in GaN*, *Phys. Rev. B* **56** (1997) R10020–R10023.

[141] J. Hermet, M. Torrent, F. Bottin, G. Dezanneau and G. Geneste, *Hydrogen diffusion in the protonic conductor $BaCe_{1-x}Gd_xO_{3-\frac{x}{2}}$ from density functional theory*, *Phys. Rev. B* **87** (2013) 104303.

[142] C. G. Van de Walle and J. Neugebauer, *First-principles calculations for defects and impurities: Applications to III-nitrides*, *J. Appl. Phys.* **95** (2004) 3851–3879.

[143] A. Alkauskas, J. L. Lyons, D. Steiauf and C. G. Van de Walle, *First-Principles Calculations of Luminescence Spectrum Line Shapes for Defects in Semiconductors: The Example of GaN and ZnO*, *Phys. Rev. Lett.* **109** (2012) 267401.

[144] M. Kompan, Y. Baikov, B.-T. Melekh and A. Yakubovich, *Luminescence spectra of nominally pure $BaCeO_3$ perovskite crystals*, *Phys. Solid State* **44** (2002) 1263–1267.

[145] T. Norby, *Proton Conduction in Solids: Bulk and Interfaces*, *MRS Bulletin* **34** (2009) 923–928.

[146] Y. Yamazaki, F. Blanc, Y. Okuyama, L. Buannic, J. C. Lucio-Vega, C. P. Grey et al., *Proton trapping in yttrium-doped barium zirconate*, *Nature Mater.* **12** (2013) 647–651.

[147] H. Iwahara, T. Esaka, H. Uchida, T. Yamauchi and K. Ogaki, *High temperature type protonic conductor based on $SrCeO_3$ and its application to the extraction of hydrogen gas*, *Solid State Ionics* **1819, Part 2** (1986) 1003 – 1007.

[148] H. Iwahara, H. Uchida and I. Yamasaki, *High-temperature steam electrolysis using $SrCeO_3$-based proton conductive solid electrolyte*, *Int. J. Hydrogen Energ.* **12** (1987) 73 – 77.

[149] M. Zheng and X. Zhen, *$SrCeO_3$-based solid electrolyte probe sensing hydrogen content in molten aluminum*, *Solid State Ionics* **59** (1993) 167–169.

[150] K. Kreuer, *Proton-Conducting Oxides*, *Annu. Rev. Mater. Res* **33** (2003) 333–359.

[151] H. Uchida, H. Yoshikawa and H. Iwahara, *Dissolution of water vapor (or hydrogen) and proton conduction in $SrCeO_3$-based oxides at high temperature*, *Solid State Ionics* **35** (1989) 229 – 234.

[152] F. Goubin, X. Rocquefelte, M.-H. Whangbo, Y. Montardi, R. Brec and S. Jobic, *Experimental and Theoretical Characterization of the Optical Properties of CeO_2, $SrCeO_3$, and Sr_2CeO_4 Containing Ce^{4+} (f^0) Ions*, *Chem. Mater.* **16** (2004) 662–669.

[153] G. C. Mather, S. Garcia-Martin, D. Benne, C. Ritter and U. Amador, *A-site-cation deficiency in the $SrCe_{0.9}Yb_{0.1}O_{3-\delta}$ perovskite: effects of charge-compensation mechanism on structure and proton conductivity*, *J. Mater. Chem.* **21** (2011) 5764–5773.

[154] G. Henkelman, B. P. Uberuaga and H. Jnsson, *A climbing image nudged elastic band method for finding saddle points and minimum energy paths*, *J. Chem. Phys.* **113** (2000) 9901–9904.

[155] D. Steiauf, J. L. Lyons, A. Janotti and C. G. Van de Walle, *First-principles study of vacancy-assisted impurity diffusion in ZnO*, *APL Mater.* **2** (2014) 096101.

[156] V. M. Goldschmidt, *Die Gesetze der Krystallochemie*, *Naturwissenschaften* **14** (1926) 477–485.

[157] M. Johnsson and P. Lemmens, *Crystallography and Chemistry of Perovskites*, arXiv:cond-mat/0506606 [cond-mat.str-el].

[158] J. Ranlov and K. Nielsen, *Crystal structure of the high-temperature protonic conductor $SrCeO_3$*, *J. Mater. Chem.* **4** (1994) 867–868.

[159] N. Sata, H. Yugami, Y. Akiyama, T. Hattori, S. Yamaguchi and M. Ishigame, *Studies on the superlattice of perovskite-type proton conductors synthesized by pulsed laser ablation*, *Solid State Ionics* **121** (1999) 321 – 327.

[160] C. G. Van de Walle and J. Neugebauer, *Hydrogen in semiconductors*, *Annu. Rev. Mater. Res.* **36** (2006) 179 – 198.

[161] T. Scherban and A. Nowick, *Bulk protonic conduction in Yb-doped $SrCeO_3$*, *Solid State Ionics* **35** (1989) 189 – 194.

[162] J. Liu and A. Nowick, *The incorporation and migration of protons in Nd-doped $BaCeO_3$*, *Solid State Ionics* **50** (1992) 131 – 138.

[163] P. G. Moses, M. Miao, Q. Yan and C. G. Van de Walle, *Hybrid functional investigations of band gaps and band alignments for AlN, GaN, InN, and InGaN*, *J. Chem. Phys.* **134** (2011) 084703.

[164] C. G. Van de Walle and J. Neugebauer, *Universal alignment of hydrogen levels in semiconductors, insulators and solutions*, *Nature* **423** (2003) 626–628.

[165] C. G. Van de Walle, *Universal alignment of hydrogen levels in semiconductors and insulators*, *Physica B* **376-377** (2006) 1 – 6.

[166] J. B. Varley, A. Janotti and C. G. Van de Walle, *Hydrogenated vacancies and hidden hydrogen in $SrTiO_3$*, *Phys. Rev. B* **89** (2014) 075202.

[167] L. Weston, A. Janotti, X. Y. Cui, C. Stampfl and C. G. Van de Walle, *Hybrid functional calculations of point defects and hydrogen in* $SrZrO_3$, *Phys. Rev. B* **89** (2014) 184109.

[168] P. G. Sundell, M. E. Björketun and G. Wahnström, *Density-functional calculations of prefactors and activation energies for H diffusion in* $BaZrO_3$, *Phys. Rev. B* **76** (2007) 094301.